Re-analysis of Deep Excavation Collapse Using a Generalized Effective Stress Soil Model

by

Gonzalo Andrés Corral Jofré
B.Sc. in Civil Engineering (2000)
Structural Engineer (2001)
Pontificia Universidad Católica de Chile

M.Sc. in Geotechnical Engineering (2007)
Universidad de Chile

Submitted to the Department of Civil & Environmental Engineering
In Partial Fulfillment of the Requirements for the degree of

CIVIL ENGINEER

at the

Massachusetts Institute of Technology

June 2010

Signature of Author.....
Department of Civil & Environmental Engineering
May 21, 2010

Certified by.....
Andrew J. Whittle
Professor of Civil and Environmental Engineering
Thesis Supervisor

Accepted by.....
Daniele Veneziano
Chairman, Department Committee on Graduate Students

Re-analysis of Deep Excavation Collapse Using a Generalized Effective Stress Soil Model

by

Gonzalo Andrés Corral Jofré

Submitted to the Department of Civil and Environmental Engineering on May 21, 2010,
in Partial Fulfillment of the Requirements for the Degree of Civil Engineer

Abstract

This thesis re-analyzes the well-documented failure of a 30m deep braced excavation underconsolidated marine clay. Prior analyses of the collapse of the Nicoll Highway have relied on simplified soil models with undrained strength parameters based on empirical correlations and piezocone penetration data. In contrast, the current research simulates the engineering properties of the key Upper and Lower Marine Clay units using a generalized effective stress soil model, MIT-E3, with input parameters calibrated using laboratory test data obtained as part of the post-failure site investigation. The model predictions are evaluated through comparisons with monitoring data and through comparisons with results of prior analyses using the Mohr-Coulomb (MC) model.

The MIT-E3 analyses provide a modest improvement in predictions of the measured wall deflections compared to prior MC calculations and give a consistent explanation of the bending failure in the south diaphragm wall and the overloading of the strut-waler connection at the 9th level of strutting. The current analyses do not resolve uncertainties associated with performance of the JGP rafts, movements at the toe of the north-side diaphragm wall or discrepancies with the measured strut loads at level 9. However, they represent a significant advance in predicting excavation performance based directly on results of laboratory tests compared to prior analyses that used generic (i.e., non site-specific) design isotropic strength profiles.

Thesis Supervisor: Prof. Andrew J. Whittle
Title: Professor of Civil and Environmental Engineering

Acknowledgements

First and foremost, I would like to thank my supervisor, Professor Andrew J. Whittle, for giving me the opportunity of working with him on this fascinating project. Thanks for the guidance and advices during this research work. This has undoubtedly been a remarkable learning process.

I would also like to thank my friend and colleague, Sherif Akl for playing an important role on a part of this thesis, and also to my friend Dr. Maria Nikolinakou.

Additionally, I would like to express my sincere gratitude to Dr. Lucy Jen, and Dr. John T. Germaine for being always willing to help.

Finally to my family: Elisa, Eduardo & Ivette, Loreto, Cristóbal, Josefa, Tomás, Dominga, Antonia, Francisca, and Amalia for being a continuous support and appreciation of each personal goal and interest I have had. Specially, I would like to thank, Natalia, for being a tremendous support and encouragement during this MIT experience.

TABLE OF CONTENTS

LIST OF FIGURES

LIST OF TABLES

1 INTRODUCTION

A 30 m deep excavation in marine clay next to Nicoll Highway in Singapore collapsed at 3.30 pm on 20th April 2004. The excavation support system comprised 41.3 m deep diaphragm wall panels with 10 levels of preloaded cross-lot struts and two rafts of jet grout piles (JGP). Failure occurred when excavations progressed below the 9th level of strutting when the upper JGP (sacrificial) was removed. Figure 1-1 shows a picture taken after the collapse.

This thesis re-analyzes the collapse of the excavation using the generalized effective stress soil model, MIT-E3 (Whittle, 1987). This work enabled by a program of laboratory tests that were conducted as part of the post-collapse investigations at the site.

The thesis begins by reviewing the original project, corresponding to the first phase of construction for the new Circle Line Subway in Singapore, contract C-824. Chapter 2 describes the event leading up to the collapse and the causes of the collapse as determined by the Committee of Inquiry in May 2005 (COI, 2005).

Chapter 3 describes the local geology site conditions and soil properties together with key observations from data as reported by Davies et al., 2006. The chapter also discusses errors in the original design of the support system associated with the modeling of the undrained shear strength profile (based on Whittle & Davies, 2006).

Chapter 4 summarized the key features of the MIT-E3 soil model and describes model calibration for the Singapore Marine Clays at the site. This is made possible using laboratory data obtained from the post-collapse site investigation (Kiso-Jiban, 2005; unpublished)

Chapter 5 describes the 2-D finite element modeling for the instrumented section of the project at the strut line S335. Modeling is carried out using commercial Plaxis^{TM} (v.8.5). This is the first application of Plaxis that includes MIT-E3. The model was integrated within the Plaxis program by Akl and Bonnier (pers. comm., 2008)

Chapter 6 analyses all results obtained from the simulations. The effects of soil modeling on predictions of lateral wall deflections, bending moments, strut loads & vertical settlements are discussed in detail, comparing results from MIT-E3 with those obtained by conventional models. The predictions are then compared with monitoring data at S335.

Chapter 7 presents the summary, conclusions, and recommendations from this work.

Figure 1-1: Nicoll Highway Collapse – April 20th 2004 (COI, 2005)

2 PROJECT & COLLAPSE REVIEW

2.1. Overview

The new Circle Line (CCL) project in Singapore was intended to improve time for commuters around the downtown district, by passing busy interchanges such as City Hall and Raffles Place Figures 2-1, 2-2. The CCL project consists of twin subway tunnels 33.6 km long with 26 operating stations, and provision for 3 future stations. The project had an estimated budget of S$6.7 billion and was originally scheduled for completion in 2009.

Figure 2-2 and Table 2-1 shows that the project was to be built in 5 main stages. The first phase CCL1 has a total length of 5.4 km and was divided contracts C824 and C825. This thesis focuses on excavations for contract C824 between the proposed Nicoll Highway Station east to Kallang River, Figure 2-3. These locations are shown in more detail in Figure 2-5.

A complete description of the project can be found at the "Report of the Committee of Inquiry into the incident at the MRT Circle Line Worksite that led to The Collapse of Nicoll Highway on April 20th 2004 (COI, 2005).

2.2. Contract C-824

Contract C824 involved approximately 2.8 km of route and included the construction of Nicoll Highway and Boulevard Stations, and the linking tunnels. The original contract period ran from

May 30th 2001 to Jan 30th 2006. This design-build contract was awarded to a joint venture of Nishimatsu Construction Company Limited and Lum Chang Building Contractors. All parties (Contractor and Sub-Contractors) involved in C824 are shown in Figure 2-4. Hereby, it can be seen who was the responsible for each design and construction part of the contract, including the design of permanent works, installation of the diaphragm wall, steel work and strutting, excavation, instrumentation, the jet grout piles – JGP (Figure 2-6), the bored piles, the strut monitoring works, and, the soil investigation works. Table 2-2 outlines the different sections involved in C824, describing the type of sections, the wall type or wall label, and the approximate length in meters. The Collapse occurred in the Cut & Cover Tunnel 2 (CC2) area in design section M3 adjacent to the Temporary Access Shaft.

Figure 2-7 shows the design cross-section for the (intended) 33.3 m deep excavation comprising 0.8 m thick diaphragm wall panels that extend through deep layers of Estuarine and Marine clays (Kallang formation) and are embedded a minimum of 3 m within the underlying Old Alluvium (layer SW-2). The walls were to be supported by a total of ten levels of pre-loaded, cross-lot bracing and by two relatively thin rafts of continuous Jet Grout Piles (JGP). The Upper JGP raft was a sacrificial layer that was excavated after installation of the 9th level of struts.

The numerical simulations of excavation performance have been carried out focusing on one specific cross-section (within the collapse zone) corresponding to the location of the instrumented strut line S335, Figure 2-8. Loads in each of the nine levels of struts installed at S335 were measured through sets of three strain gauges. These data have been extensively

validated by each of the expert witnesses for the public inquiry (e.g., Davies et al., 2006). Measurements of the lateral wall movements at this section are obtained from inclinometer I-65 (installed through the north diaphragm wall panel) and I-104 located in the soil mass 1.5 – 2.0 m outside the South wall.

It is extremely important to denote that because of the length of the CC2 section, variation of ground conditions, among other singularities of the area, the project demanded different widths of excavation, depths of diaphragm walls, numbers of levels of struts and JGP thicknesses. In order to overcome this complexity, NLC subdivided the temporary work into different types, as Table 2-3.

2.3. Events Leading Up the Collapse

From March 2003 to April 2004, the construction of the temporary retaining wall system for C824 was surrounded by multiple problems. These were detailed by the COI report (COI, 2005) and included incidents at Launch Shaft 2, and cut and cover excavations Type K, and Type M2 & Type M3 are included.

Problems in the collapse area begin when measured lateral wall deflection exceeded the design level on February 23th 2004 (145 mm) when excavation was progressed to a depth of 18.3 m (corresponding to 84.6 m RL in Figure 2-7). The contractor presented backanalyses (BA1) on March 5th 2004 to increase allowable design wall deflection, from 145 mm to 253 mm.

The revised levels for wall deflection were exceeded on March 30th 2004 (excavations at 78.3 m RL). This provided further re-analyses of M3 (BA2) that were finally approved on April 19th which design levels increased to 359 mm. These design levels were exceeded the following day at M3 (as measured by one of the inclinometer on the south side of the wall). On April 20th, the first signs of collapse were related to observations of failure in the 9th level strut-waler connections (these were observed over a period of 4 hours, 9 am-1 pm). Strut loads measured at S335 response at about 11am when the load drops in the 9th level strut increasing by an equal amount in the 8th level strut (indicating a transfer of load upwards trough the bracing system). Contingency actions at the site, including adding concrete to strengthen strut-waler connections were ineffectual and failure at the 8th level strut-waler connection began at 3:00 pm. The excavation collapsed catastrophically at 3:30 pm with the tragic loss of 4 lives. Further details can be found on the COI report (COI, 2005).

2.4. Collapse Causes Summary

Based on Committee of Inquiry Report (COI, 2005), the main causes of the collapse can be attributed to two critical design errors in the temporary retaining wall system. These two errors correspond to:

1. The under-design of the diaphragm wall using Method A.
2. The under-design of the waler connection:
    a. Incorrect estimations of loads on waler connections for different strut conditions.

b. Replacement of plate waler connections by C-channels which do not posses ductile behavior.

Figure 2-9 presents a more detailed breakdown of causality as proposed by Arup (2005).

From a geotechnical perspective, under-design of the diaphragm wall using Method A is one of the key factors. The terminology Method A refers to the particular use of the Plaxis program to present undrained behavior of low permeability clays using the reference Mohr-Coulomb (MC) model. Table 2-3 shows that there are three possible methods for representing undrained behavior using the MC model.

Method A refers to the approach where effective stress strength parameters (c', ϕ') are used as inputs. In this case, undrained shear strength is obtained implicitly by the MC model (based on assumptions of linearly-elastic, perfectly-plastic material behavior. Whittle & Davies (2006) have shown that using Method A (with parameters observed from drained strength of Singapore Marine Clay) greatly overestimates the undrained shear strength of the profile. As a result, the original design underestimated the wall deflections (Figure 2-11) and bending moments in the diaphragm used at section M3 (by a factor of 2). It also led the designers to undersize JGP rafts (see Figure 2-9). However, as shown in Table 2-4, Method B has a much smaller effect on predictions of strut loads. Indeed only 2 levels of struts are expected to carry higher loads according to Method B (levels 6 and 9).

In comparison of the experts to the COI all used Method B (Table 2-3), which uses the undrained strength profile directly as input to the MC model (c'→su, ϕ=0; i.e. total stress strength parameters are used). This method is considered reliable assuming there is minimal consolidation occurring in the clay layer over the time frame of the construction.

Figure 2-10 summarizes the stress paths for each of the 4 methods in q-p' space (where q= (σ_1-σ_3) is the shear stress and p'=1/3(σ'_1+σ'_2+σ'_3) is the mean effective stress). This example assumes initial hydrostatic conditions (i.e. K_0=1), showing the value of undrained shear strength reached using each method. As may be noted in this Figure, Method A dramatically overestimated the s_u (or c_u) value.

Table 2-1: The Various Stages of the MRT Circle Line Project (COI, 2005)

CCL Stage	Description	No of Stations	Stage Length (km)	Year Start / Expected Year of Completion
CCL1	From Dhoby Ghaut to Boulevard station	6	5.4	2001 / 2006
CCL2	From Old Airport Road to Upper Paya Lebar Station	5	5.5	2002 / 2006
CCL 3	From Bartley to Marymount Station	5	5.7	2003 / 2008
CCL 4	From Thomson to NUH station	8	10.4	2004 / 2009
CCL 5	From West Coast to HarbourFront station	5	6.6	2004 / 2009
	Total	**29 stations**	**33.6**	

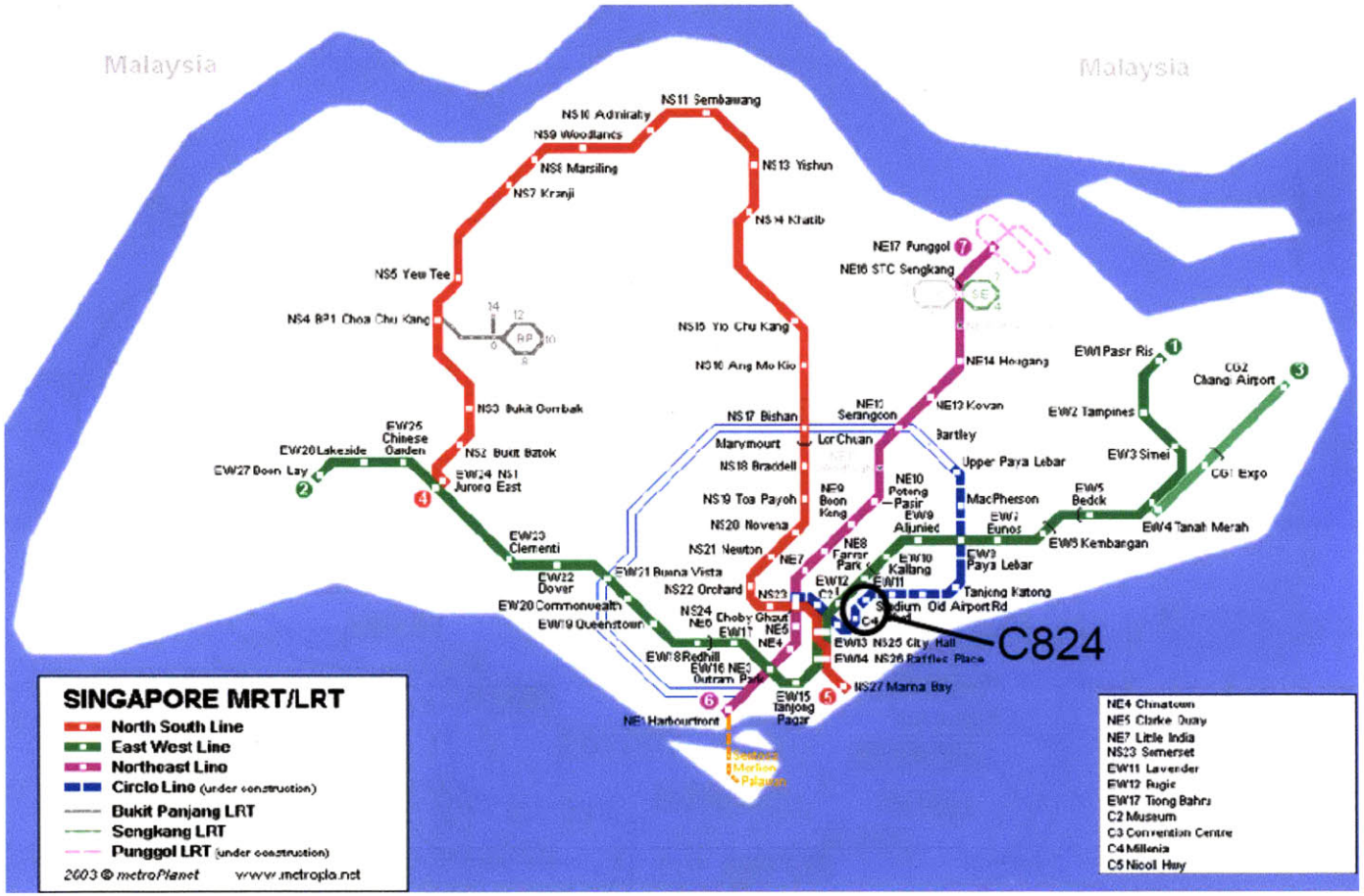

Figure 2-1: Subway system in Singapore, showing new Circle Line project in 2006

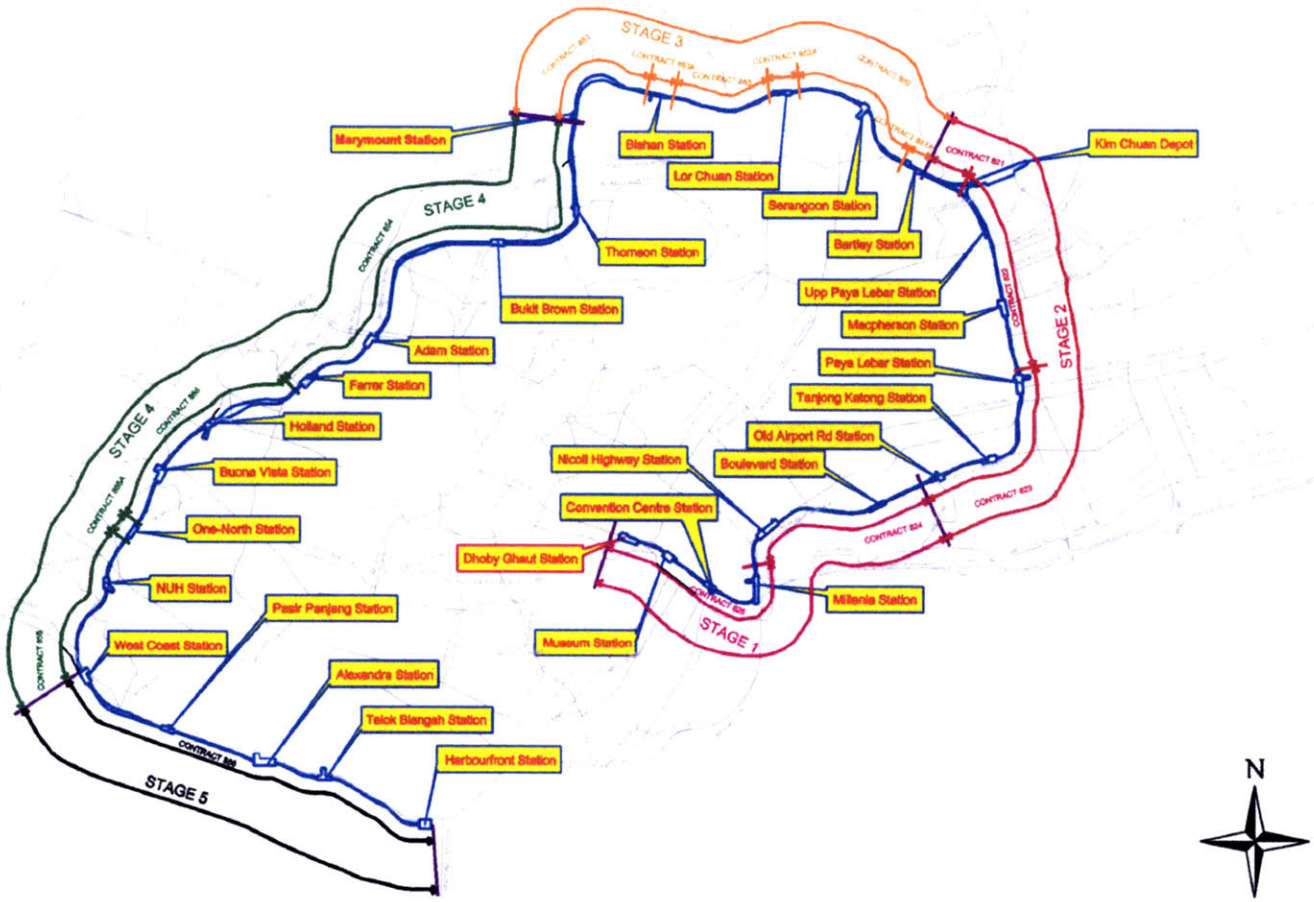

Figure 2-2: Overview of Circle Line Stages (COI, 2005)

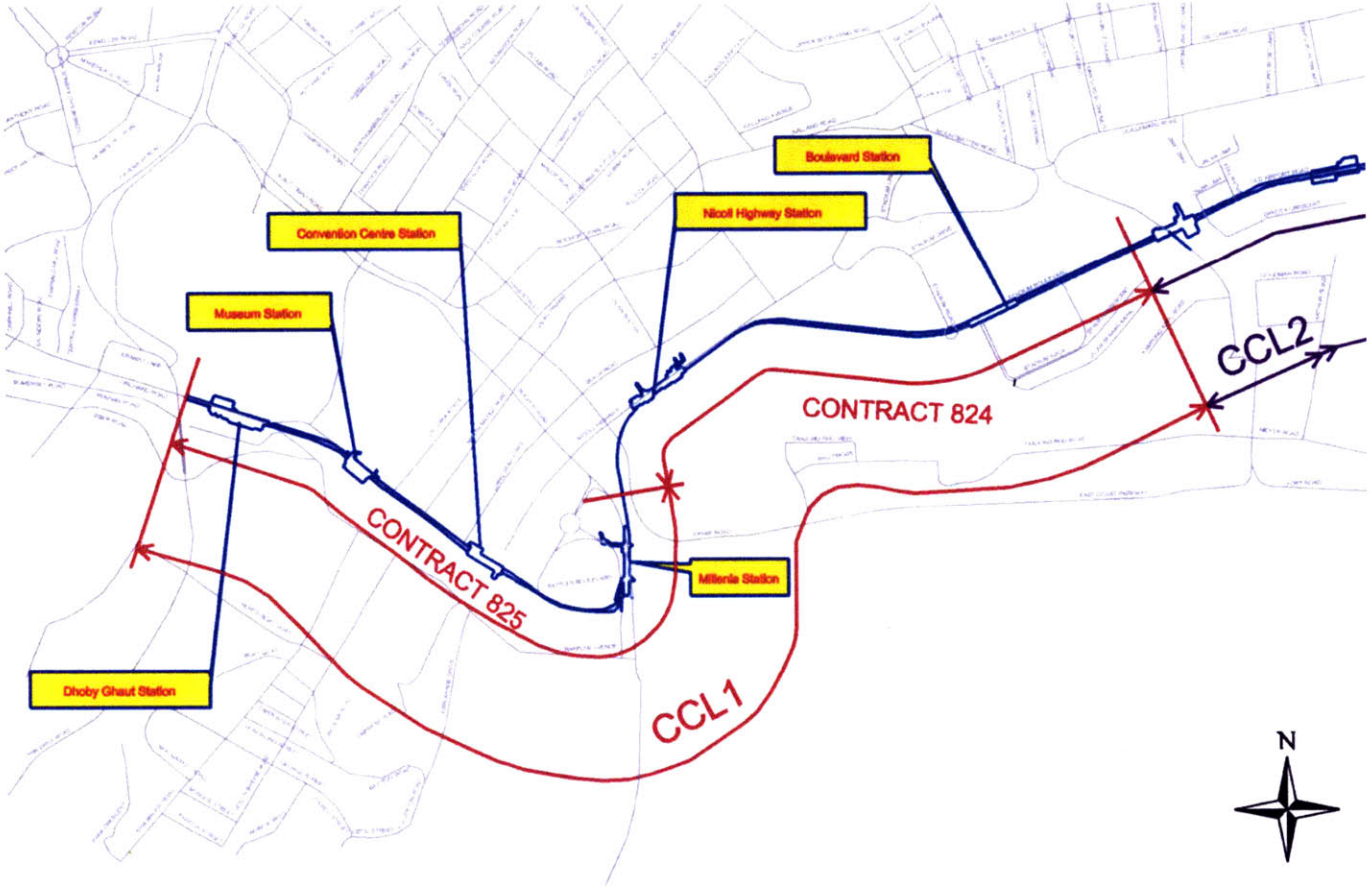

Figure 2-3: Overview of Circle Line Stage 1: CCL1 (COI, 2005)

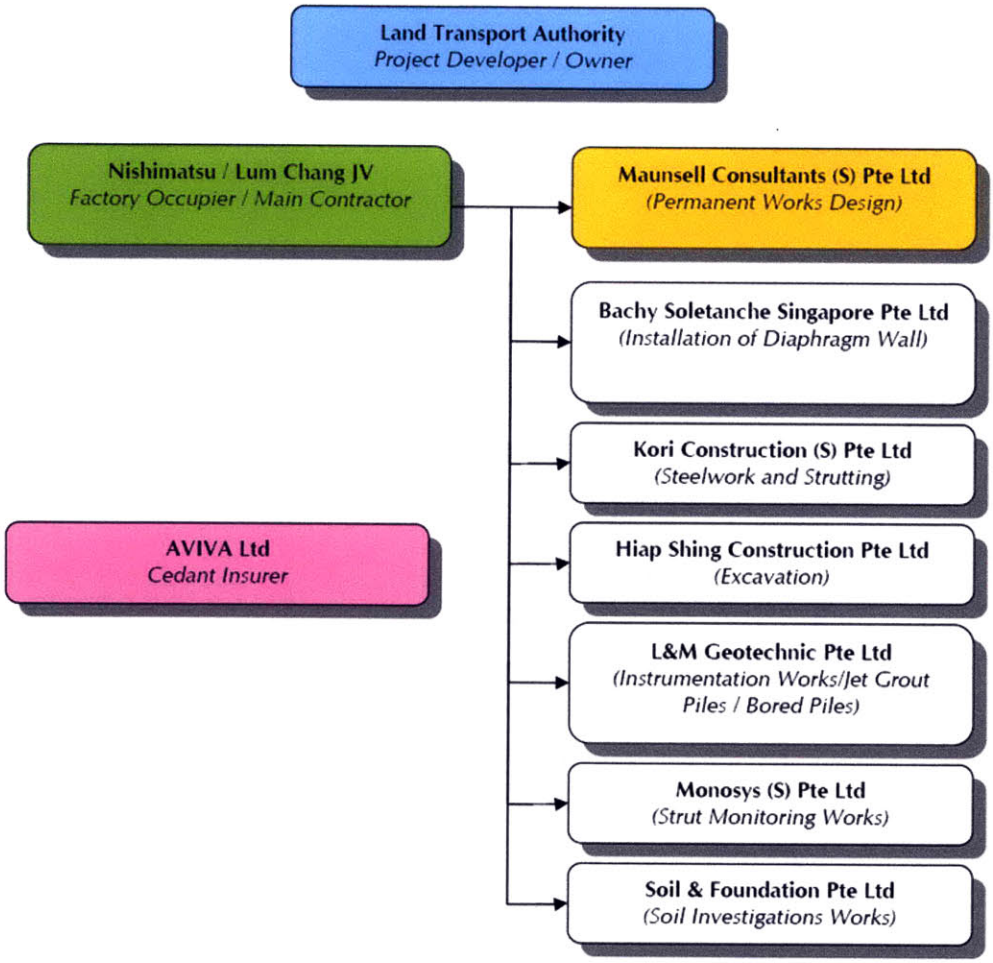

Figure 2-4: Chart showing the Relationship of Parties Involved in C824 (COI, 2005)

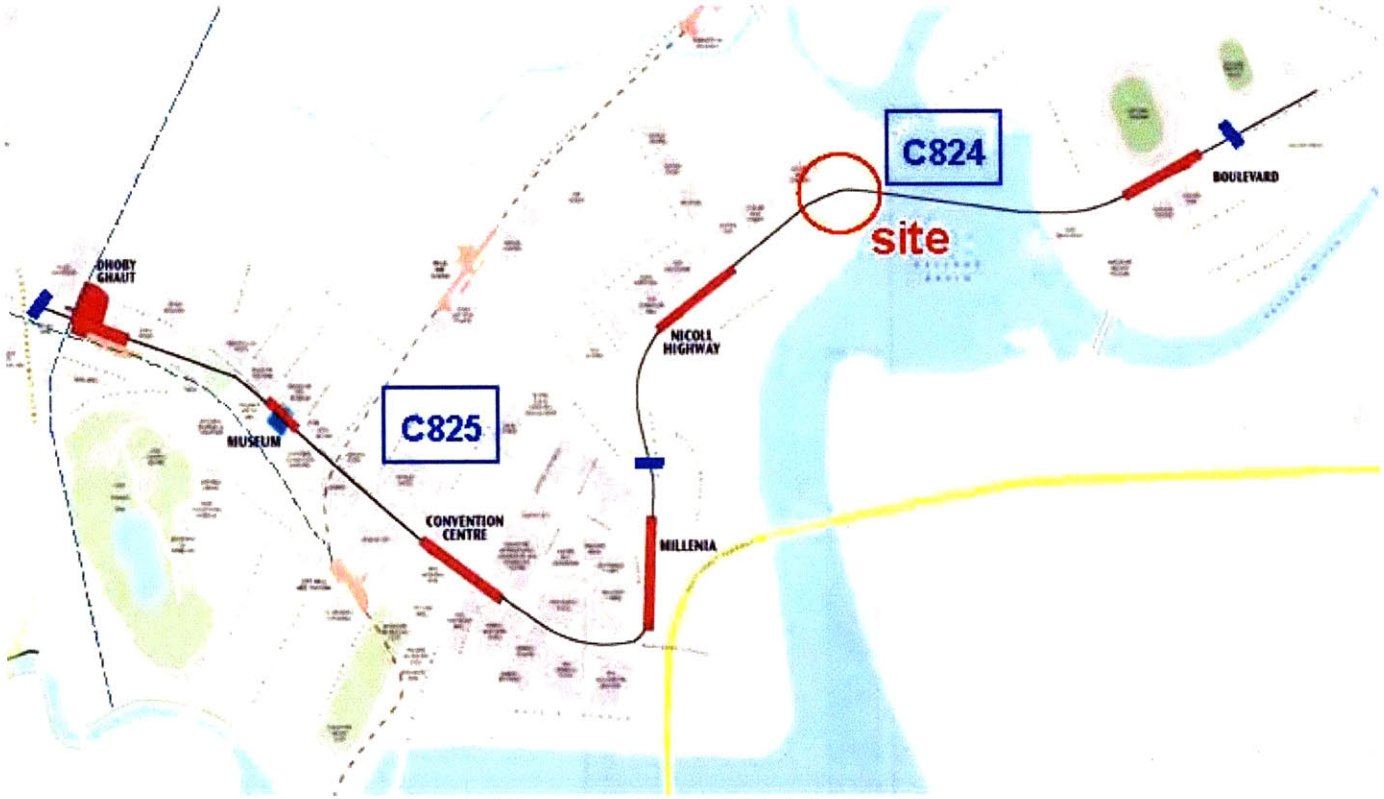

Figure 2-5: **Contract C824 involved approximately 2.8 km of route and included the construction of Nicoll Highway & Boulevard Stations, and the linking tunnels (Davies at al., 2006)**

Table 2-2: The Various Sections of C824 and Sections of Cut & Cover 2: CC2 (COI, 2005)

Section of C824	Wall Type	Approx. Route Length (m)
Cut & Cover Tunnel 1 (CC1)	Type A, B, B1 and C	372
Nicoll Highway Station (NCH)	Type D2, D1A, E1, F1, E2, D1, E3, E4, F2, G1 and G2	327
Cross Over Box (XOB)	Type H, I, J and K	199
Cut & Cover Tunnel 2 (CC2)	Type L, M1, M2 and M3	211
TSA Shaft (TSA)	Type N	35
Bored Tunnels (under Kallang Basin)	-	799
Launch Shaft 1	Type Q1 and Q2	33
Boulevard Station (BLV)	Type R1, S and R2	246
Boulevard Siding (BLS)	Type T, U1, U2, V, W1, W1a, W1b, W2, W2a and Y	475
Bored Tunnels (over-run after BLS)	-	71
	Total	**2768**

Section of CC2	Approx. Route Length (m)
Type L	46
Type M1	44
Type M2	88
Type M3	33
Total Route Length	**211**

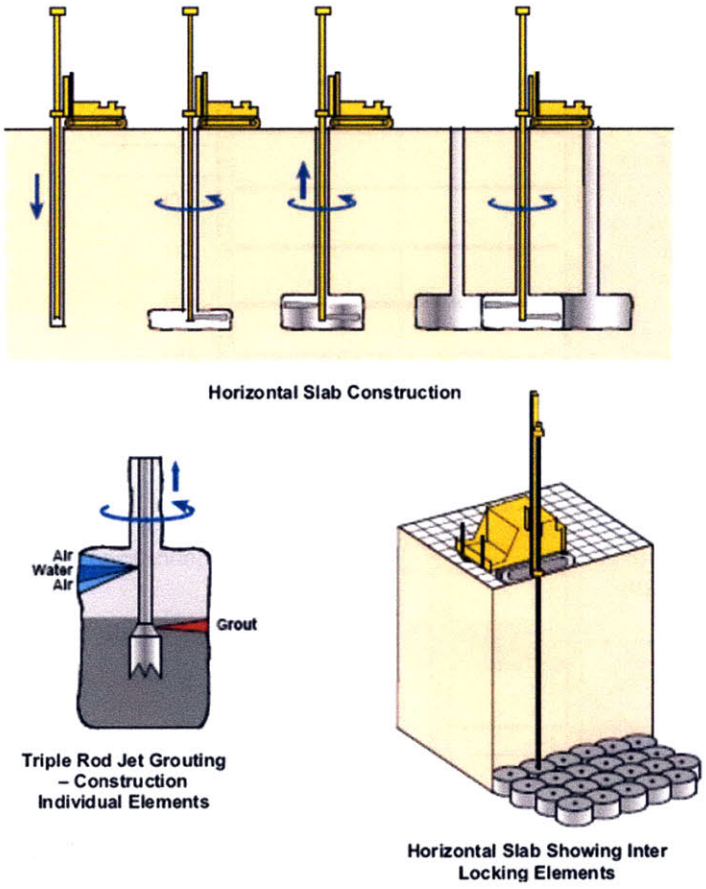

Figure 2-6: Construction Principle of the Jet Group Pile – JGP – Slab (COI, 2005)

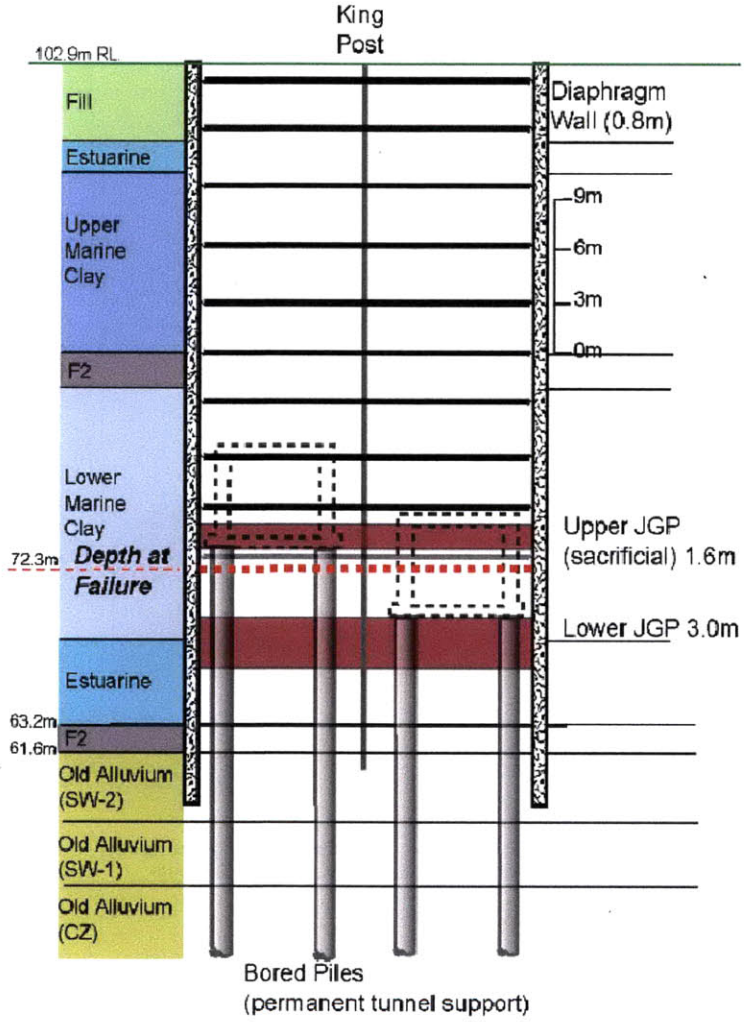

Figure 2-7: M3 typical design cross-section of excavation support system (Whittle and Davies, 2006)

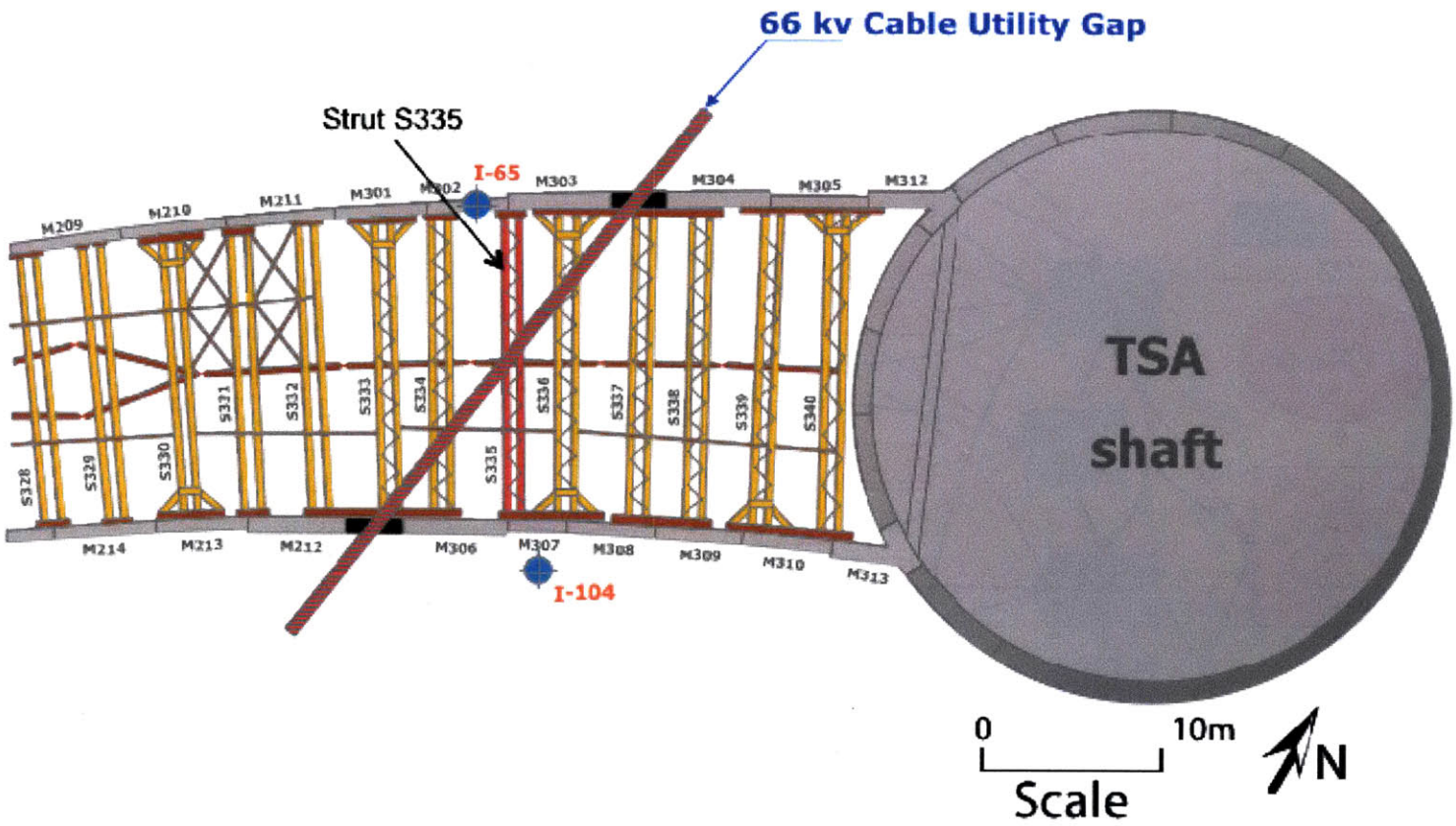

Figure 2-8: Plan showing the structural support system and 9th level strutting and monitoring instrumentation (Corral & Whittle, 2010)

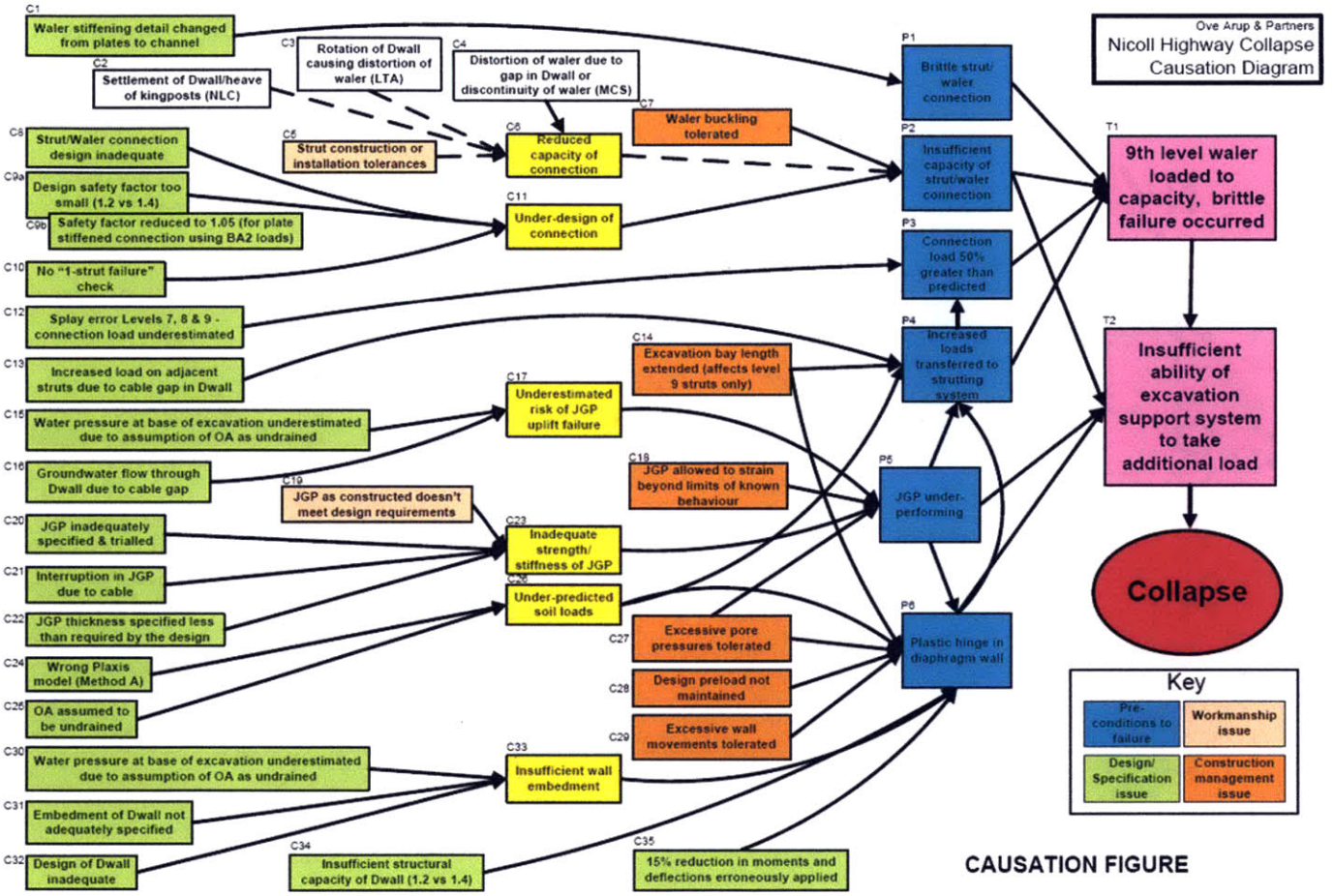

Figure 2-9: Diagram: Collapse Causes interpreted by ARUP (ARUP, 2005)

Table 2-3: Definition of Methods A, B, C & D (COI, 2005)

Undrained Behaviour					
Method	**Plaxis Material setting**	**Material Model**	**Parameters**		**Computed stresses**
			Strength	**Stiffness**	
A	Undrained	Mohr-Coulomb	c', ϕ' (effective)	E',ν' (effective)	Effective stress and pore pressure
B	Undrained	Mohr-Coulomb	c_u, ϕ_u (total)	E', ν' (effective)	Effective stress and pore pressure
C	Non-porous	Mohr-Coulomb	c_u, ϕ_u (total)	E_u, ν_u=0.495 (total)	Total stress
D	As in Method A, for other soil models				

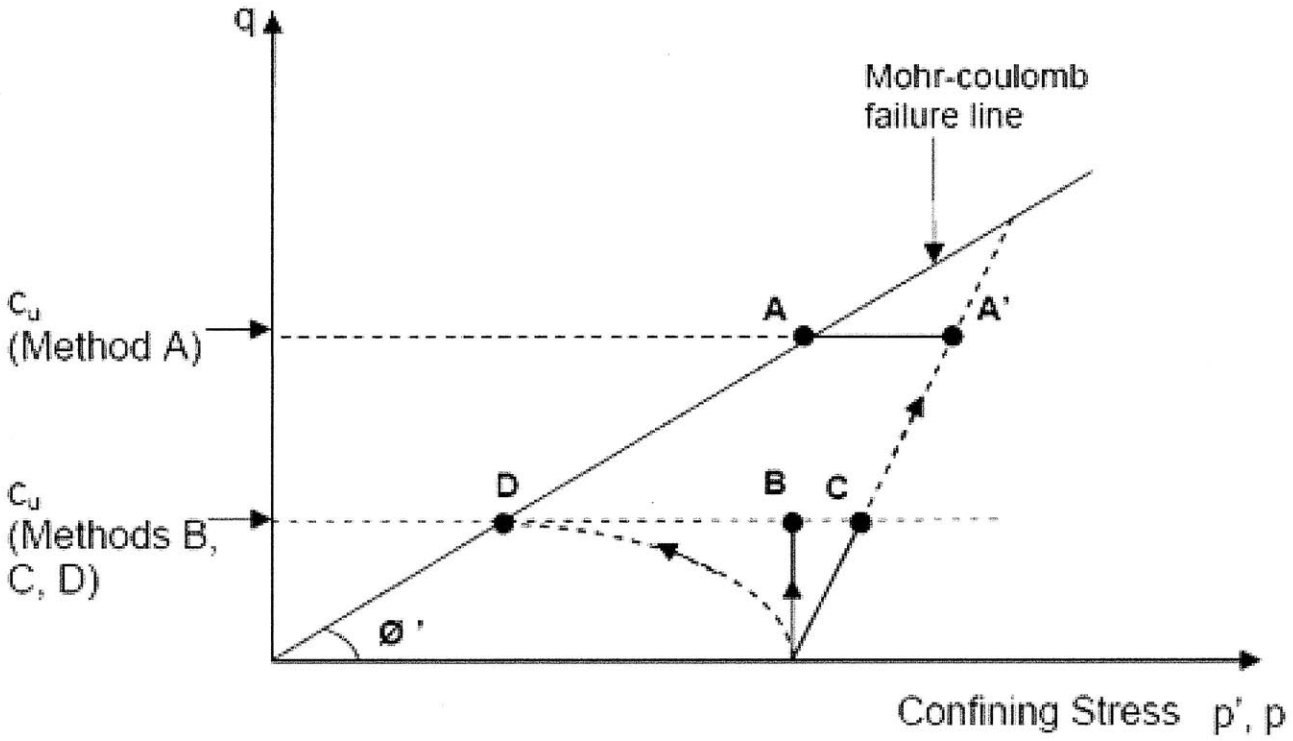

Figure 2-10: Mohr-Coulomb Failure Model: Undrained Shear Strengths derived from Methods A, B, C & D used in the C824 Project (COI, 2005)

Table 2-4: Comparative Study of Method A & Method B for Strut Loads at Type M3 (COI, 2005)

Strut Row	Predicted Strut Load Using Method B (kN/m)	Design Strut Load (unfactored) Using Method A (kN/m)	Ratio Method B to Design Strut Load
1	379	568	67%
2	991	1018	97%
3	1615	1816	89%
4	1606	1635	98%
5	1446	1458	99%
6	1418	1322	107%
7	1581	2130	74%
8	1578	2632	60%
9	2383	2173	110%

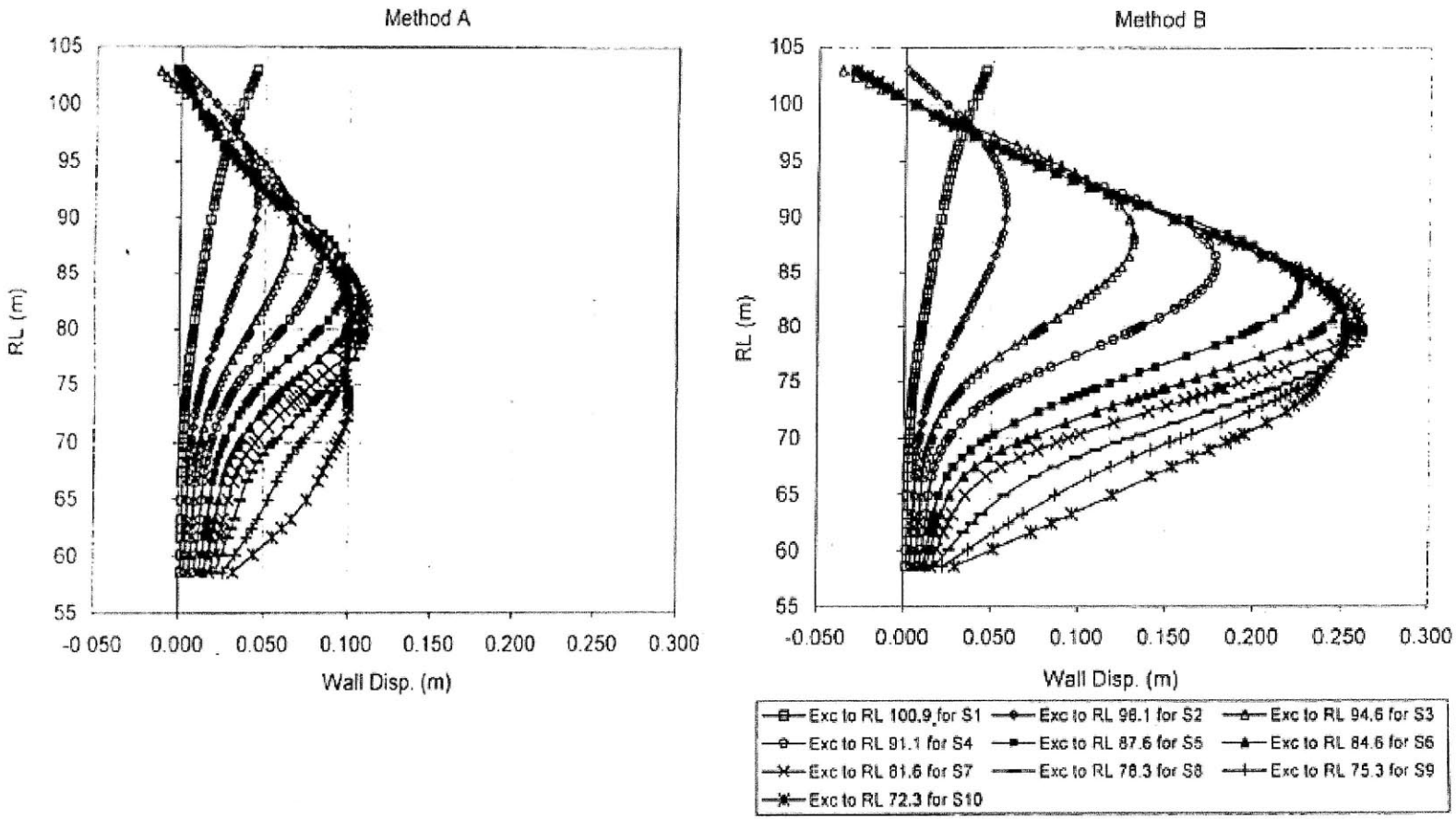

Figure 2-11: Lateral Wall Defection comparison between Method A & B (COI, 2005)

3 SITE CONDITIONS

3.1. Geology and Site Conditions

Figure 3-1 shows a generalized map of surficial geology for Singapore, illustrating the main geological formations which can be found in the island. Circle Line contract C824 is located within underlying by the Kallang formation and affected by more recent land reclamation (dating from 1940's; see Figure 3-4). The M3 section comprises more than 40m of marine sediments underlying by variable deposits of Old Alluvium.

Chiam et al. (2003) and Pitts (1984) state that the Old Alluvium (OA) is known to be the oldest of the drift deposits and is mainly found in the eastern and northwestern parts of Singapore. It is an extension of early Pleistocene deposits found in southern Johore and exists as a virtually uninterrupted sheet either at the surface or buried beneath younger deposits. Davies (1984) shows typical conditions in the Kallang formation where the marine deposits are formed in valley cut into the Old Alluvium, Figure 3-3. This is consistent with the alluvial drainage pattern outlined in a review of the Pleistocene deposits by Gupta el al. (1987).

More recently, Mote at al. (2009) have discussed the existence of Palaeochannels locally in the Old Alluvium. Figure 3-2 shows their statistical interpretation of meandering channels and their likely occurrence in the vicinity of C824.

Regarding the Kallang Formation, the main two units of marine clay (upper and lower) are found consistently. It is believed that the upper clay was deposited during the Holocene era, but the lower one was deposited more that 10,000 years ago (Hanzawa and Adachi 1983; Pitts 1984).

The presence of land reclamations plays a very important role to comprehend the state of the main soil layers in some areas of Singapore. Two periods of reclamation have been identified. The first in the 1930-1940's and the second in the 1970's, as shown in Figure 3-4. The extent of the second reclamation is clearly illustrated by a 1969 aerial photo of the site, Figure 3-5.

Whittle and Davies (2006) present an illustration (Figure 2-7) of the original design of the lateral earth support system (based on one borehole – ABH32) at the initiation of the collapse area (type M3). The cut-and-cover section is approximately 20m wide, with a final formation depth of 33 m. Most of the diaphragm walls (i.e. excavation support system) have a thickness of 80 cm and a varying embedment in the Old Alluvium (OA). The walls were designed with 10 levels of pre-loaded cross-load bracing and two rafts of jet grout piles. The collapse occurred (April 20th 2004) following the installation of strut level 9 and removal of the upper sacrificial JGP raft when the formation was at approximately 72.3 m RL. No level 10 struts were installed.

The location of the pre-tender and post-tender boreholes, piezocones and diaphragm wall panels in the M3 section are presented in Figure 3-6.

The typical soil profile comprises (Figure 2-7) Fill, Upper Estuarine, Upper Marine Clay (UMC), transition clay unit F2, Lower Marine Clay (LMC), Estuarine units, F2 Clay and Old Alluvium (OA). Whittle and Davies (2006), indicate that for practical purposes (e.g., estimation of

undrained shear strength) there is little to distinguish the lower Estuarine and Marine clay units of the Kallang formation (both have plasticity indices, I_p = 35- 55%, while the Estuarine has a slightly higher liquid limit, w_L = 70-100% than LMC, w_L = 65-80%). The thicknesses of each layer vary considerably from one point to another. Figures 3-7 and 3-8 show two sections constructed using data from the pre-tender borings. The bases of the marine clay/estuarine deposits are clearly defined and show a significant change in elevation across the site. The deepest sections of Marine clay are in M3 and in the south side of the excavation. The top of the buried layer of OA is more difficult to interpret from the complex borehole descriptions. Whittle and Davies (2006) present the elevation of the bottom of LMC and the top of OA based on a definition N_{spt}>30, Figures 3-9 and 3-10.

Contour plots assembled for the COI (Figure 3-10) show clearly a valley within the OA. The valley trends NNE-SSW and is deepest between the TA Shaft and the instrumented strut line S335.

The OA classified as very dense silty sands with transitioning with depth to very stiff to hard, silty clay. Also, it is convenient to separate the OA in different sub-layers depending on the SPT blowcounts (Whittle & Davies, 2006). There is evidence that, at the North side, transitional fluvial sand (F1) exists between the OA and the Marine Clay, and, fluvial clays (F2) at the South side.

The groundwater table in the fill varies from 100 to 100.5 m (RL). However, standpipe piezometer data from boreholes indicate an excess of piezometric head (estimated at H~103 m) below the Marine Clay (COI, 2005; Figure 3-11). Surface settlements measured prior to

construction (2000-2001), Figure 3-12. Hence, Whittle and Davies (2006) conclude that there is on-going consolidation within the Marine Clay that can affect excavation performance.

The most reliable data for estimating the undrained shear strength was provided by piezocone penetration records (Whittle & Davies, 2006). Figure 3-13 shows a comparison of the undrained shear strength captured by four piezocone records. These are interpreted using a cone factor N_{kT}=14. The results are compared with a design strength line for normally consolidated marine clay using an average undrained strength ratio s_u/σ'_{vo} = 0.21. (This corresponds to the assumed undrained properties in the original Geotechnical Interpretative Memorandum; GIM, 2001). The results show good agreement between the GIM and piezocone strengths in the Upper unit of the Marine Clay (UMC). However, the piezocone results also suggest that the Lower Marine Clay (below 75mRL) is weaker than the design strength profile. Whittle and Davies (2006) have attributed this to underconsolidation of the Lower Marine Clay associated with 5m of fill used to reclaim the land in the 1970's. This explanation assumes that the underlying units of Old Alluvium have low bulk permeability and/or low recharge potential.

3.2. Construction

The construction sequence of the cut-and-cover excavation at C824 has the following main stages: 1) install diaphragm walls, 2) install bored piles, 3) drive king posts, 4) install jet gout piles (JGP), 5) excavation and the strut pre-loading (10 stages), and then 6) permanent works (tunnel supports). Collapse occurred prior to installation of the 10th level of strutting.

According to Whittle and Davies (2006), the original design idea was to achieve 3m of embedment of the diaphragm wall panels within the Old Alluvium. However, the construction records show that the individual panels of the diaphragm wall were actually installed to specified design elevations rather than embedment requirements. Figure 3-15 show the as-built wall panels on the North and South side of the excavation. Panel embedment was much less than 3m for a series of panels close to the TSA Shaft where the Old Alluvium is at the greatest depth. At the instrumented section S335, the embedment of panels M307 and M302 is critically quite close to design (1.8 – 2.6 m). Figure 3-15 also shows the gap in the diaphragm wall due to the presence of the 66 kv cable. The designers increased panel with and reinforcement of the adjacent panels (M303-M304, M212-M306) to enable arching of earth pressures across these gaps.

The JGP was designed as two relatively thin rafts in the M3 area (upper 1.6 m and lower 2.5 m thick, respectively). Jet group piles were installed using a double fluid jetting system with parameters calibrated for conditions in the upper Marine clay (i.e. jetting parameters were selected to achieve required column diameter). The design shear strength of the JGP rafts was s_u=300 kPa based on prior empirical data. Figure 3-14 shows the sequence of column installation that was intended to produce an integral raft of soilcrete. In practice, records on actual pile installation were incomplete and do not enable validation of the actual construction. Whittle and Davies (2006) note that is unlikely that the design column dimensions were achieved for JPG piles installed trough higher strength OA or F2 layer.

3.3. Instrumentation and Monitoring Data

Instrumentation is critical for monitoring and controlling the excavation performance.

There are two inclinometers available for interpreting wall deflections at the M3 section, I-104 (south side 2m behind the wall) and the I-65 (north side within diaphragm wall), Figure 2-8.

The loads in each strut level at the line S335 (Figure 2-8) were also monitored using load cells (recording strut pre-load) and sets of three strain gauges.

Davies et al. (2006) present the lateral wall deflection measurements for excavation levels 6, 7, 8, & 9, Figure 3-16 and for conditions immediately prior to the failure, April 17-20, Figure 3-17. The data shows very similar measured deflections of the north and south trough early March, 2004 (strut level 7 installed). Thereafter, the south wall countries to deform significantly below the formation level, reading 300 mm at level 9 (April 5), while there are negligible movements at the North wall over this same time period (March-April; levels 7-9) This asymmetry is closely linked to the underlying stratigraphy.

Figure 3-18 shows a summary of S335 strut load data for levels 5 trough 9. These data were validated by the experts at the COI and show an unexplained disconnect between the imposed pre-load (measured by load cell) and subsequent strut loads obtained by strain gauges. The data show a consistent pattern of increased load in the succeeding excavation step (after pre-load), a decrement due to installation of the next strut, and general reduction in load thereafter.

3.4. Effect of Undrained Strength Profile on Predicted Performance

Whittle and Davies (2006) carried out a series of finite element simulations in order to investigate the role of the analysis method (A vs. B) and selected undrained shear strength

profiles on performance of the M3 excavation. Figure 3-19 shows 4 profiles used in these calculations:

1. A[NLC] is a calculation that reproduces the original design using Method A. The undrained shear strength of the Marine and Estuarine Clay units are based on the use of effective stress strength parameters (c', ϕ') provided by GIM (2001).
2. B[GIM] uses Method B (s_u, $\phi' = 0°$) to represent the undrained strength profile for the Marine and Estuarine clay layers with undrained shear strengths specified by GIM (2001).
3. GIM* also uses Method B, but makes three amendments that are consistent with more detailed interpretation of local ground conditions. These relate to undrained strength of the Old Alluvium and as-constructed thickness of JGP rafts.
4. EBC corresponds to Whittle and Davies (2006) best estimates of the undrained strength profile, including underconsolidation of the Lower Marine Clay.

The resulting predictions of lateral wall deflection results are summarized in Figure 3-20 at level 7 excavation and at the final dig level. Method A clearly underestimates the magnitudes of wall deflections by more than a factor of 2 compared with the tree method analyses. Additionally, the maximum strut loads at each excavation level 6, 7 & 9, and for each s_u profile are presented in Figure 3-21. These results show that all 4 sets of analyses predict overloading of the as-built strut-waler connection at level 9.

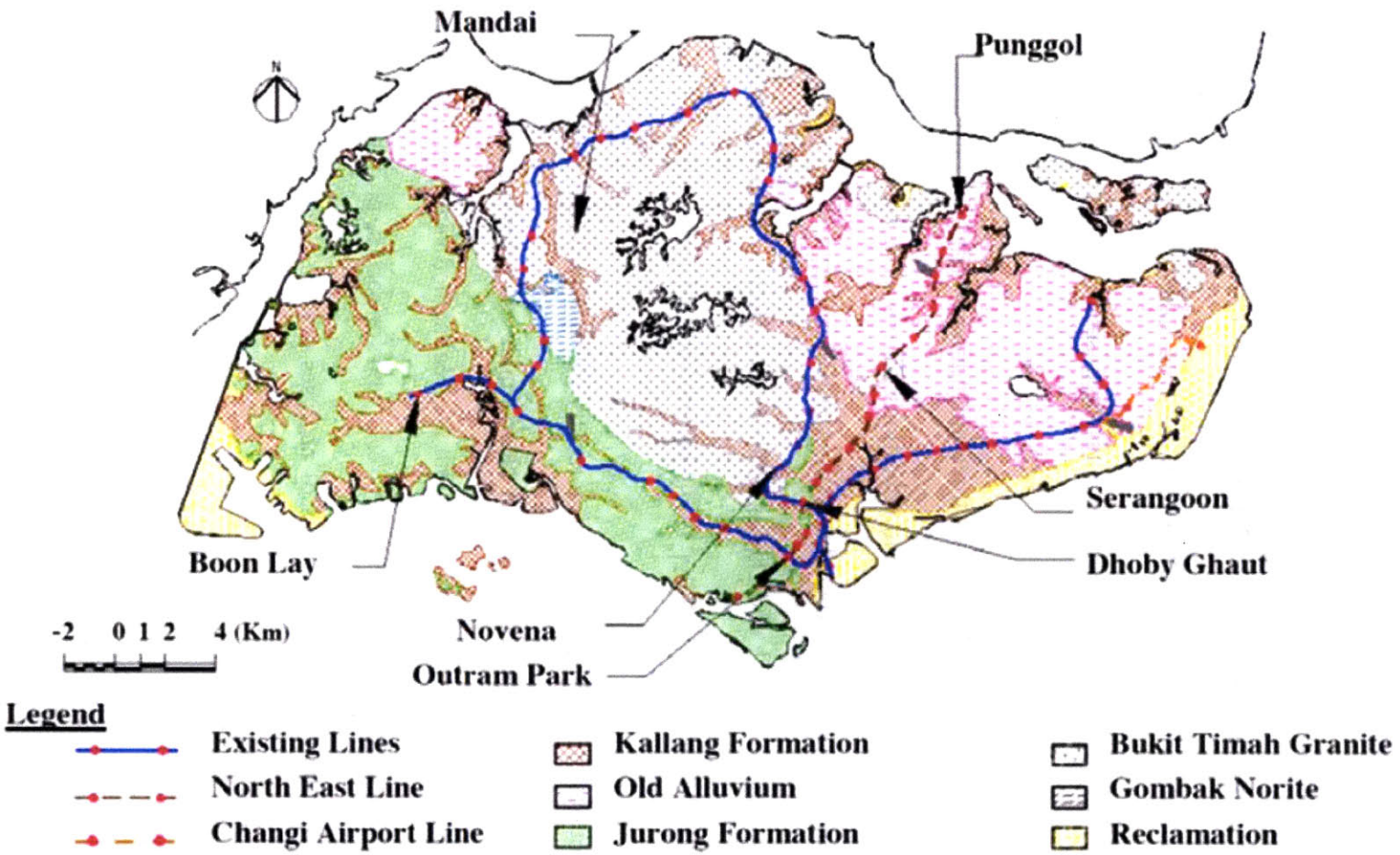

Figure 3-1: Geology of Singapore showing the North East Line Location (Shirlaw et al., 2000)

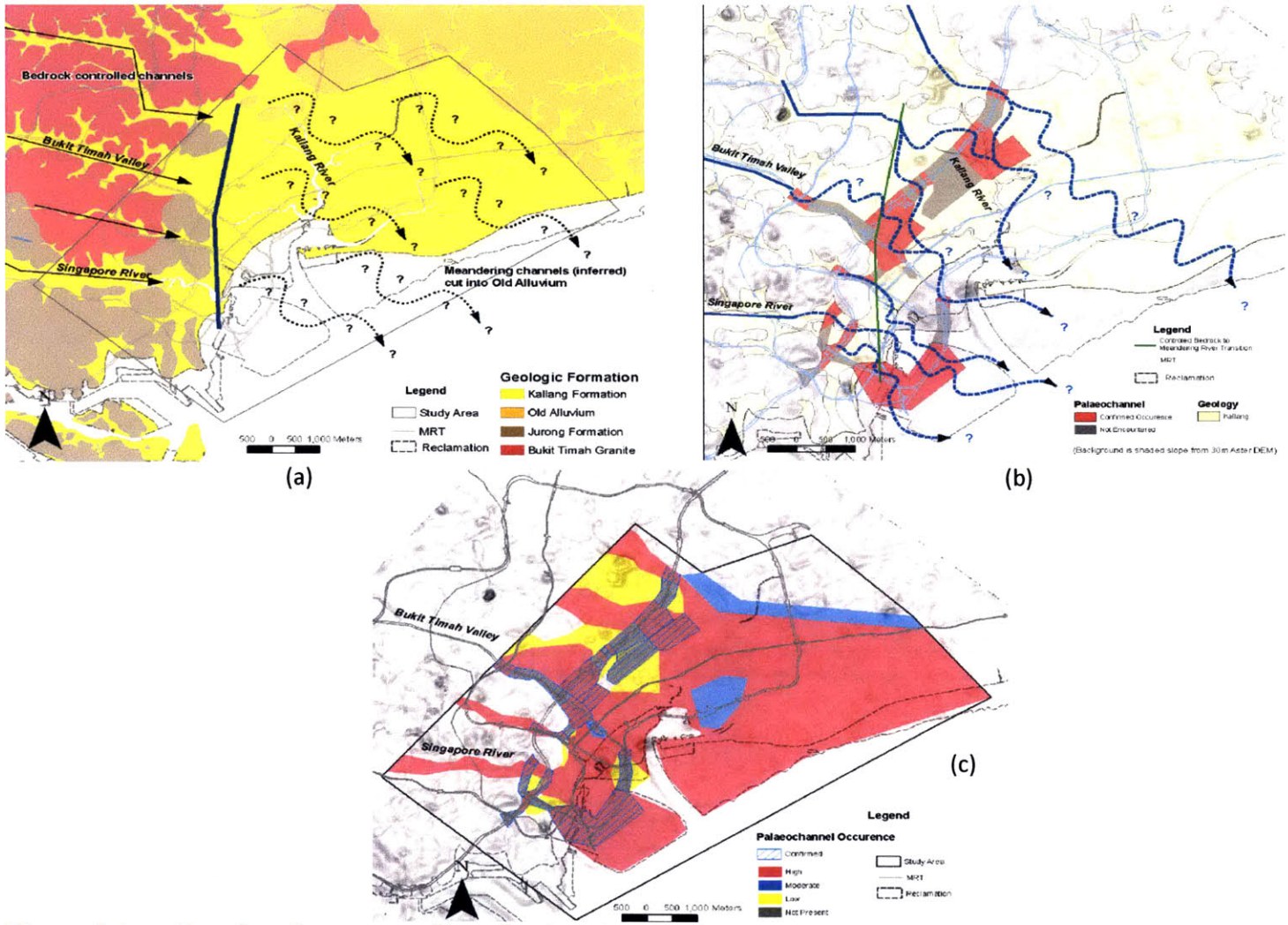

Figure 3-2: Results of recent studies of paleo-channels beneath Kallang formation (a) Transition from Bedrock Controlled Channels into Meandering Channels (b) Location of Confirmed Palaeochannels, (c) Palaeochannels Likelihood Mapping (Mote at al. 2009)

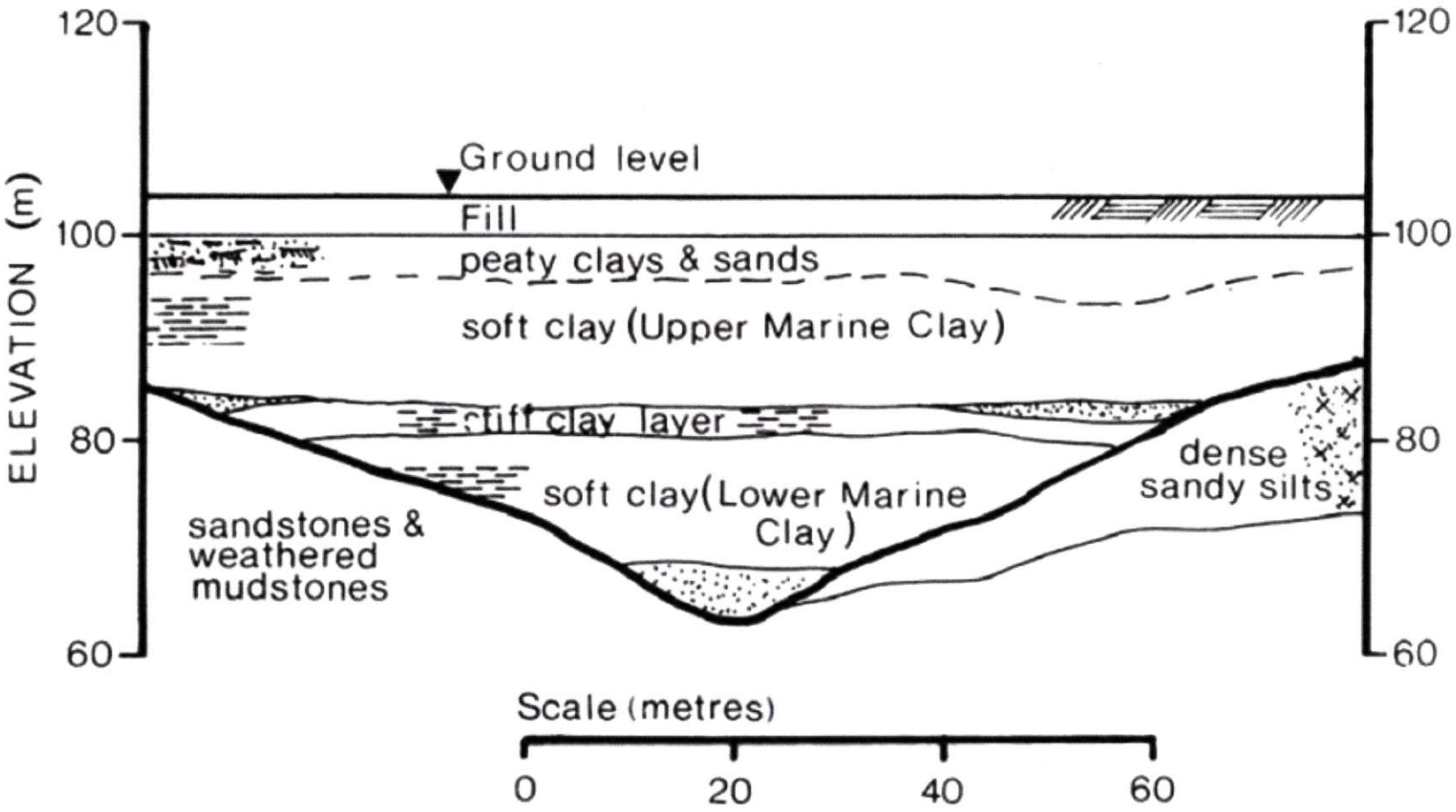

Figure 3-3: Typical Profile in Kallang Formation Area (Davies, 1984)

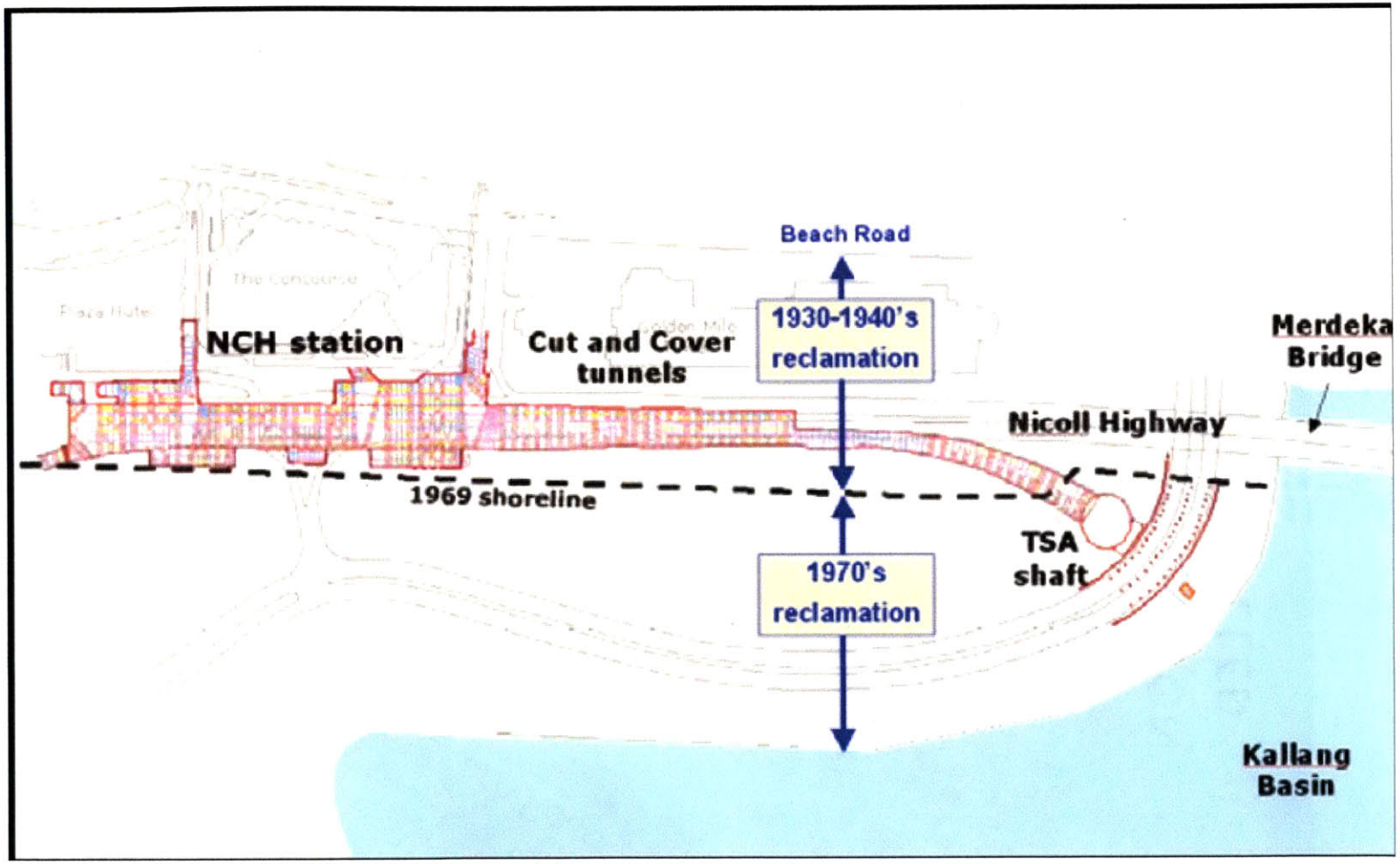

Figure 3-4: Land Reclamations in the 30's & 70's (Davies at al., 2006)

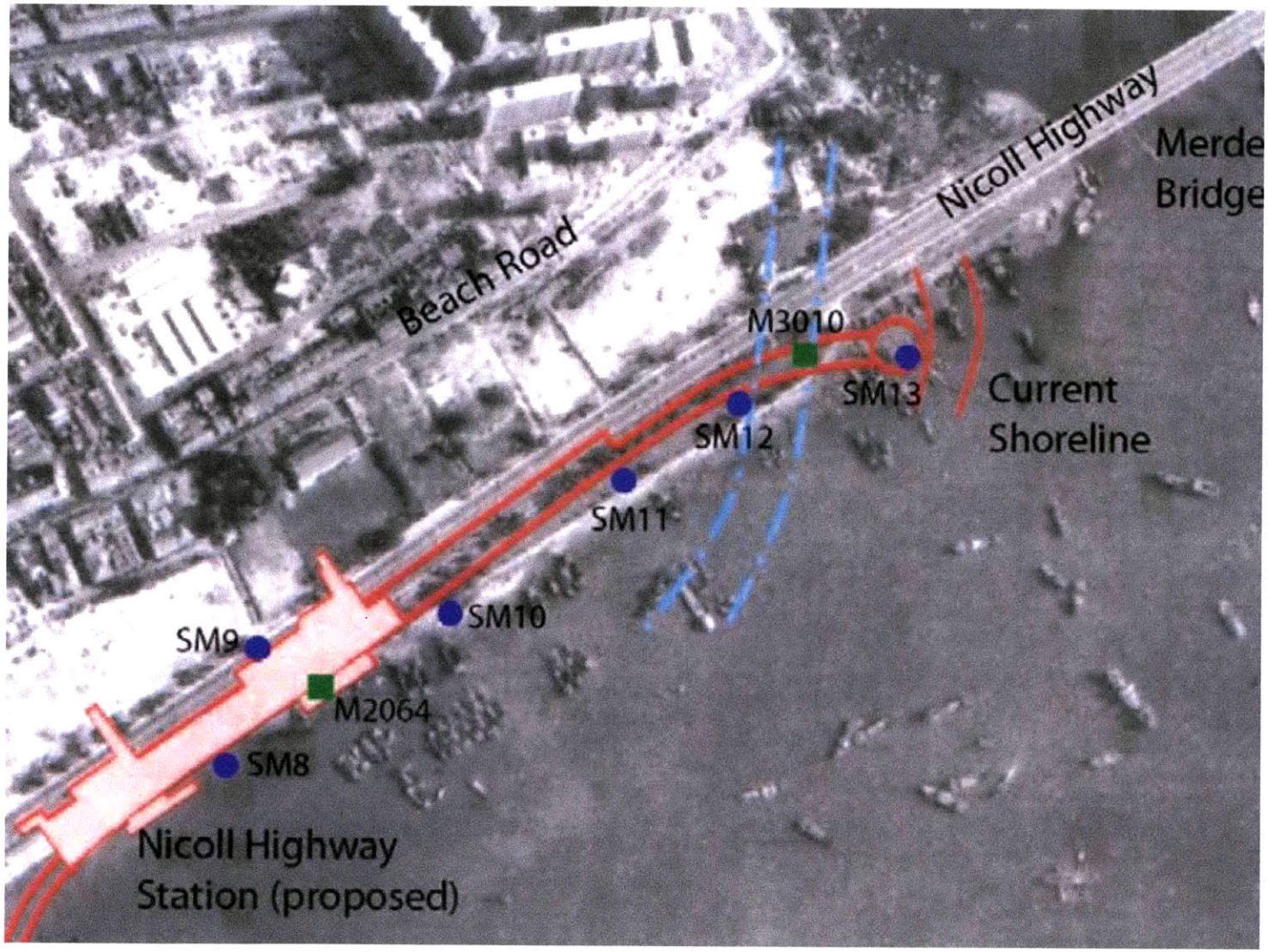

Figure 3-5: Prior Reclamation of Land: Aerial Photo taken 5th April 1969 (Davies at al., 2006)

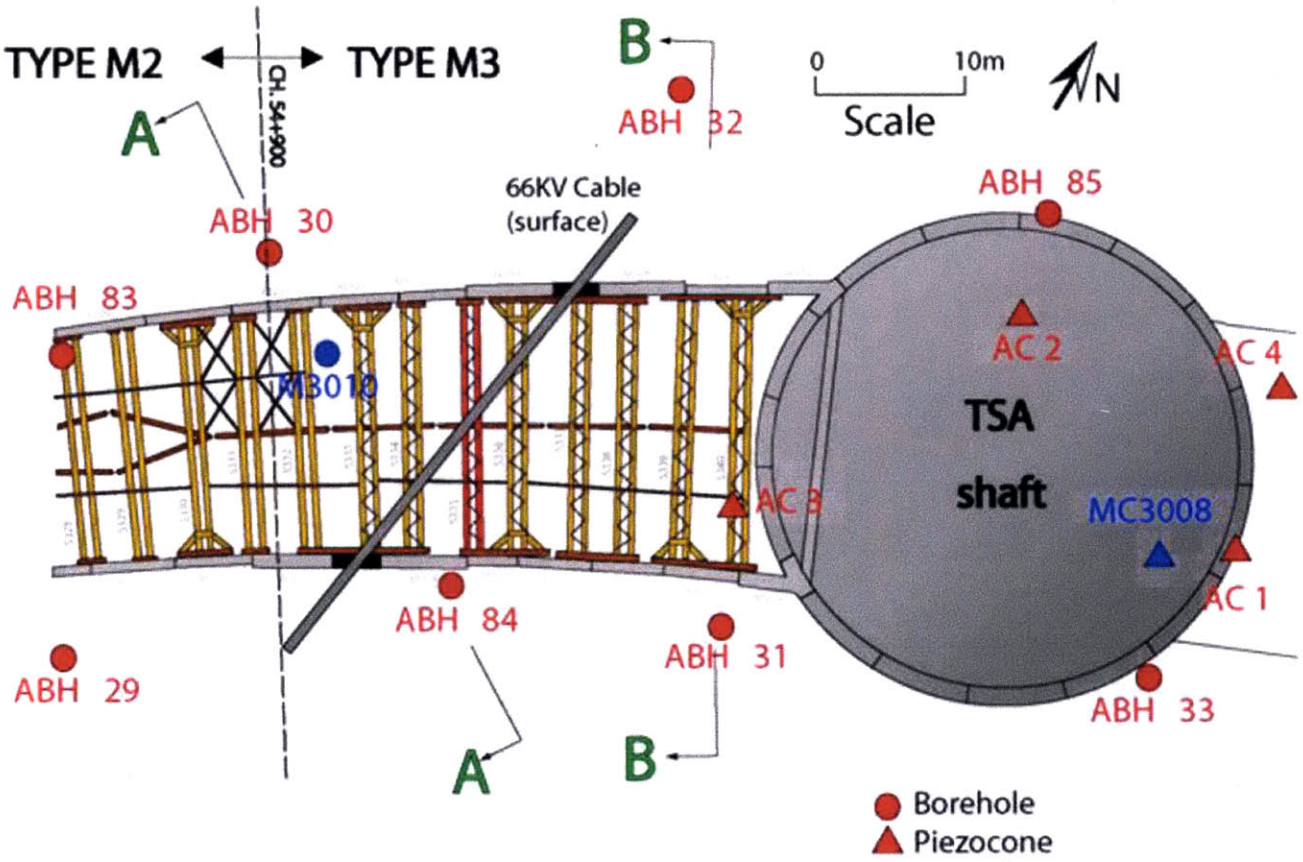

Figure 3-6: **Location of Boreholes, Piezocones & Diaphragm Wall Panels in the M3 section. Blue and red circles and triangles represent the boreholes and piezocones for pre-tender and post-tender, accordingly. (Whittle & Davies, 2006)**

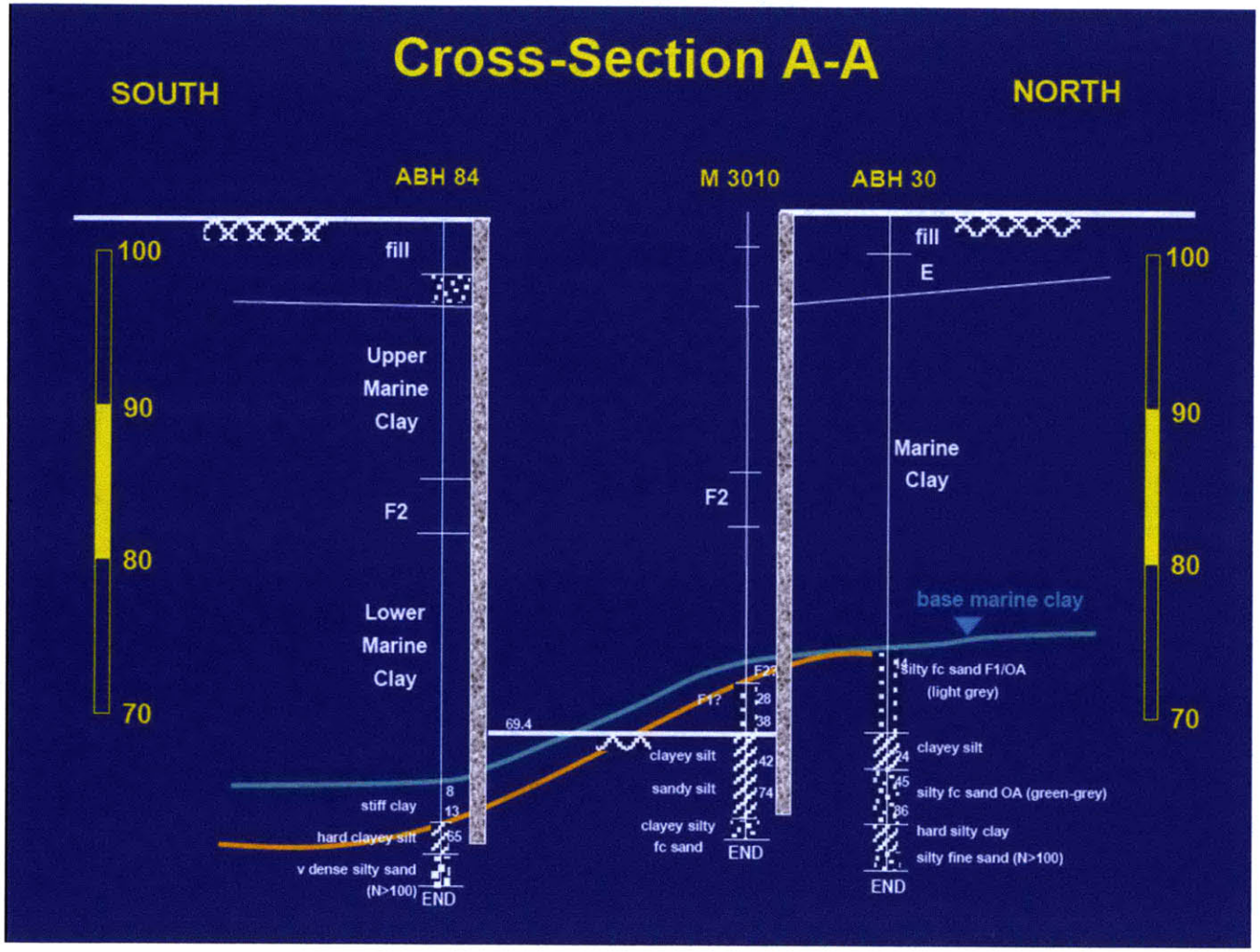

Figure 3-7: Cross Section A-A, showing the Required Final Depth of the Excavation and Variations of OA & LMC (Davies at al. 2006)

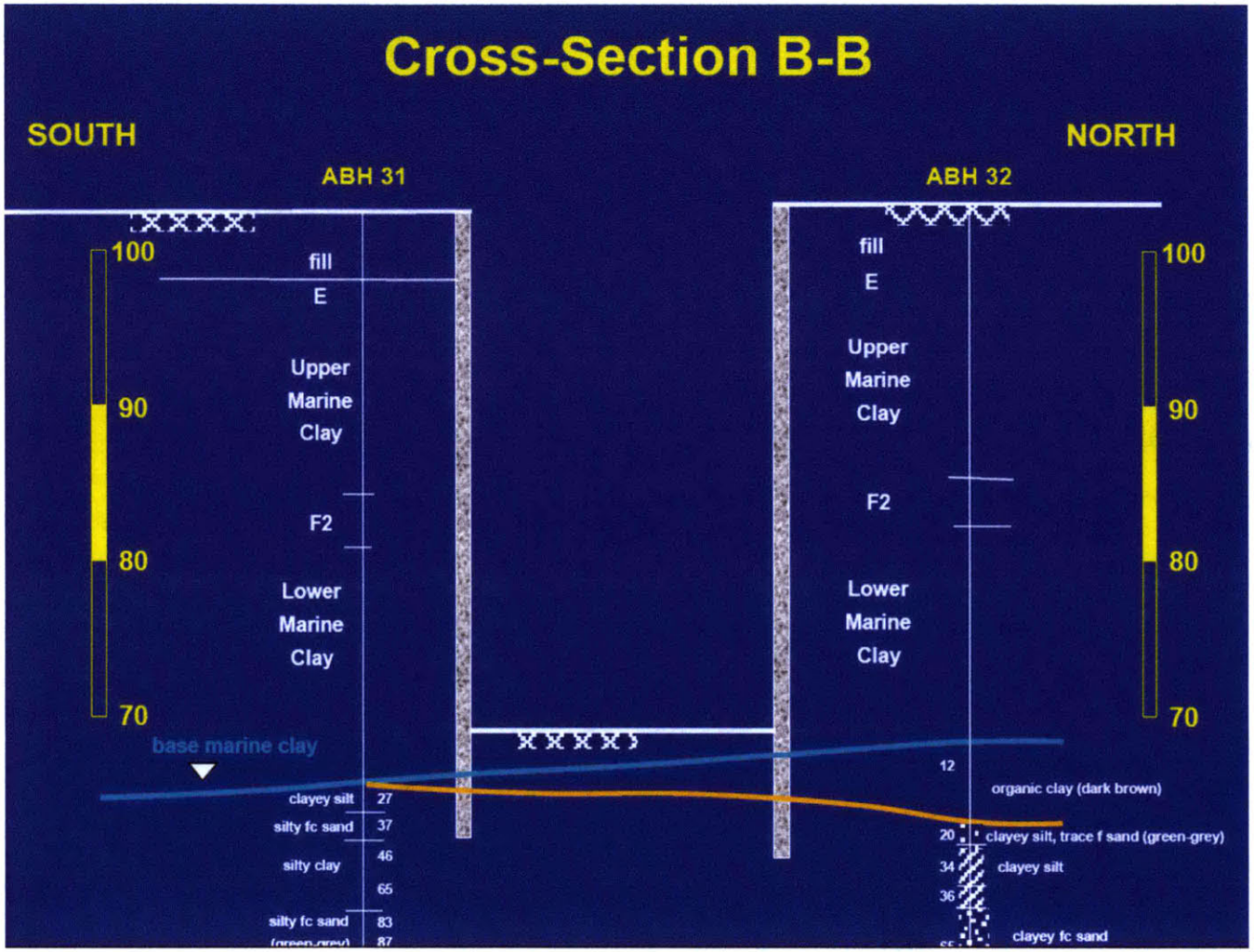

Figure 3-8: Cross Section B-B, showing the Required Final Depth of the Excavation and Variations of OA & LMC (Davies at al. 2006)

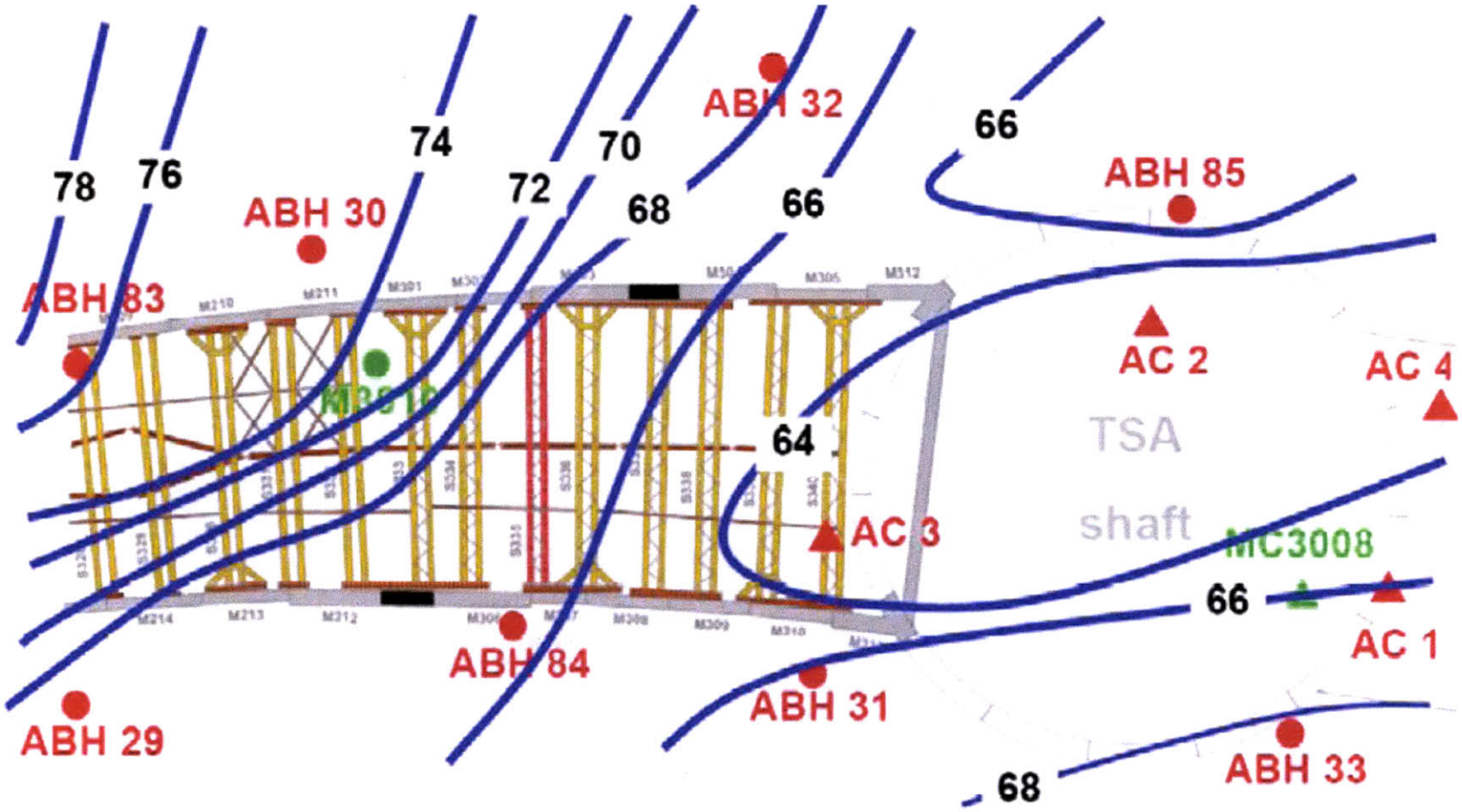

Figure 3-9: Contours of base of Lower Marine Clay, in m, RL (Whittle & Davies, 2006)

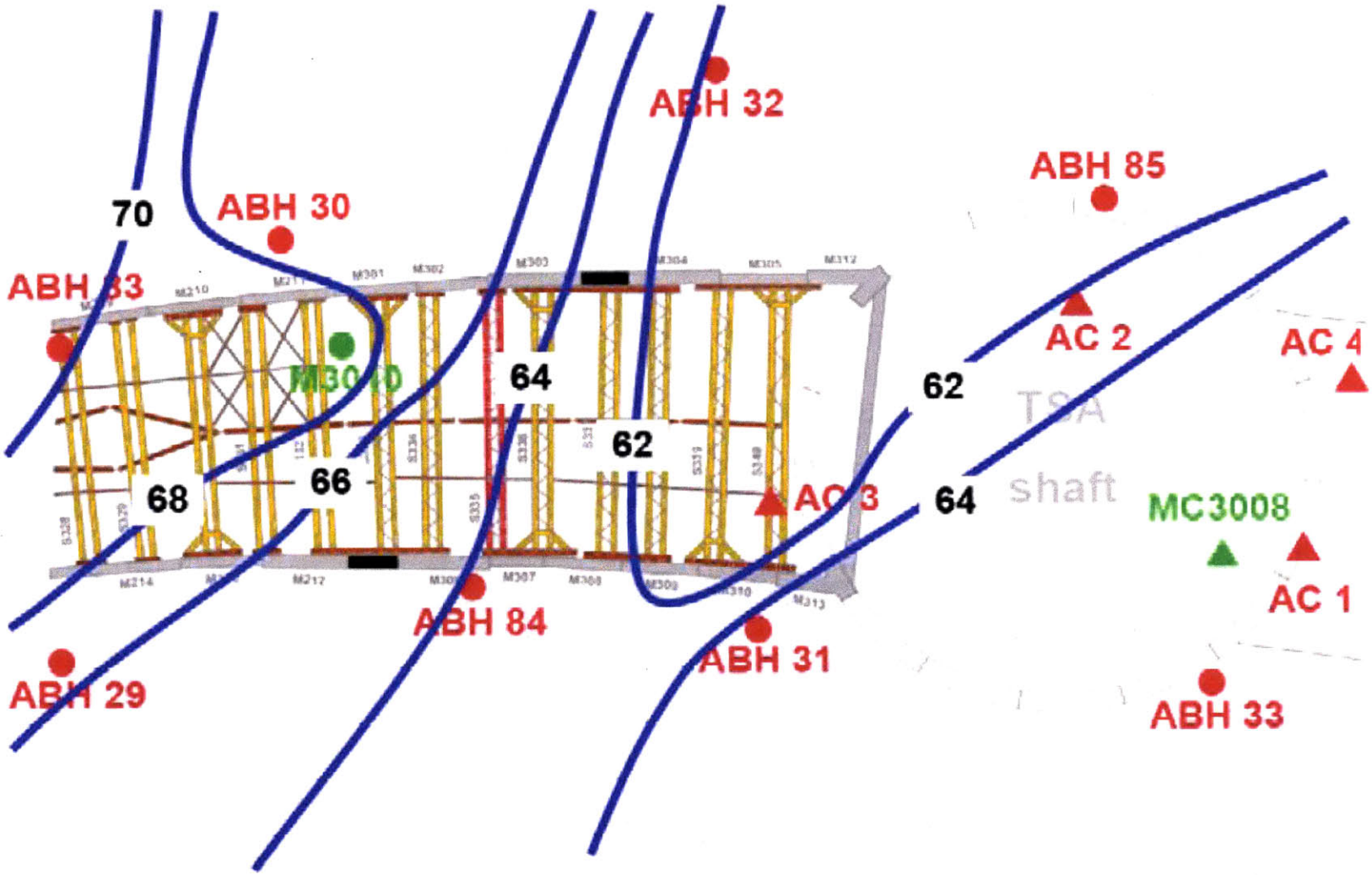

Figure 3-10: Contours of top of Old Alluvium (for N_{spt}>30), in m, RL (Whittle & Davies (2006)

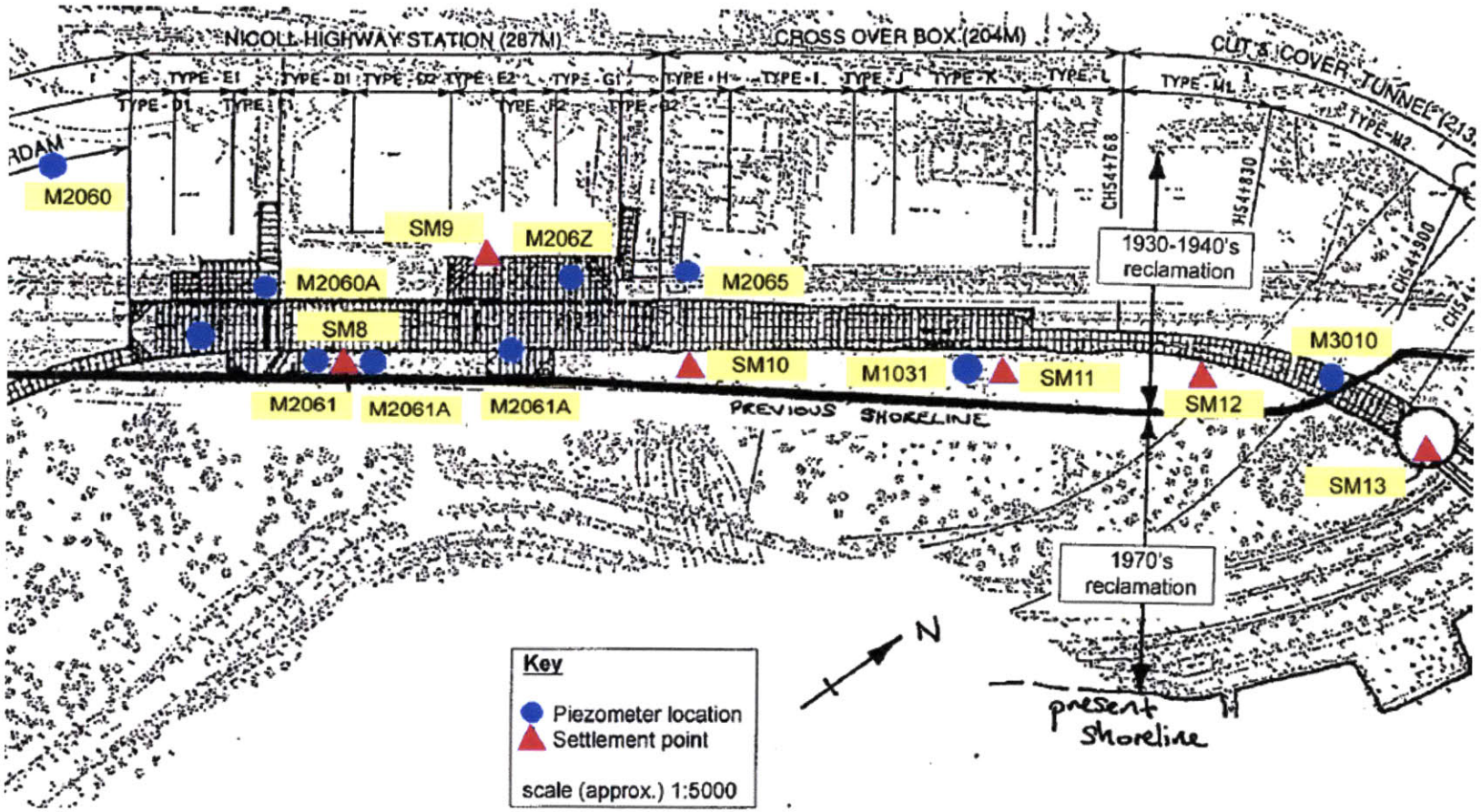

Figure 3-11: Locations of Piezometer & Settlement Points and Reclamation History (COI, 2005)

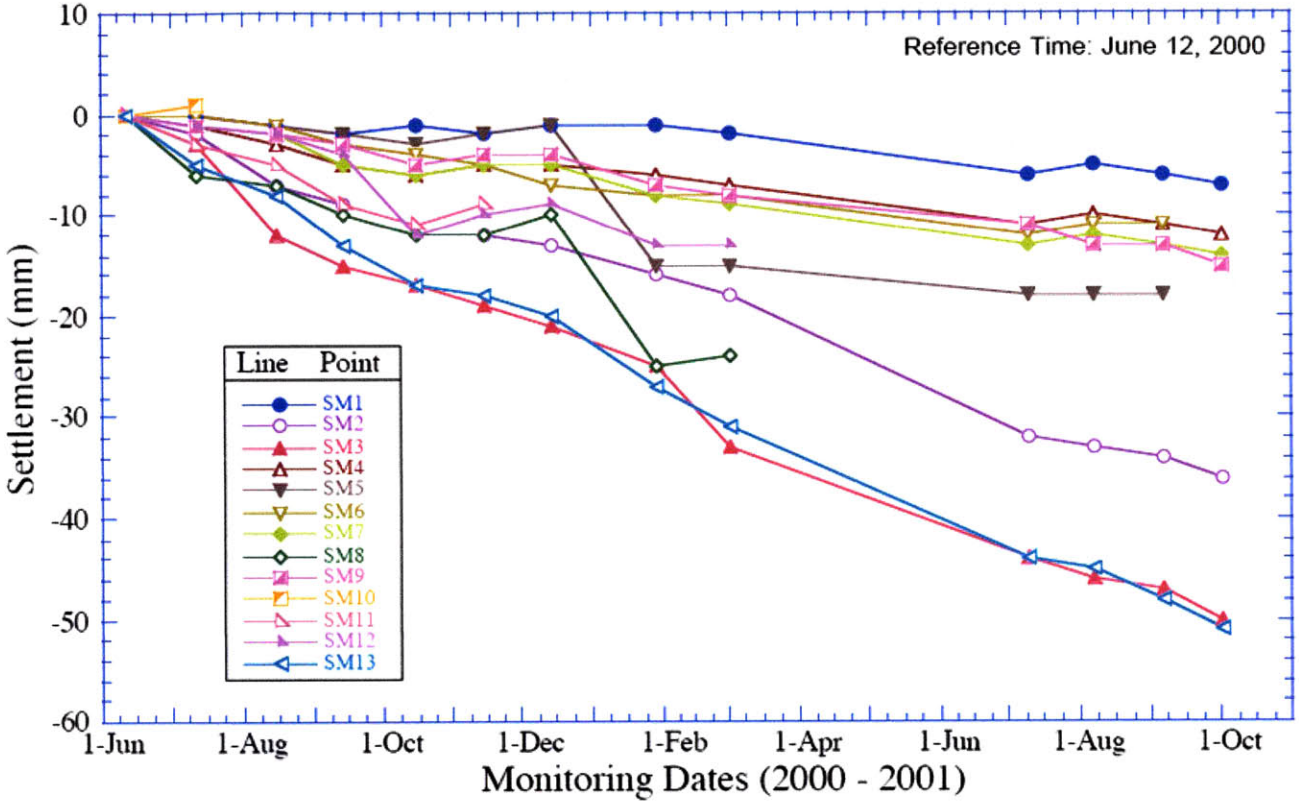

Figure 3-12: Ground Surface Settlement Measured prior to Construction (Whittle & Davies, 2006)

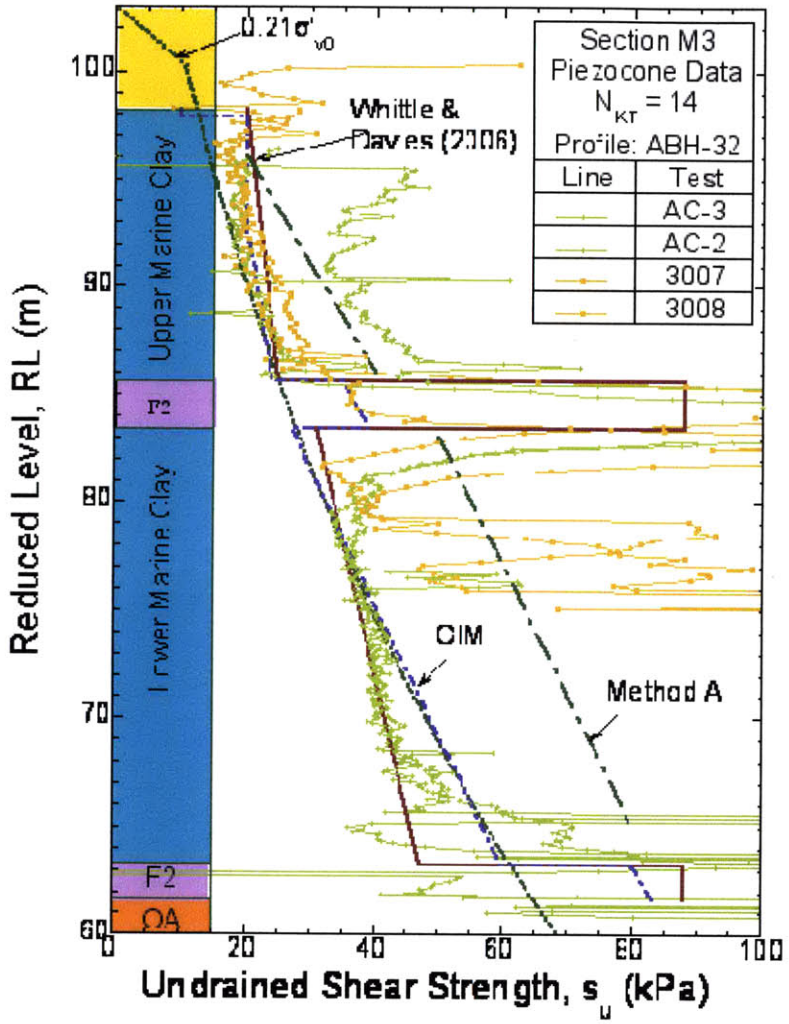

Figure 3-13: Undrained shear strength profiles (Corral & Whittle, 2010)

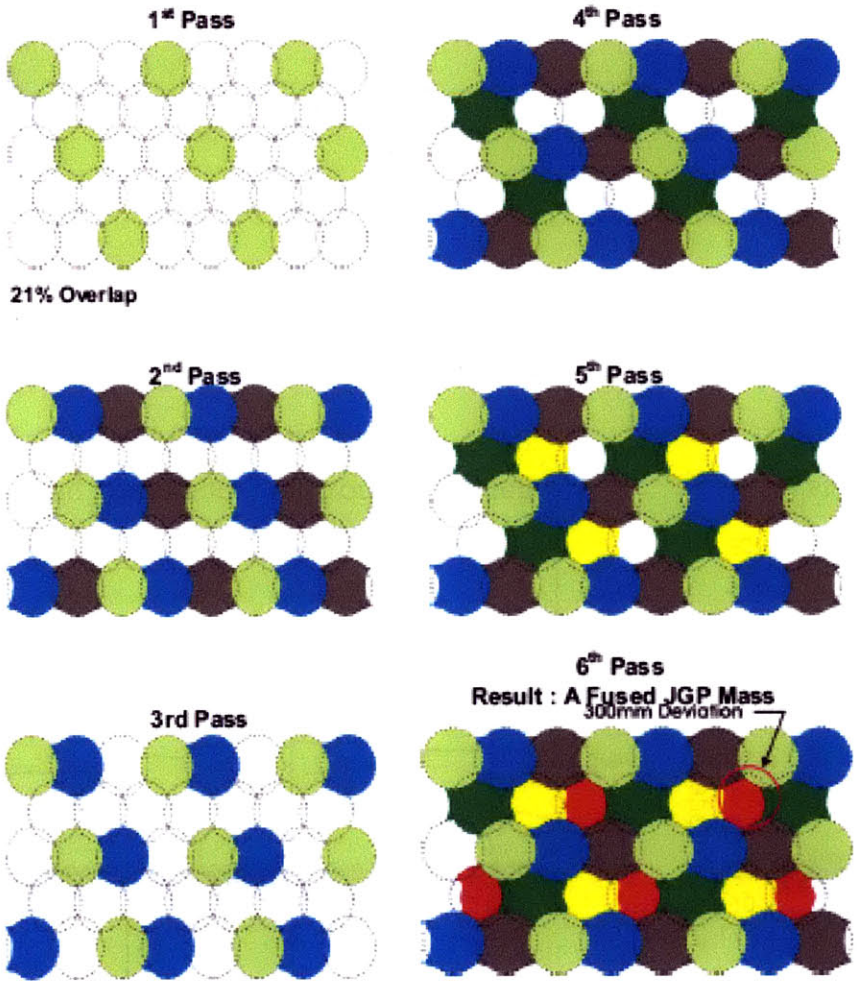

Figure 3-14: Construction Sequence for JGP slabs (COI, 2005)

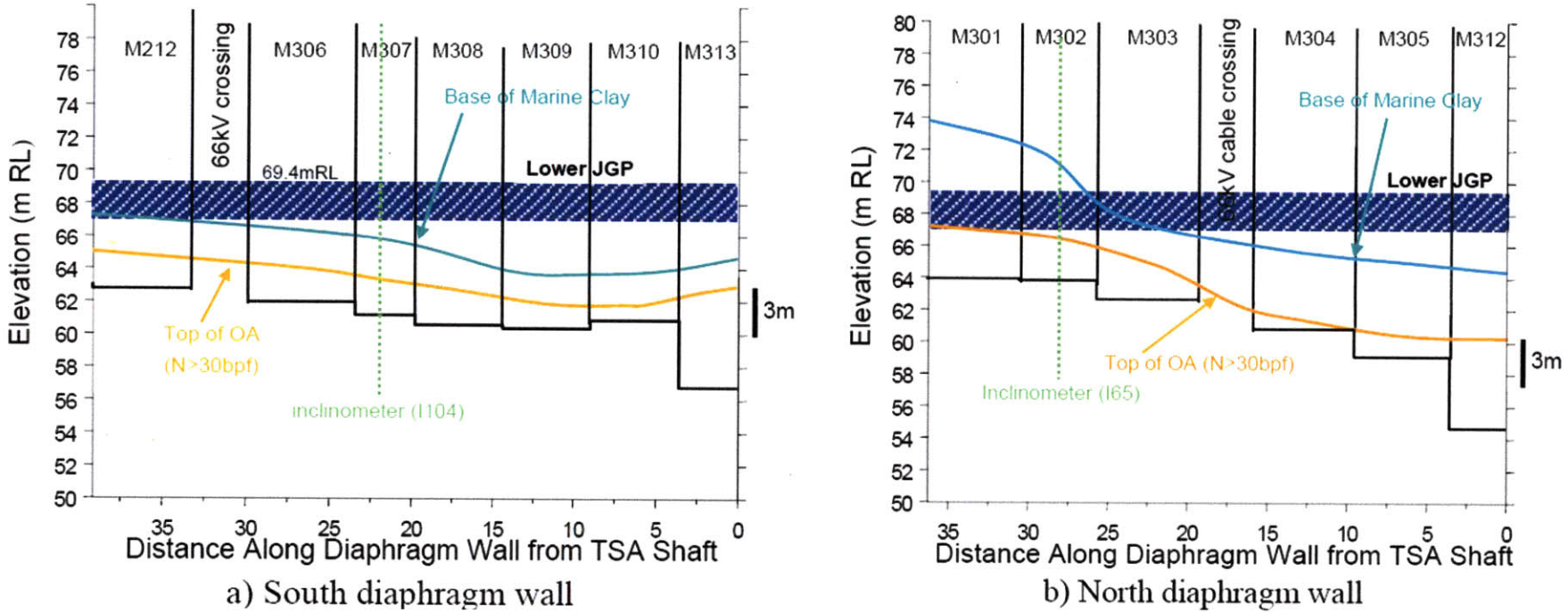

Figure 3-15: Summary of As-Built South & North Diaphragm Wall Panel Embedment in M3 area (Whittle & Davies, 2006)

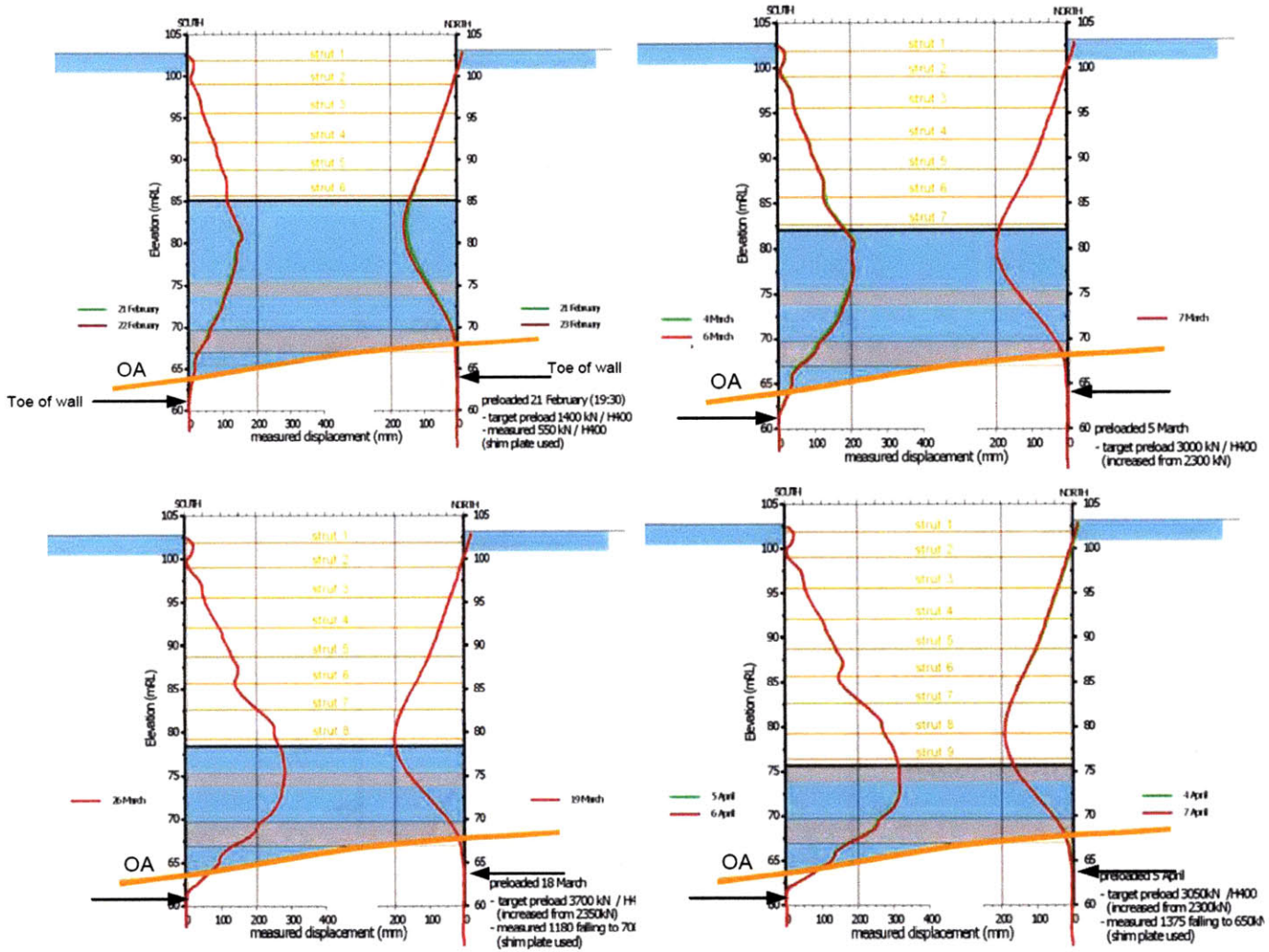

Figure 3-16: Lateral Wall Deflection Measurements for Excavation Levels 6, 7, 8, & 9 (Davies at al., 2006)

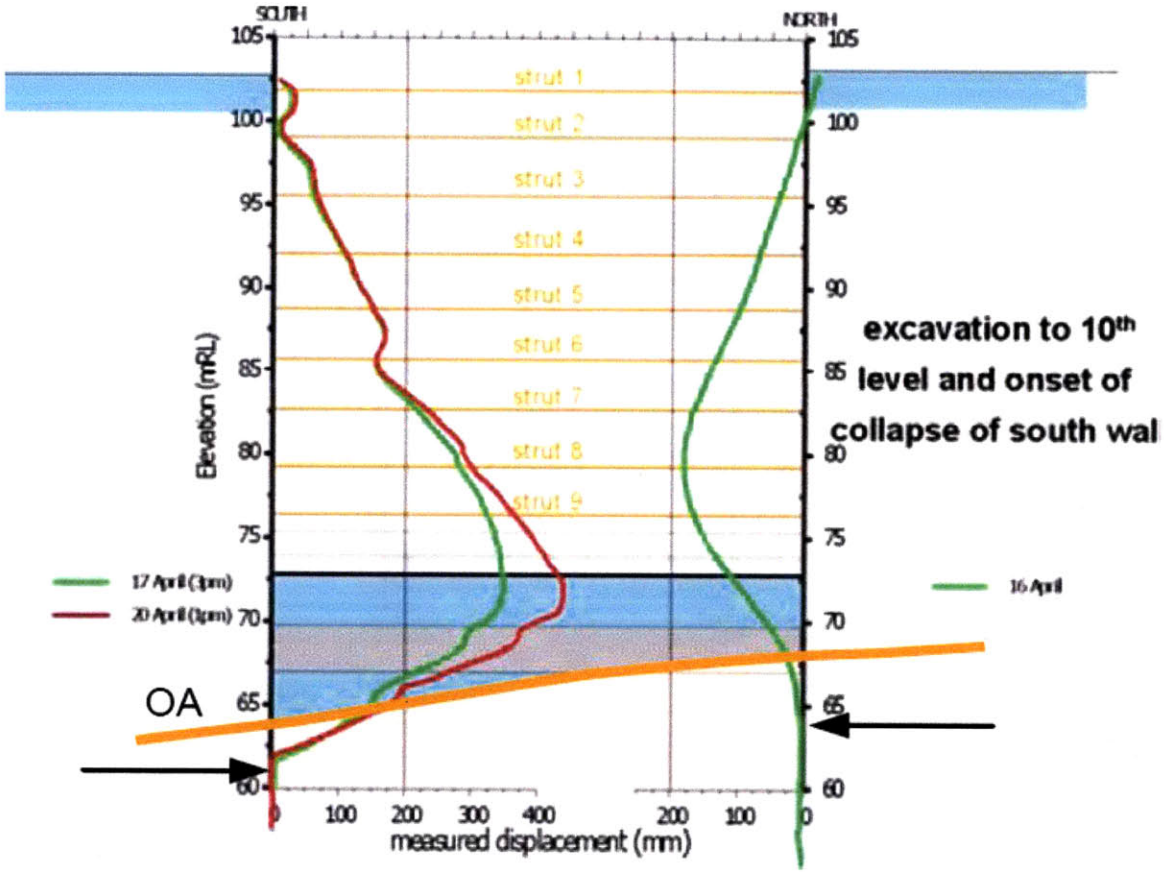

Figure 3-17: Lateral Wall Deflection Measurements for Excavation Level 10 (Davies at al., 2006)

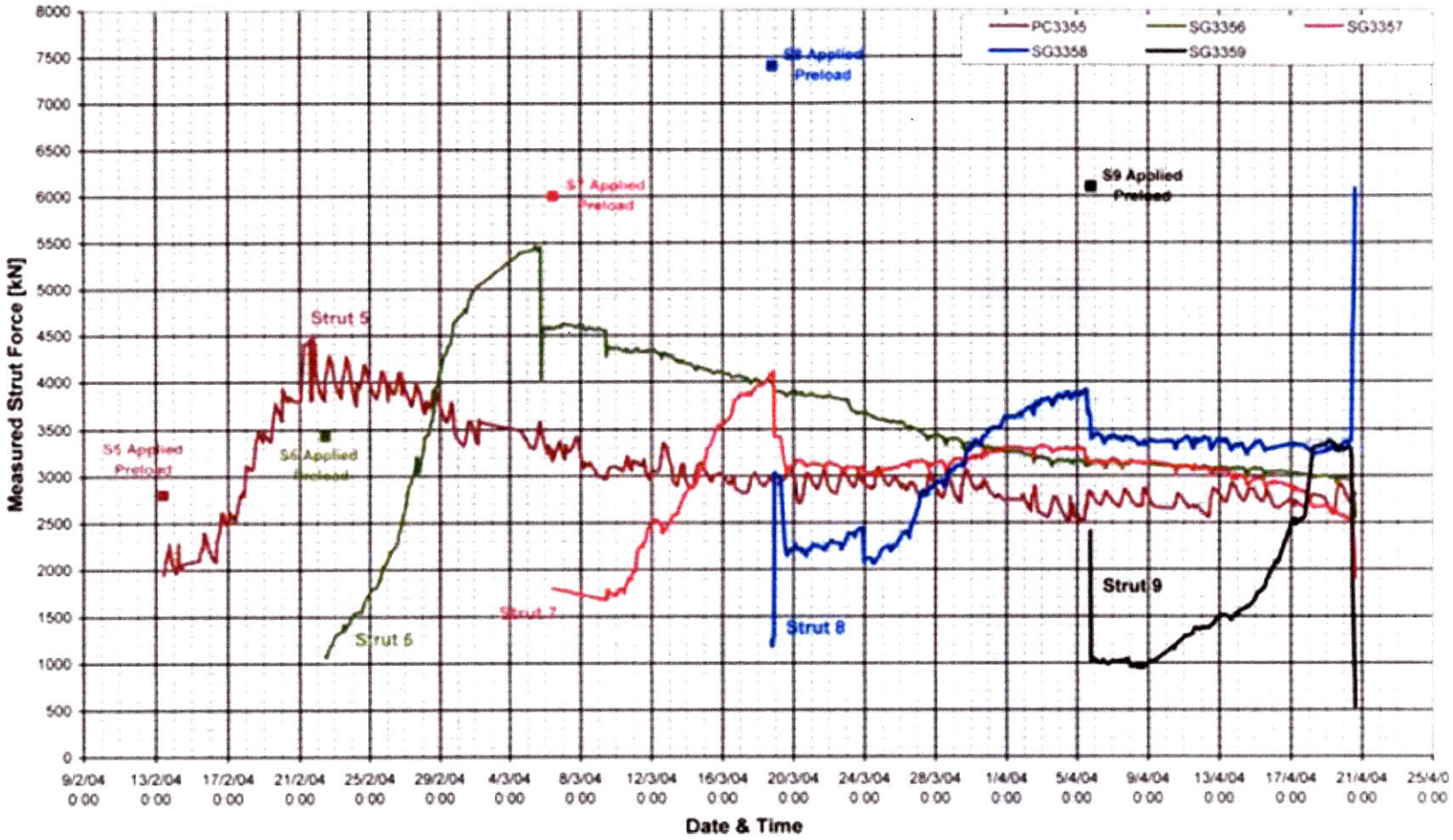

Figure 3-18: Summary of S335 Strut Load Data vs. Date & Time (Whittle, 2006)

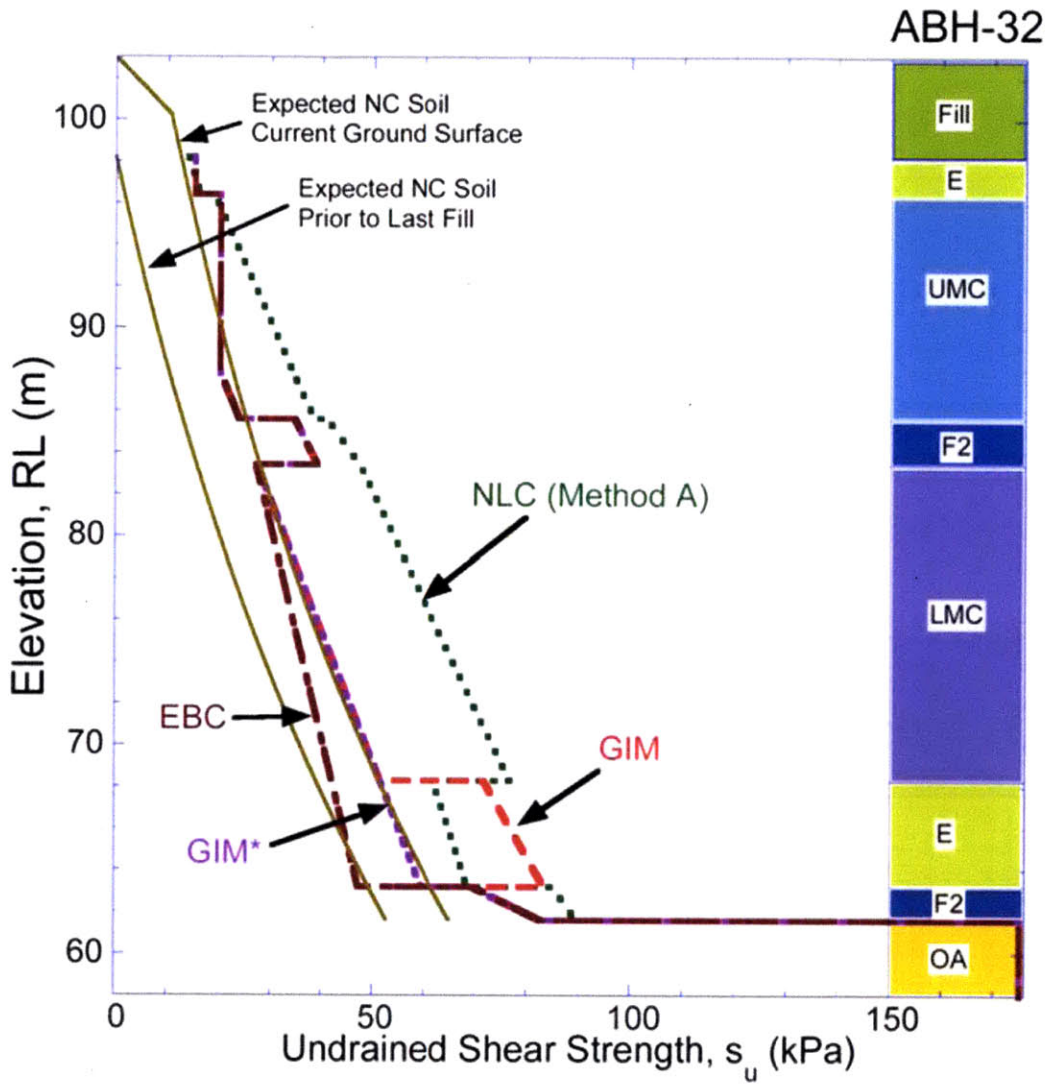

Figure 3-19: Undrained Strength Profiles used in FE simulations for Type M3 Excavation Support System (Whittle & Davies, 2006)

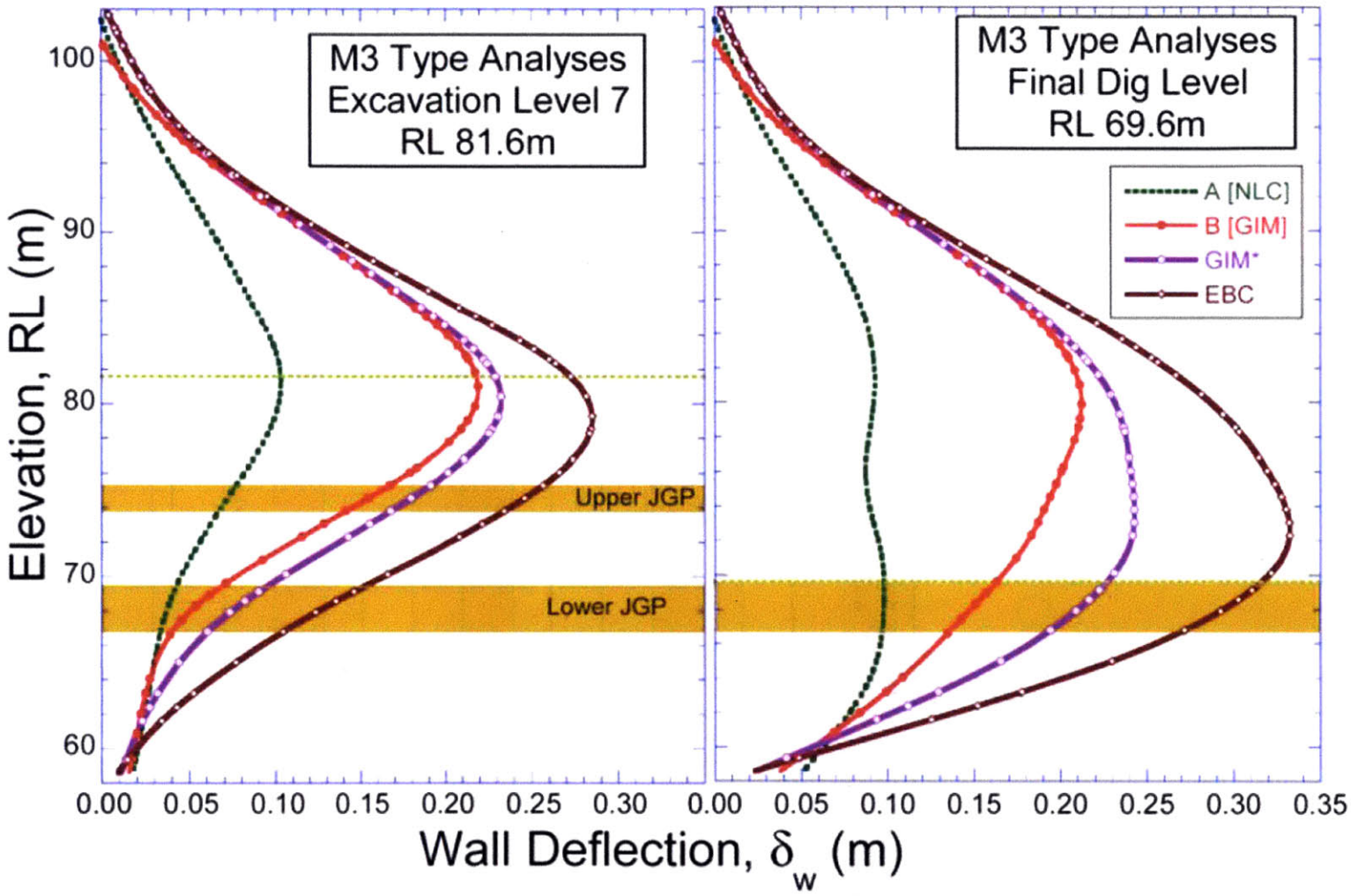

Figure 3-20: Effect of Undrained Shear Strength Profile on Wall Deflections for Type M3 Excavation Support System (Whittle & Davies, 2006)

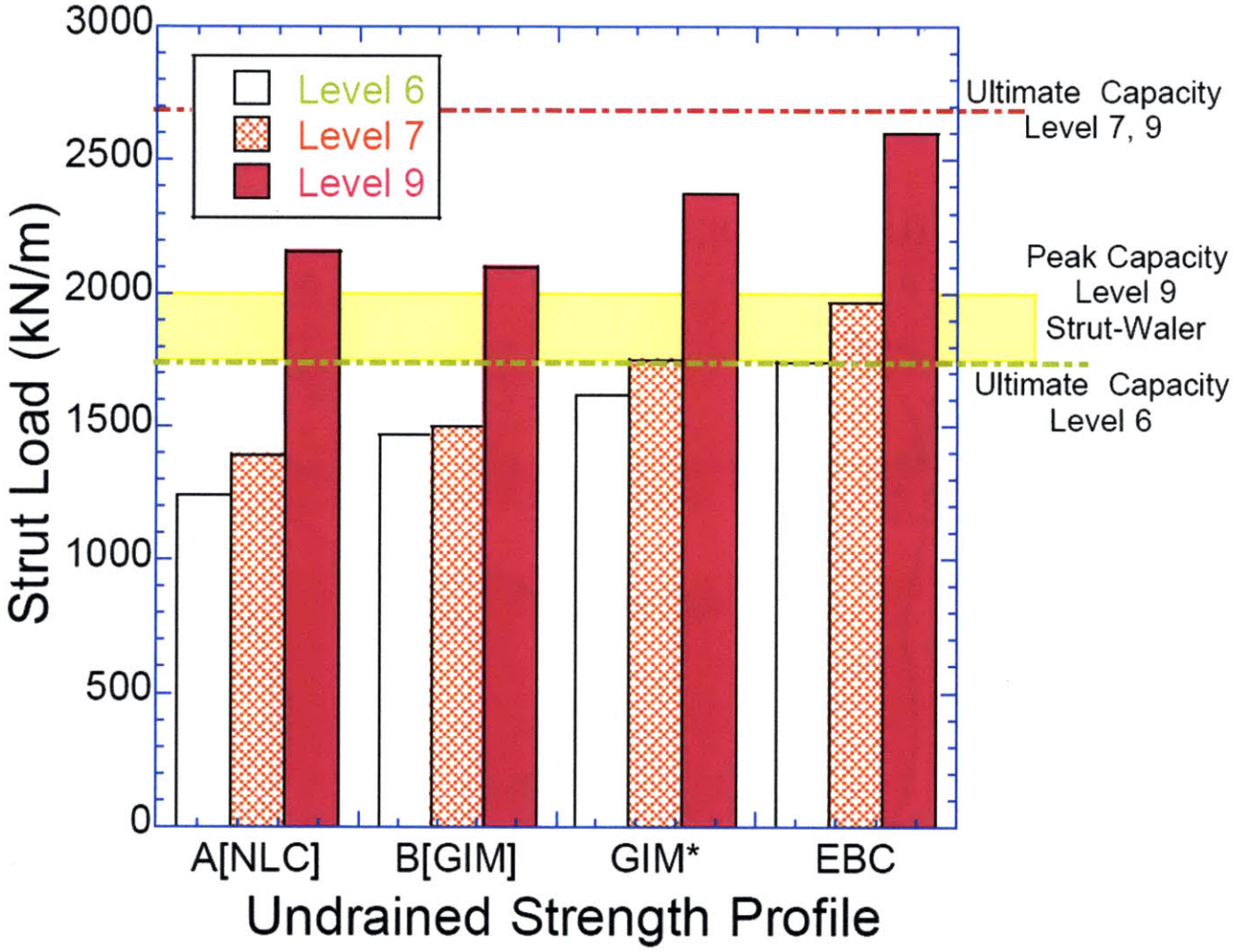

Figure 3-21: Effect of the Analysis Method and Undrained Shear Strength Profile on Computed Strut Loads (Whittle & Davies, 2006)

4 CONSTITUTIVE BEHAVIOR OF KALLANG FORMATION SOILS

4.1. Soil Behavior and Generalized Effective Stress Soil Models

Figure 4-1 illustrates the typical features of the shear-stress-strength properties of clays. The following key points should be noted:

1. The stress-strain properties are non-linear; there is no well defined range of linear behavior.
2. Shearing behavior first loading produces strains that are irrecoverable (i.e. not recovered during unloading).
3. To a first approximation, the unload-reload response is reversible and elastic (although typically non-linear and hysteretic).
4. The highest stiffness (tangent stiffness, Figure 4-1b) occurs immediately upon load reversal.

This behavior is described to a first order approximation by treating the soil as a linearly elastic-perfectly plastic material (EPP), Figure 4-2. The EPP model captures the key difference in stiffness between loading and unloading/reloading. However, it approximates the non-linear stress-strain behavior with an equivalent linear elastic stiffness, while the shear strength is simulated as a plastic flow at constant shear stress.

The EPP modeling of soil behavior is most commonly introduced by relating shear strength to the effective stress Mohr-Coulomb failure criterion, Figure 4-3.

The elastic-perfectly plastic Mohr-Coulomb (MC) soil model is fully defined by five input parameters that specify the linear elastic behavior (E, ν') and yield conditions (c', ϕ'). Perfectly plastic failure occurs when there is no volume change at failure and hence, the dilation angle ψ=0°.

Figure 4-4 shows the undrained effective stress path predicted by the MC for a saturated plane strain[†] soil model. The initial K_0-stress condition is represented by A'. For the undrained shearing in the elastic range, the effective stress path is independent of changes in total stress and is constrained to a condition where Δp'=0 [††] and hence A=0.5 [†††]. This is represented by the effective stress path A'-B' in Figure 4-4. Failure occurs at B' and hence, the undrained shear strength can be found from the initial stresses at the selected drained effective stress parameters (c', ϕ'). Thus:

$$s_u = c' \cos \emptyset' + {}^1/_2 (\sigma'_1 + \sigma'_3) \sin \emptyset' \tag{4.1}$$

$${}^{s_u}/_{\sigma'_{vo}} = {}^{c' \cos \emptyset'}/_{\sigma'_{vo}} + {}^1/_2 (1 + K_0) \sin \emptyset' \tag{4.2}$$

Given these key results the MC model can be defined using either effective stress strength parameters (c', ϕ'; Method A) or using total stress strength parameters (c'=s_u, ϕ'=0; Method B). The key advantage of the MC model is the use of a small number of well-defined parameters for

[†] This is the geometric constraint for 2D FE models of excavation sections.
[††] $p' = 1/3 (\sigma'_{xx} + \sigma'_{yy} + \sigma'_{zz})$ is the mean effective stress.
[†††] $A = 1/3$ corresponds to ESP for undrained triaxial shearing.

which there are extensive empirical data (e.g. GIM, 2001 for C824). As a result, MC is used as the default model in the Plaxis^{TM} program. Prior analyses of C824 performance have also relied heavily on MC parameters to diagnosis the Collapse of Nicoll Highway due to lack of more complete soil stress-strain-strength properties.

4.2. Generalized Effective Stress Soil Models

The goal of generalized effective stress soil models is to represent more reliably the effective stress-strain-strength properties of soils. The models are calibrated to properties measured in well-controlled laboratory element tests and must then be validated using results of more complex tests on boundary value problems.

Most generalized models of clays are based on principles of Critical State Soil Mechanics (CSSM; Schofield and Wroth, 1968) as embodied in Cam Clay models, most notable Modified Cam Clay (MCC; Roscoe and Burland, 1968). The CSSM framework unifies observations on the consolidation and shear behavior of reconstituted clays (under general drainage conditions). The key features of the MCC model can be summarized as follows:

1. Conditions of yielding and large-strain (critical state) shear failure are de-coupled. Plastic yielding is described by a convex yield function, while a separate frictional strength when is used to represent critical state. Figure 4-5 shows that the critical state (CSL) is described by a criterion:

$$q_f = Mp'_f \tag{4-3}$$

where $M = 6\sin\emptyset'_{TC}/(3-\sin\emptyset'_{TC})$, $\emptyset'_{TC}$ is the frictional angle measured in conventional triaxial compression. q_f, p'_f are the shear stress and mean effective stress ($(\sigma'_1-\sigma'_3)$, $1/3(\sigma'_1+2\sigma'_3)$) in triaxial space.

2. MCC assumes an elliptical yield function:

$$f = q^2 - Mp'(p_c' - p') \tag{4-3}$$

where p_c' is the hydrostatic pre-consolidation pressure that defines the size of the surface, Figure 4-5.

3. p_c' is a hardening parameter that changes with plastic volume strain and enables the model to define the virgin consolidation and elastic swelling lines associated with consolidation (associated with compressibility parameters λ, κ; respectively).

During undrained shearing (Figure 4-5), the effective stress path for a clay is controlled by associated plastic flow and hardening of the yield surface (elastic behavior occurs inside the yield function). Figure 4-5 illustrates the typical effective stress path for a normally consolidated clay (with K_0=1). Undrained shearing produces positive shear-induced pore pressures (i.e. $\Delta p'<0$). The undrained strength of the clay is controlled by hardening of the yield surface and the critical state friction parameter (i.e. by input parameters λ, κ and M).

Although the MCC model is very well known in geotechnical engineering it is not used so extensively in practice. This is due in part, to some key limitations of the modeling representing the elemental behavior of K_0-consolidated clays:

1. It assumes that undrained shear strength is only mobilized at large strain critical state conditions. In contrast, there is extensive empirical data, especially for NC clays, that show the occurring at relatively small shear strains, and at stress ratios q/p' far from critical state.
2. It assumes isotropic behavior, such that the shear strength is independent of the direction of shearing. This is also contrary to the wealth of experimental data that find shear strength of natural of natural clays are strongly dependent on the direction of major principal stress at failure.
3. It assumes elastic behavior inside the yield surface and hence, does not describe accurately the observed non-linear and characteristic stress-strain properties of overconsolidated clays.

There has been extensive research to develop more reliable generalized effective stress soil models for describing the rate-independent behavior of normally to moderately overconsolidated clays. Whittle (1987) and Whittle and Kavvadas (1994) describe the formulation of MIT-E3. Figure 4-6 illustrates the conceptual framework for this model for the case of hydrostatic compression. The model comprises 3 concepts:

1. An elastoplastic model for normally consolidated clay that describes the anisotropic and strain-softening behavior (corresponding to behavior on the VCL, A, Figure 4-6).
2. Equations to describe the small strain non-linearity and hysteric response in unloading and reloading (A-B-A, Figure 4-6a).

3. Bounding surface plasticity for irrecoverable, anisotropic, and path-dependent behavior of overconsolidated clays (reload path B-C with irrecoverable stress Δ^p, Figure 4-6b).

The anisotropic behavior of normally consolidated clays is described by introducing a generalized yield function with hardening parameters that control the size of the surface (α') and its orientation (**b**); Figure 4-7.

$$f = (\boldsymbol{s} - \sigma'\boldsymbol{b}) : (\boldsymbol{s} - \sigma'\boldsymbol{b}) - c^2\sigma'(2\alpha' - \sigma') = 0 \tag{4-4}$$

where c is the ratio of the semi-axes that defines the shape of the surface.

The model is able to describe the VCL using density hardening similar to MCC; while evolving anisotropic properties that are predicted through changes in orientation of the surface. The formulation assumes that the stress state of a K_0-normally consolidated soil is at the tip of the yield surface:

$$(\sigma', \boldsymbol{s}) = 2\alpha'(1, \boldsymbol{b}) \tag{4-5}$$

Anisotropic shear failure at large strains is modeled using a critical state failure criterion (Figure 4-7)

$$h = (\boldsymbol{s} - \sigma'\boldsymbol{\xi}) : (\boldsymbol{s} - \sigma'\boldsymbol{\xi}) - k^2\sigma'^2 = 0 \tag{4-6}$$

where $\boldsymbol{\xi}$ represents the orientation (anisotropy) tensor for critical state failure criterion.

The model formulations assumes that the orientation tensor is completely defined by both large strain friction angles measured and the triaxial compression and extension (ϕ'_{TC} and ϕ'_{TE}).

The unload-reload behavior in MIT-E3 is specified by a formulation that described a closed-symmetric hysteresis loop in the strain-stress response. The model requires the detection of a stress reversal point and functions to describe the non-linear stiffness relative to the reversal point. The volumetric response (Whittle and Kavvadas, 1994) is described by a tangent bulk modulus, K:

$$K = \frac{1+e}{(1+\delta)\kappa_0}\sigma' \tag{4-7a}$$

where $$\delta = Cn(log_e\xi + \xi_S)^{n-1} \tag{4-7b}$$

with κ_0, C, n constant parameters that are calibrated to measured data, while ξ and ξ_S are stresses defined relative to the reversal point. For hydrostatic swelling, $\xi = \sigma'_{rev}/\sigma'$ is a measure of the overconsolidation ratio (defined in terms of mean stress)[†].

Figure 4-8 illustrates typical swelling behavior from the formulation for ranges of the parameters (C, n). The value of κ_0 is derived from small strain elastic properties (or alternatively from G_{max}).

Figure 4-9 shows typical predictions of the undrained shear behavior K_0-normally consolidated clay using MIT-E3 (in triaxial compression and extension modes). The model is able to describe key features of the observed effective stress paths and shear stress strain behavior in these two

[†] ξ_S relates to changes in the stress ratio ($\eta = S/\sigma'$)

laboratory element modes. In particular it is able to predict describe realistically the undrained strength anisotropic and characteristic stress-strain properties.

4.3. Calibration of MIT-E3 for Marine Clays

This section describes calibration of MIT-E3 model of units of the Upper and Lower Marine Clay at C824. This is made possible by a program of high quality laboratory tests carried out by Kiso-Jiban (unpublished) as part of the post-failure site investigation at the site of the Nicoll Highway Collapse.

The complete description of the MIT-E3 model is much more complex than MC and requires calibration of 15 input parameters. Of these parameters, 7 can be identified unambiguously following Whittle and Kavvadas (1994):

1. $\boldsymbol{K_{ONC}}$ is the coefficient of lateral earth pressure (geostatic) normally consolidated clay that can be estimated from empirical formulas or measured during K_O-consolidation in either triaxial test or an oedometer with lateral stress measurements.
2. $\boldsymbol{\lambda}$ and $\boldsymbol{e_O}$ define the slope of the virgin consolidation line in $(e - \log_e \sigma')$ space, and can be obtained from an oedometer or CRS test.
3. $\boldsymbol{2G/K}$ is the ratio of the tangential elastic shear modulus to the bulk modulus can be expressed in terms of the Poisson's ratio, as Equation (46). In addition, if the OCR at $K_O = 1$ is known (OCR_I), the ratio can be estimated from Equation (47).

$$\frac{2G}{K} = \frac{3(1-2\nu)}{(1+\nu)} \tag{4-8}$$

$$\frac{2G}{K} = \frac{(1-K_{ONC})OCR_1}{\frac{1}{3}(1+2K_{ONC})OCR_1-1} \quad (4\text{-}9)$$

4. $\boldsymbol{\kappa_O}$ is the elastic bulk modulus at small strains levels (i.e. K_{MAX} at stress reversal) should be estimated from the elastic shear wave velocity (G_{MAX}) measured either by lab resonant column tests or field investigations.
5. $\boldsymbol{\phi'_{TC}}$ and $\boldsymbol{\phi'_{TE}}$ are the friction angles for shearing at the critical state conditions in triaxial compression and extension modes of shearing (for practical proposes these friction angles can be estimated at 10% of axial strain from undrained triaxial shear tests).

The remaining eight input parameters must be determined by parametric studies (i.e. indirectly):

1. $\boldsymbol{C, n}$ define the non-linearity in the volumetric response for the perfectly hysteretic formulation are selected to match the swelling behavior in an oedometer or CRS test as shown in Figure (4-21).
2. $\boldsymbol{\psi_O}$ is a dimensionless constant that controls the rate of change of anisotropy caused by the strain or stress history. The most useful lab tests are drained strain controlled tests (i.e. drained strain path tests).
3. $\boldsymbol{S_t}$ and $\boldsymbol{c}$ control the strain softening (principally in compression mode of shearing) and the undrained strength in the compression and extension modes of shearing are established from the undrained shear behavior of a K_O-normally consolidated clay (preferably form Triaxial CK_OUC and CK_OUE tests).

4. $\boldsymbol{\omega}$ controls the non-linear behavior during undrained shearing at small strain levels and/or when the stress state is far from the bounding surface can be obtained from measurements of the secant shear modulus in the small strain range ($\varepsilon_a = 0.001 - 0.05\%$) from undrained triaxial compression tests on lightly OC clay ($OCR = 1.5 - 2.0$).
5. $\boldsymbol{h}$ defines the amount of residual plastic strain Δ_P observed in hydrostatic unload-reload cycles.
6. $\boldsymbol{\gamma}$ represents the development of shear-induced pore pressures during undrained shearing of OC clays. For further explanation refer to the paper by Whittle & Kavvadas, 1994.

Table 4-1 summarizes these input parameters, their physical meanings within the model formulation and laboratory tests from which they can be obtained, together with parameters selected for UMC and LMC units. The parameters have been derived principally from a set of 1-D consolidation tests (Figure 4-10) and K_0-consolidated undrained triaxial shear tests (Figure 3-11) on specimens reconsolidated to the in situ stress conditions.

The compressibilities of the normally consolidated UMC and LMC units are well-characterized virgin consolidation lines with $\lambda = 0.37 - 0.38$, Figure 4-10a. The upper marine clay generally has higher in situ void ratio ($e = 1.7 - 1.9$) than the lower unit ($e = 1.5 - 1.6$). The marine clays show significant elastic rebound when unloaded. Figure 2b shows that recoverable axial strains, $\Delta\varepsilon_a$ = 10-12% when the effective stress is reduced by one order of magnitude (ξ_v = OCR = 10). This behavior is consistent with laboratory measurements of the maximum shear modulus, G_{max},

(from bender elements), reported by Tan et al. (2003). The Authors have used these data to estimate the model input parameter, κ_0, and then selected input values of C, n (Table 4-1) to the swelling data as shown in Figure 4-10b.

A series of CAU normally consolidated triaxial compression and extension tests were performed on specimens from 4 depths within the UMC and LMC units, Figure 4-11.

All of the specimens were consolidated to a common lateral stress ratio, $K_0 = 0.52$ prior to shearing. The measured data show a significant different in the average undrained triaxial compression strength ratios measured in these tests, $s_{uTC}/\sigma'_{vc} = 0.30$ vs. 0.27 for the UMC and LMC units, respectively. The data also show that UMC specimens mobilize higher friction angles when sheared to large strains (in both compression and extension), $\phi' = 32.4° - 33.8°$ vs. 27.0° - 27.1° for UMC and LMC. The UMC exhibits higher undrained strength anisotropy, $s_{uTE}/s_{uTC} = 0.60 - 0.66$ compared to LMC (0.80 – 0.88) and both exhibit relatively modest post-peak softening in compression shear modes for $\varepsilon_a > 2\%$.

Details of the measured effective stress paths and shear stress-strain properties are well characterized by MIT-E3 through model input parameters c, S_t, ϕ'_{TC}, ϕ'_{TE}, ω and γ (Table 4-1). The remaining parameters in Table 4-1 have been estimated from prior studies on similar clays.

4.4. Parameters of Other Soil Units at C824

There are no direct laboratory data on the other soil units at S335. Hence, the current analyses use the MC model for these layers based on parameters specified in GIM (2001) or defined by Whittle and Davies (2006), see Table 4-2. These properties are used throughout the subsequent analyses.

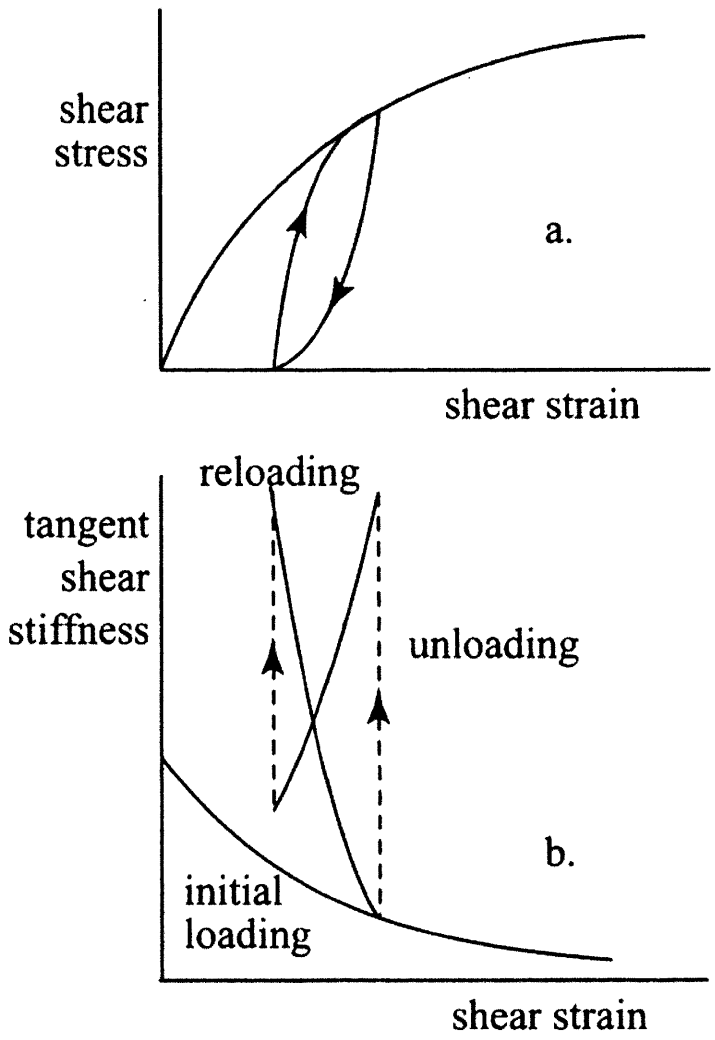

Figure 4-1: (a) Typical Irreversible Stress-Strain Response, and (b) Typical Modulus Variation for Soil (Muir Wood, 2004)

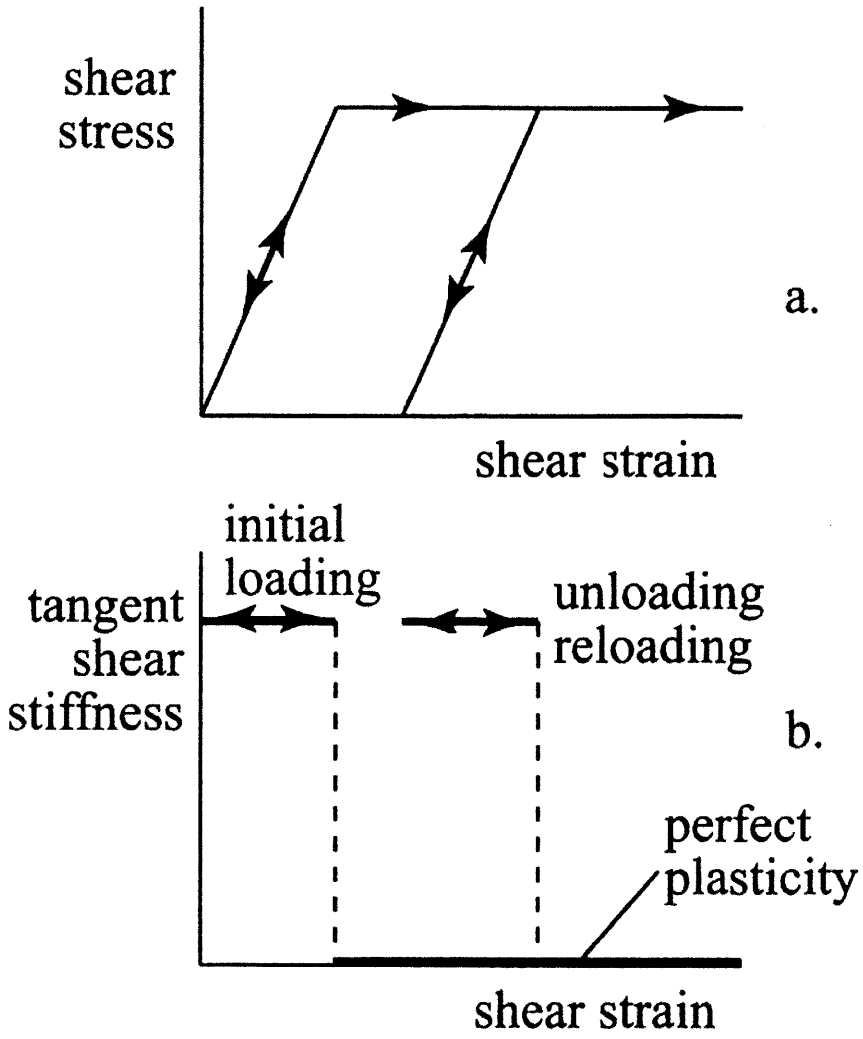

Figure 4-2: Elastic-Perfectly Plastic Model: (a) Stress-Strain Response & (b) Modulus Variation (Muir Wood, 2004)

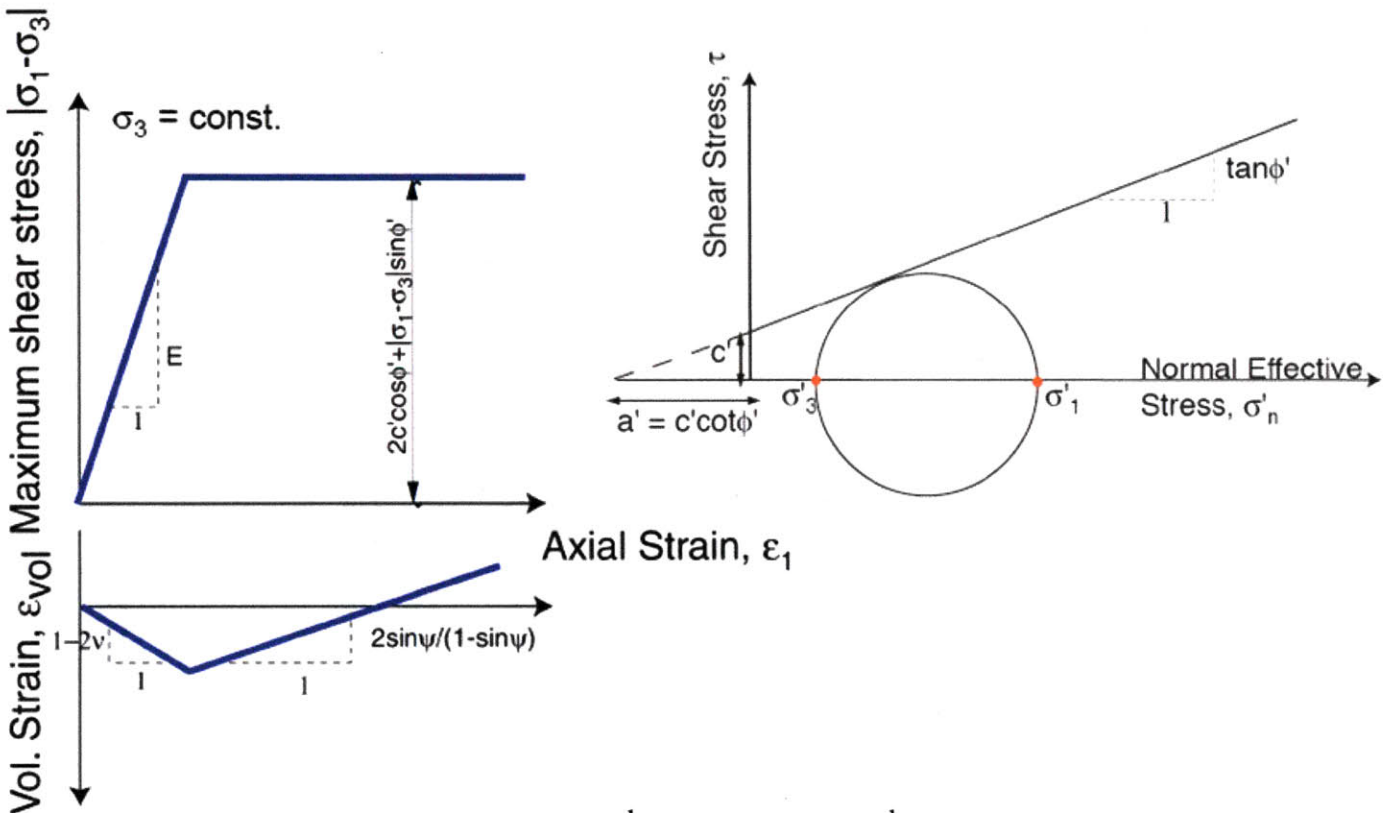

Notes: 1) Yield Function $f = \frac{1}{2}(\sigma'_1+\sigma'_3)\sin\phi' - \frac{1}{2}(\sigma'_1-\sigma'_3) + c'\cos\phi'$

2) $\psi = f(\phi'-\phi'_{cv})$, perfectly plastic case $\psi = 0$

3) where ϕ'_{cv} is the constant volume friction angle

Figure 4-3: Mohr-Coulomb Model Representation for a Drained Triaxial Shear Test

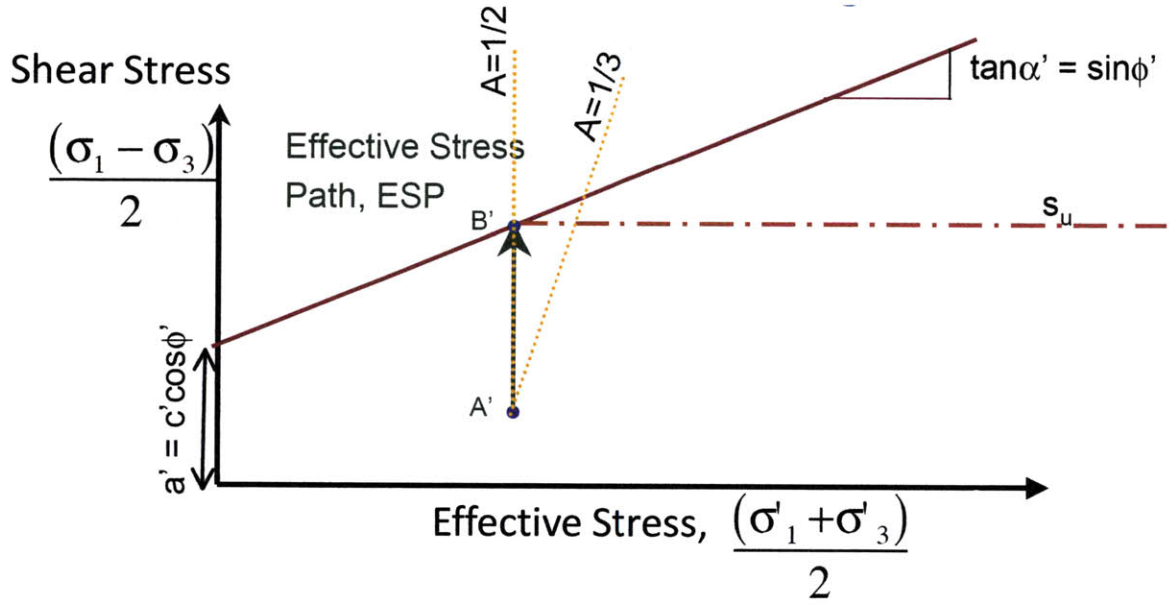

Figure 4-4: Effective stress path for undrained plane strain shearing using EPP (Mohr-Coulomb) soil model

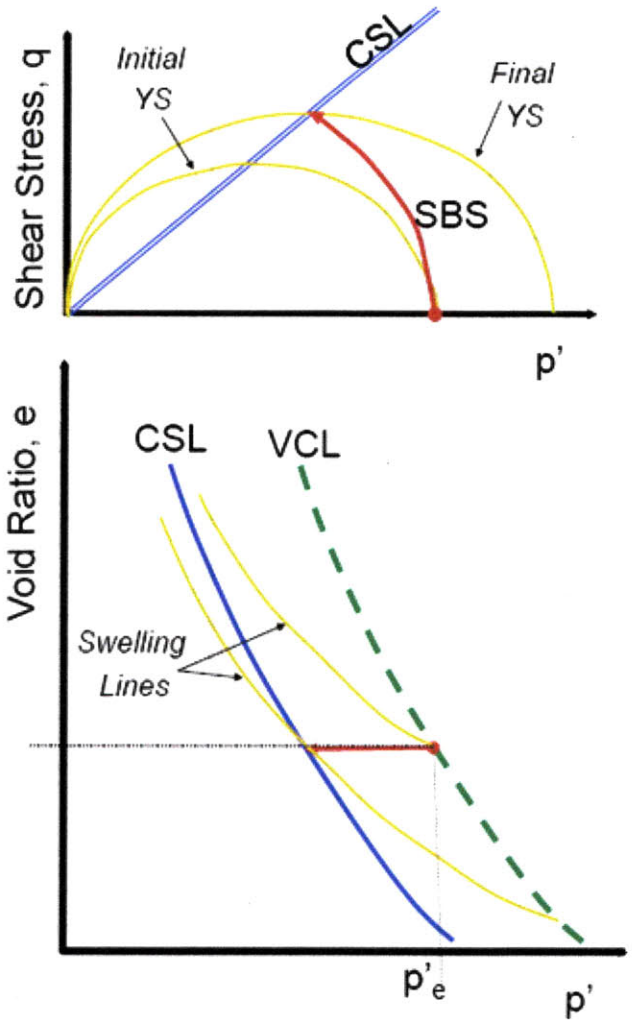

Figure 4-5: CSSM (Critical State Soil Mechanics) and MCC (Modified Cam Clay)

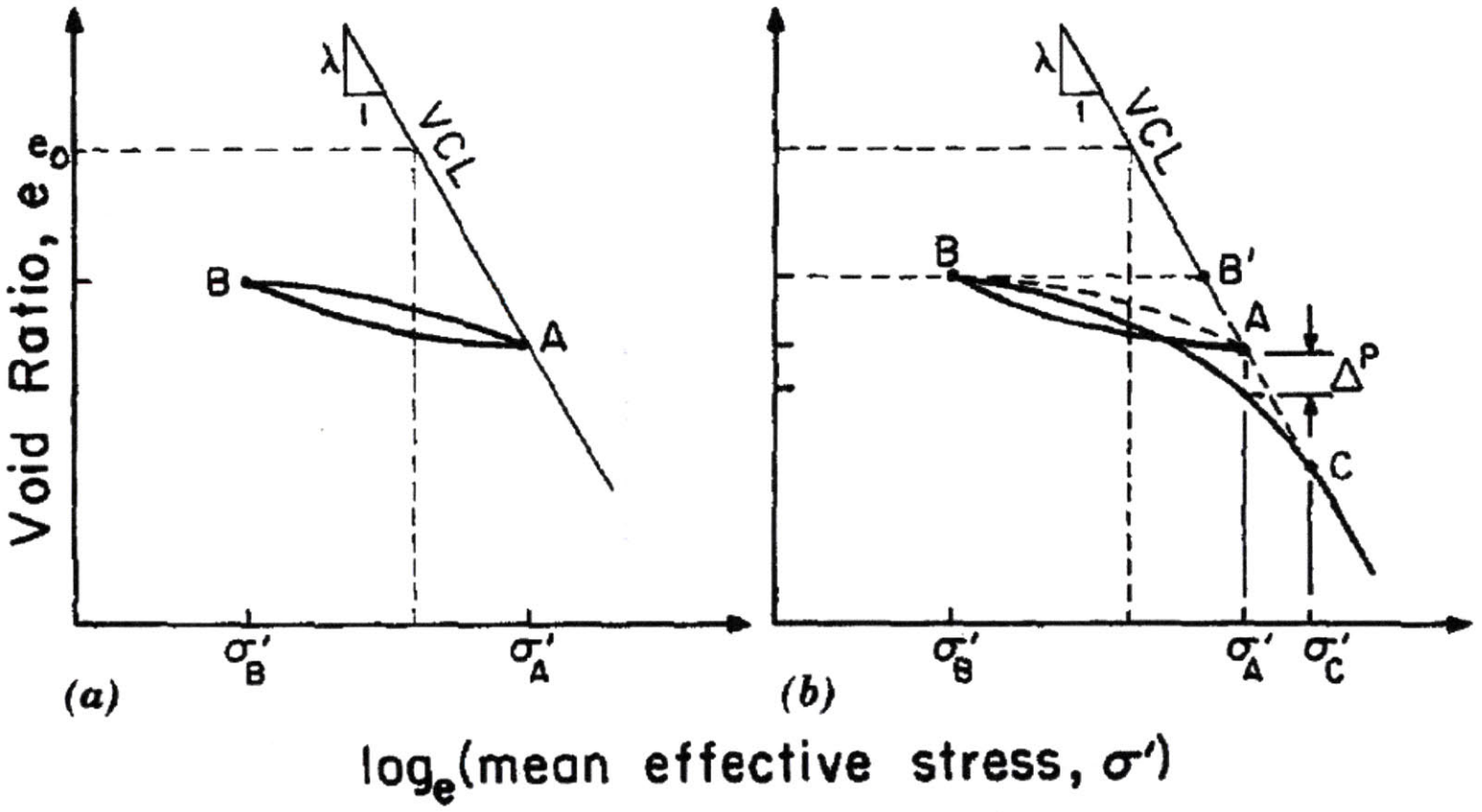

Figure 4-6: Conceptual model of Unload-Reload used by MIT-E3 for Hydrostatic Compression: (a) Perfect Hysteresis, (b) Hysteresis & bounding Surface Plasticity (Whittle & Kavvadas, 1994)

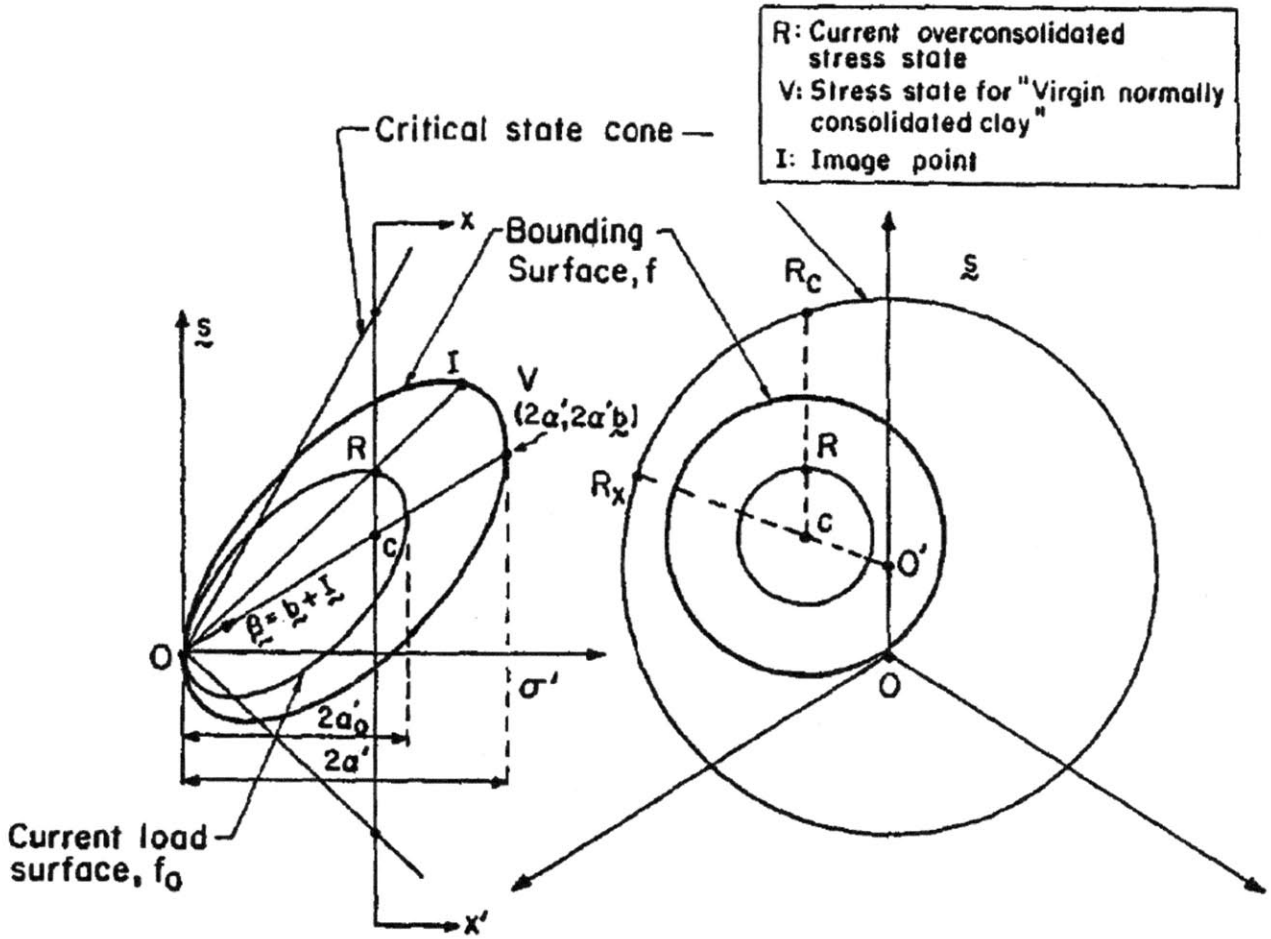

Figure 4-7: Yield, Failure & Load Surfaces used in MIT-E3 Model (Whittle & Kavvadas, 1994)

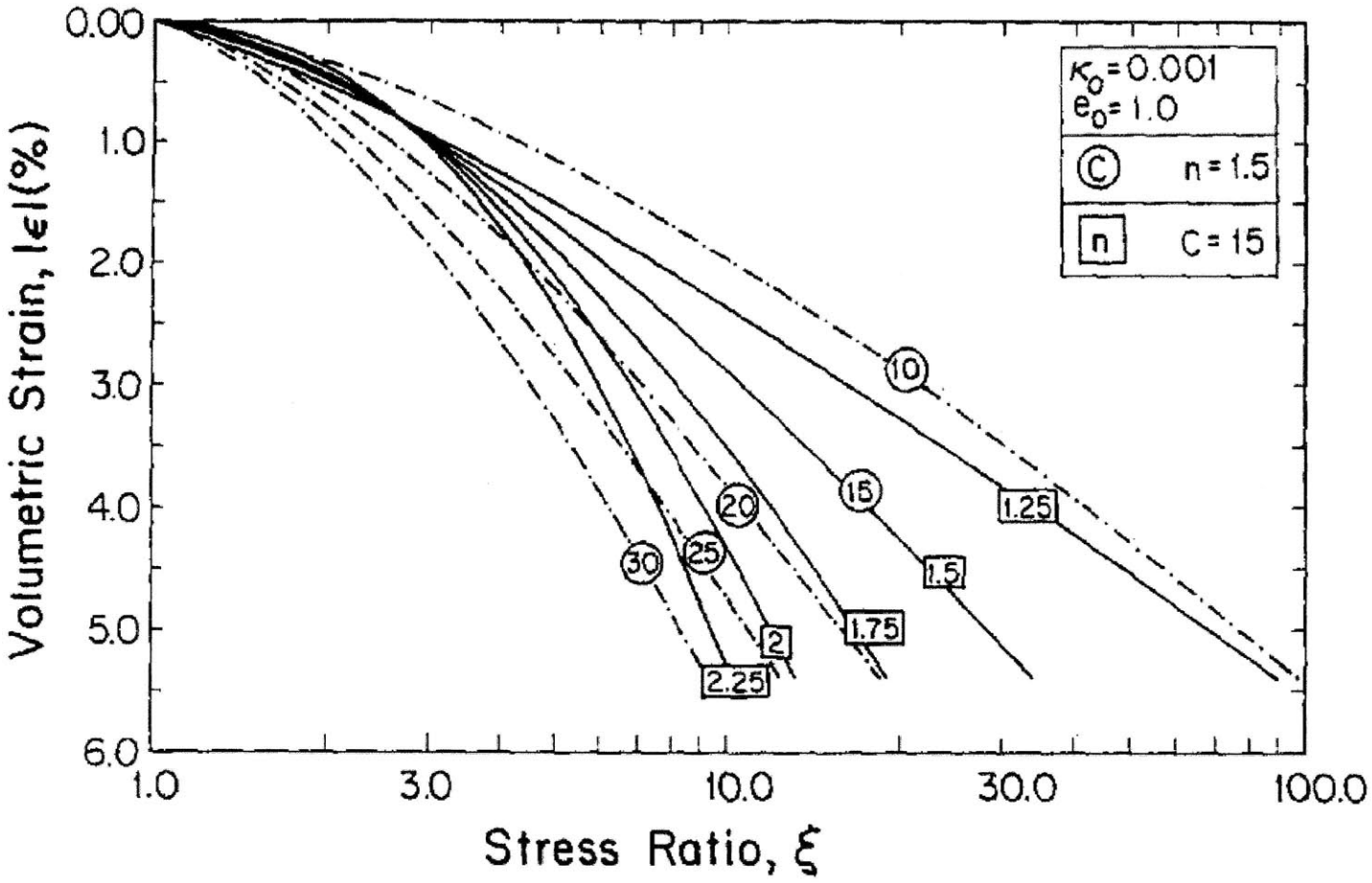

Figure 4-8: Evaluation of Model Input Parameters C, n for Hydrostatic Swelling (Whittle & Kavvadas, 1994)

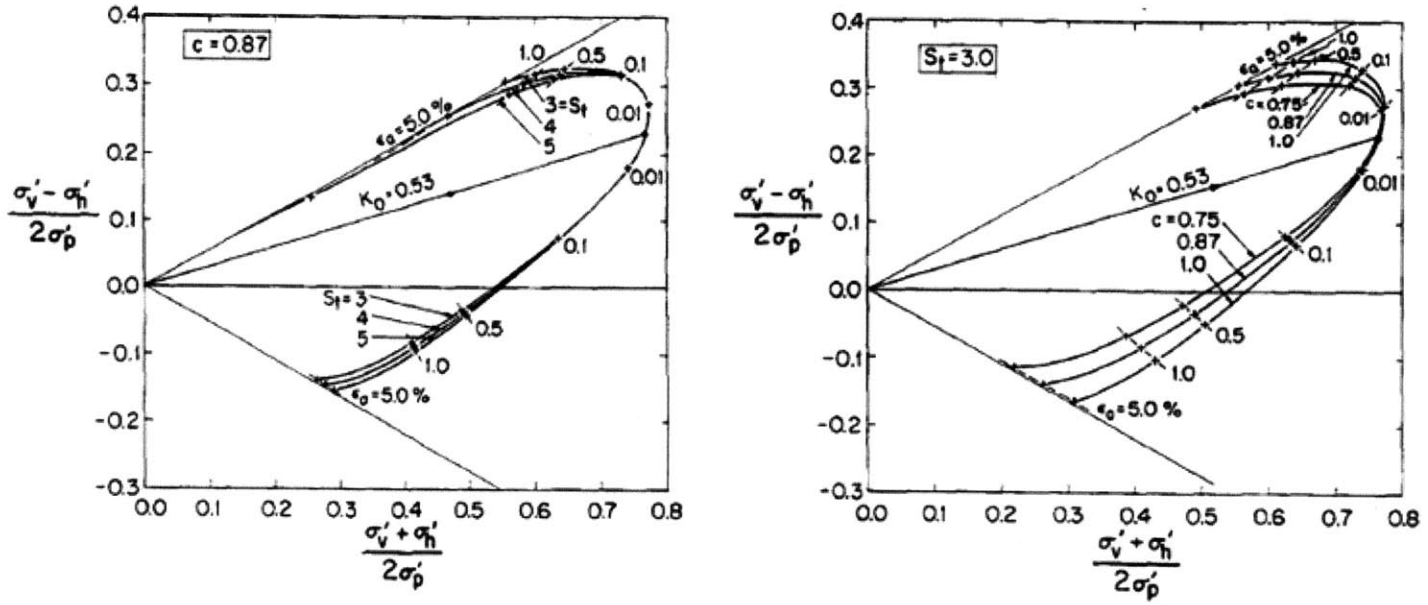

Figure 4-9: **Effect of Model Parameters St and c on Prediction of Effective Stress Paths for K_0-Normally Consolidated Clay in Undrained Triaxial Compression and Extension Tests (Whittle & Kavvadas, 1994)**

Table 4-1: Input Parameters for MIT-E3 Constitutive Soil Model: Upper Marine Clay (UMC) and Lower Marine Clay (LMC)

Test Type	Parameter/ Symbol	Physical contribution/meaning	Upper Marine Clay (UMC)	Lower Marine Clay (LMC)
1-D Consolidation (Oedometer. CRS.etc.)	e_o	Void ratio at reference stress on virgin consolidation line	1.80	1.60
	λ	Compressibility of virgin normally consolidated clay	0.380	0.370
	C	Non-linear volumetric swelling behavior	10.0	9.0
	n		1.50	1.50
	h	Irrecoverable plastic strain	0.2	0.2
Ko-Oedometer or Ko-Triaxial	K_{0NC}	K_0 for virgin normally consolidated clay	0.52	0.52
	2G/K	Ratio of elastic shear to bulk modulus (Poisson`s ratio for initial unload)	0.94	0.94
Undrained Triaxial Shear Tests: OCR=1: CKoUC OCR=1: CKoUE OCR=2. CKoUC	$\phi`_{TC}$	Critical state friction angles in triaxial compression and extension (large strain failure criterion)	32.4°	27.0°
	$\phi`_{TE}$		33.8°	27.1°
	c	Undrained shear strength (geometry of bounding surface)	0.96	0.96
	S_t	Amount of post-peak strain softening undrained triaxial compression	3.0	5.0
	ω	Non-linearity at small strains in undrained shear	0.40	0.40
	γ	Shear induced pore pressure for OC clay	0.5	0.5
Shear wave velocity	κ_0	Small strain compressibility at load reversal	0.0094	0.0094
Drained Triaxial	ψ_0	Rate of evolution of anisotropy (rotation of bounding surface)	100.0	100.0

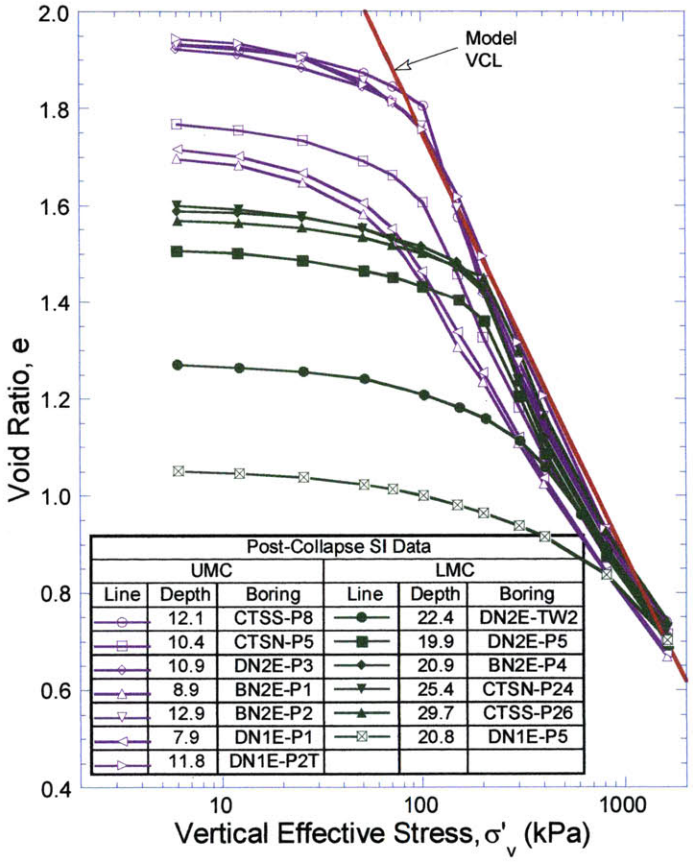

a) Compression behavior

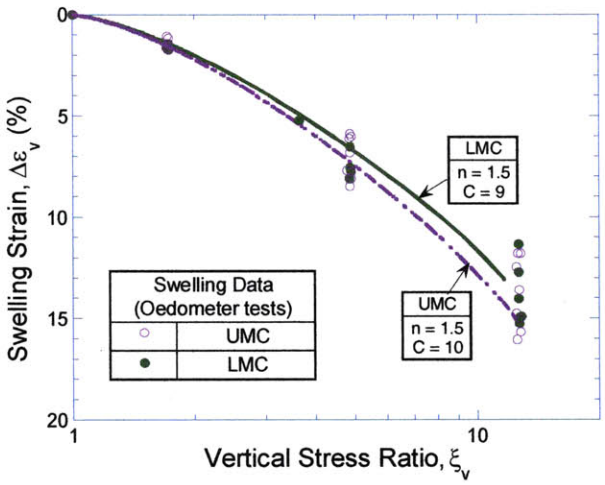

b) Swelling behavior

Figure 4-10: Compression and swelling properties of the Upper and Lower Marine Clays

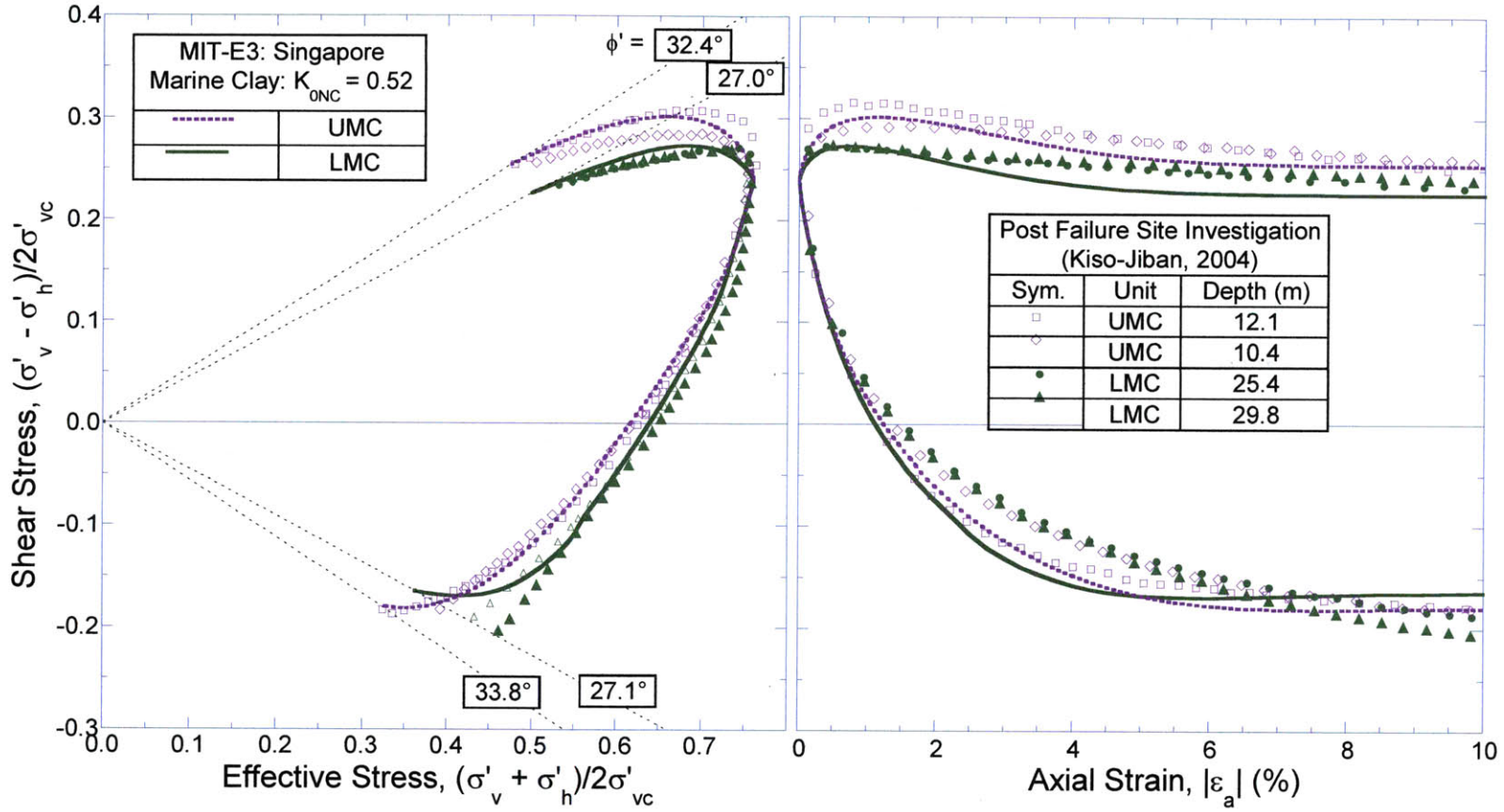

a) Effective Stress Paths

b) Shear strain-stress behavior

Figure 4-11: Comparison of measured undrained shear behavior from laboratory CAU compression and extension tests on normally consolidated UMC and LMC specimens with numerical simulations using the MIT-E3 model

Table 4-2: MC Model Parameters for Soil Layers used in Current Analyses (S335 Section)

Layer	Reference Elevation RL, m	Su [c'] (kPa)	† Δsu/Δz (kPa/m)	ϕ' (°)	E' (kPa)	† E'/Δz (kPa/m)	ν'	Ko
Fill	-	[0]	-	30	10000	-	0.25	0.5
Upper MC	98.2	20	0.397	0	6913	137	0.25	0.52
F2 Clay	-	88	-	0	29250	-	0.25	0.7
Lower MC	83.4	31	0.79	0	10310	346	0.25	0.52
F2-2 Clay	-	88	-	0	29250	-	0.25	0.7
F1-Sand	-	[0]	-	30	10000	-	0.25	0.5
OA-weathered	61.6	100	52	0	33250	13600	0.25	1
OA-competent	-	500	-	0	167500	-	0.25	1
JGP	-	300	-	0	250000	-	0.15	-

† Linear variations with depth in stiffness and shear strength within soil layers starting at reference elevation (constant values above)

5 FINITE ELEMENT MODELING

5.1. Model Geometry

The cross-sectional geometry at S335 has been developed using data from the original site investigation and the post-collapse investigation.

Figure 5-1a and 5-1b show the detailed soil profiles along the north and south walls in the M3 design area. Figure 5-2 shows the location of all boreholes available at the site. The figure locates boreholes that have been used to develop the cross-section for analysis at S335 from COI (2005). These figures highlight important changes in stratigraphy and differences in elevations at the two walls. Figure 5-2 summarizes the cross-section for S335 considered in this thesis. The results show much more refined stratigraphy (than the original one; Figure 2-7) especially the subdivision of units below the Lower Marine Clay (LMC). The design section comprises mainly low permeability clay units. However, there is a lens of higher permeability sand, F1 that intrudes across the north wall. Arup (2005) have mapped this unit very carefully, Figure 5-3, and found that it is discontinuous and therefore does not act as a source of hydraulic recharge.

The original design for M3 was based on one borehole, ABH32 and assumed a symmetric section for design of the excavation support system (Figure 2-7). The current profile is strongly asymmetric with larger changes in elevation at the base of the marine clay associated with the valley in Old Alluvium. This profile also introduces sub-units of the Kallang formation including Upper Estuarine and Lower Estuarine.

The current analysis of S335 uses the as-built data on toe embedments assumed in the M3 design sector.

Following Whittle and Davies (2006), the current analyses assume that the Upper Estuarine and Lower Estuarine clays have the same engineering properties as the UMC and LMC units, respectively. The FE model for S335 section, Figure 5-3, extends from the excavation to minimize effects of lateral boundaries on the excavation performance. The lateral earth support design includes two layers of continuous jet grout pile (JGP) rafts that were intended to provide additional passive resistance below the formation. At section S335 it is unlikely that the lower JGP raft is continuous within the Old Alluvium, as installation jetting parameters for the jet grout columns were based on parameters calibrated to marine clay conditions. Hence, the section shows a truncation of the lower JGP raft at the North wall.

5.2. Soil Layer, Diaphragm Wall & Strut Properties

Table 5-1 summarizes the MC model parameters used to present the soil and JGP layers at S335 based on values determined by Whittle and Davies (2006)†. It should be noted that the analyses account for linear changes in the elastic stiffness (E', ΔE') and shear strength (c', Δc') of the key UMC, LMC and OA layers using a reference elevation (see Table 5-2). The Fill is treated as a drained material while other layers remain undrained through the course of the excavation.

Table 5-2a shows the elevations assumed for the upper and lower JGP layers.

† K_0 values for the UMC and LMC layers are both considered to be equal to 0.52 (instead of 0.7 as used by Whittle and Davies, 2006).

Tables 5-2b and 5-2c summarize the properties of the reinforced diaphragm wall panels† and Table 5-3 the cross-lot bracing. The later presented in terms of axial stiffness and capacity per unit width of excavation. The compression capacity of strut is based on the capacity of the strut-waler connections as reported by Bell and Chiew (2006). The first 6 levels of strutting use plate stiffnesses. These remain ductile when overloaded and hence are well modeled by elasto-plastic elements in Plaxis^{TM}. Brittle strut-waler connections were installed at levels 7-9 (using C-channel stiffness). The current analyses do not model loss of strut capacity directly, but are able to simulate collapse if the 9th level strut becomes overloaded, buy assuming full loss of capacity (as done by other experts in COI, 2005).

The initial conditions in the FE model include considerations of initial pore pressures associated with underconsolidation and deviations from K_0-conditions due to inclinations of the soil strata.

In order to represent 1-D flow condition and simulate the groundwater flow conditions observed in the field, different constant head values were assigned at different depths. Figure 5-6 shows the piezometric head profile assumed in the FE model.

The initial effective stress conditions are obtained by relaxing pre-defined K_0-conditions to bring stresses in the inclined layers into an initial drained equilibrium.

The current analyses assume $\sigma'_p/\sigma'_{v0} = 1.0$ in both UMC and LMC units (Fig. 5-7a). When combined with the assumed pore pressure conditions, this implies that the marine clays are

† The wall sections had three different arrangements of reinforcements and hence are each sub-divided into top, middle and lower section.

slightly under-consolidated. The in-situ stresses also deviate from K_0-conditions due to the inclined stratigraphy. This is modeled using a standard drained relaxation of stress procedure within Plaxis.

Figure 5-7b summarizes the anisotropic undrained shear strength profiles† within the marine clays obtained using the MIT-E3 model for three standard modes of plane strain shearing. The undrained plane strain active and passive strengths bound the best estimate profile recommended by Whittle and Davies (2006), based on their interpretation of piezocone tests (this assumes $s_{uDSS}/\sigma'_{v0} = 0.21$ for normally consolidated Singapore marine clay, after Tan et al., 2003). It is interesting to note that the undrained shear strength predicted by MIT-E3 in the DSS mode is 5-7kPa lower than the best estimate used in the prior MC analyses within the LMC. The figure compares the profiles obtained using the MC model (with parameter listed in Table 5-1) with results obtained when MIT-E3 model is used to represent the UMC and LMC units (and Estuarine layers). The following points should be noted:

1. The MC model generally describes higher strengths in the Upper Marine Clay than MIT-E3, but is closer to the average of the anisotropic strength in the Lower Marine Clay.
2. The MIT-E3 model predicts very similar shear strengths in the simple shear and passive (extension) modes in both UMC and LMC units.

Table 5-4 summarizes the steps used to simulate the construction sequence at S335.

† corresponding to a south section behind the south wall.

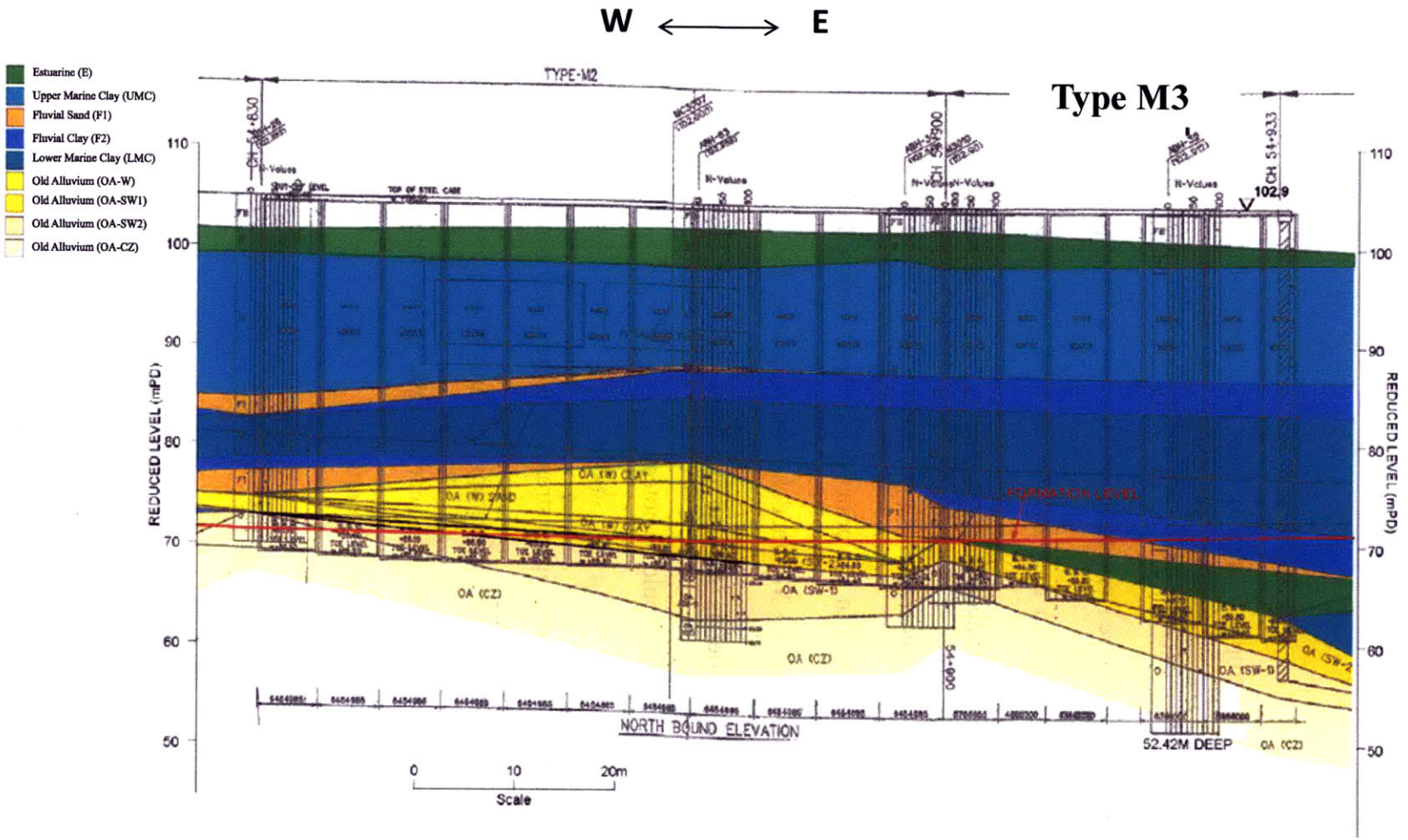

Figure 5-1a: North Wall Section Stratigraphy at M3 area (COI, 2005).

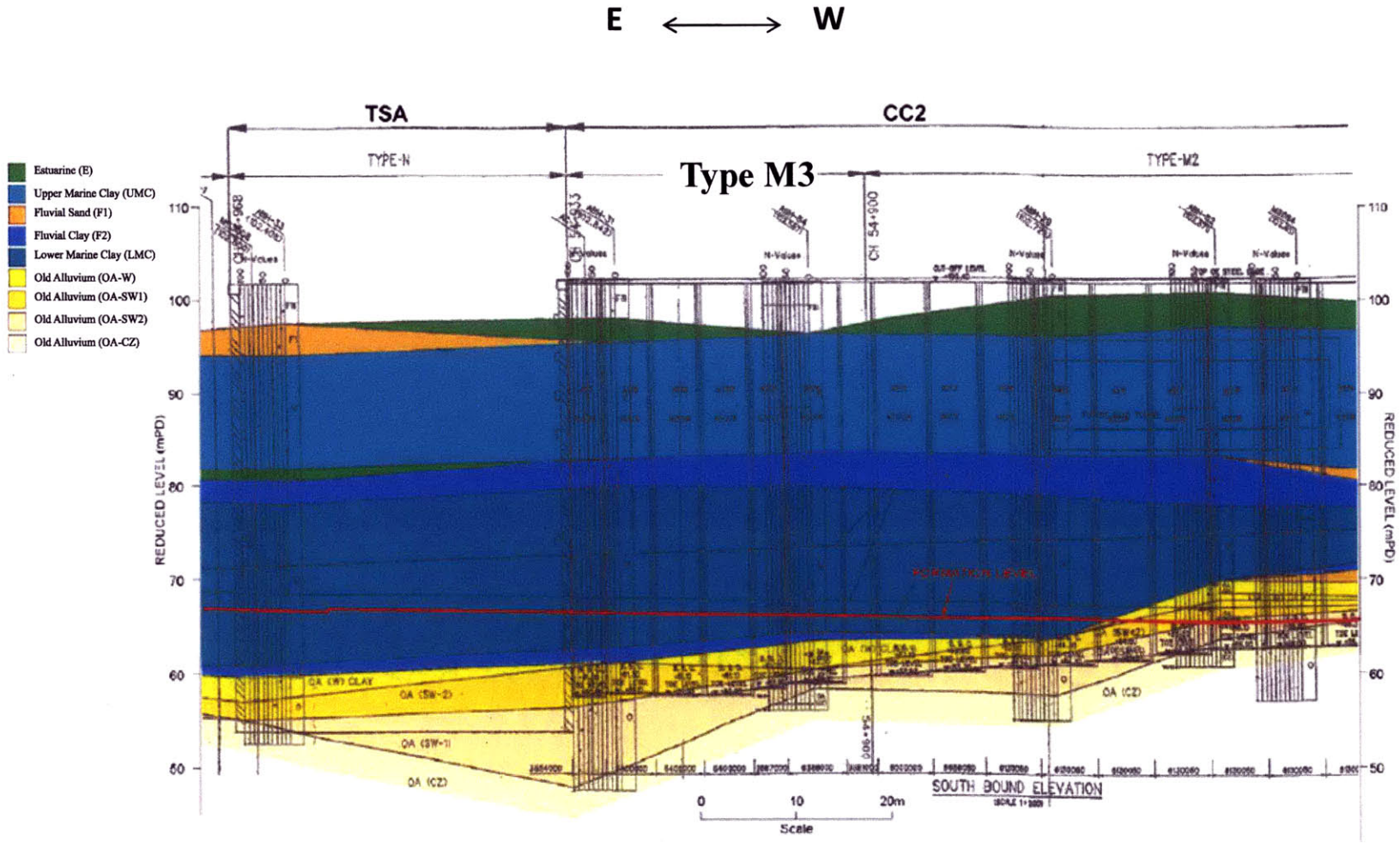

Figure 5-1b: South Wall Section Stratigraphy at M3 area (COI, 2005).

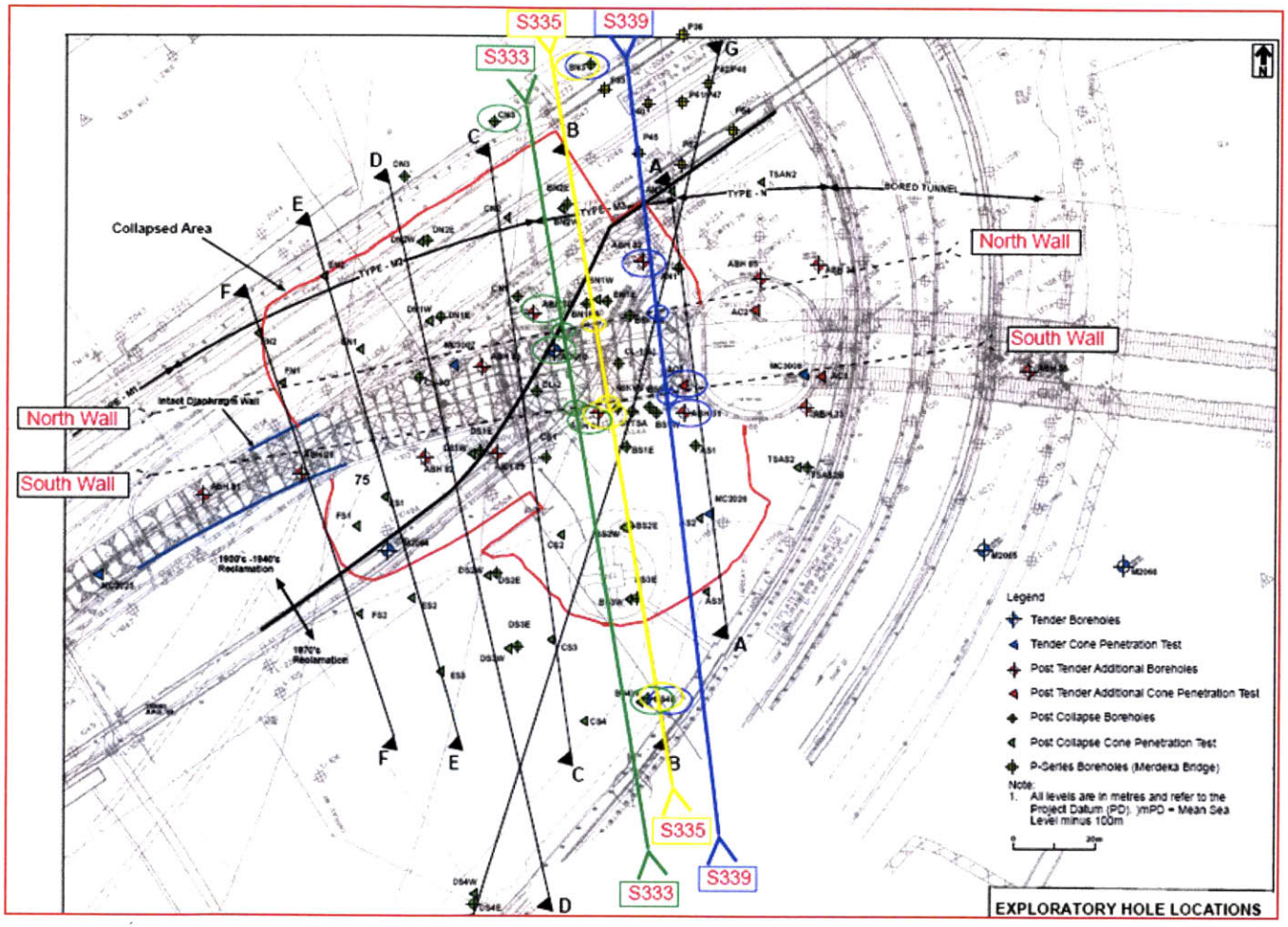

Figure 5-1: Post Collapse Site Exploration for S333, S335 & S339 Sections showing Boreholes (Arup 2005).

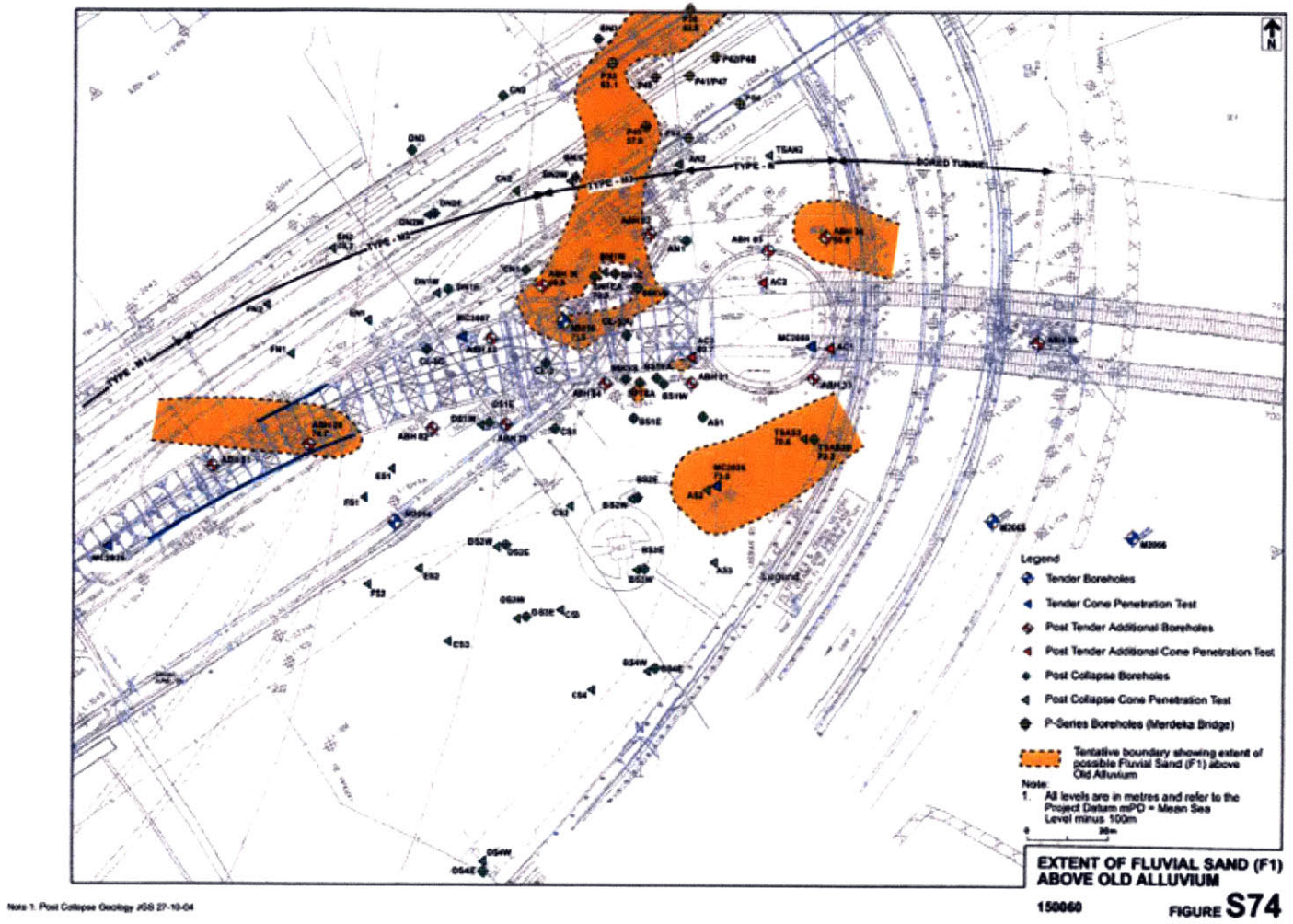

Figure 5-2: Extension of the F1 Fluvial Sand at the M3 Type Area (Arup, 2005).

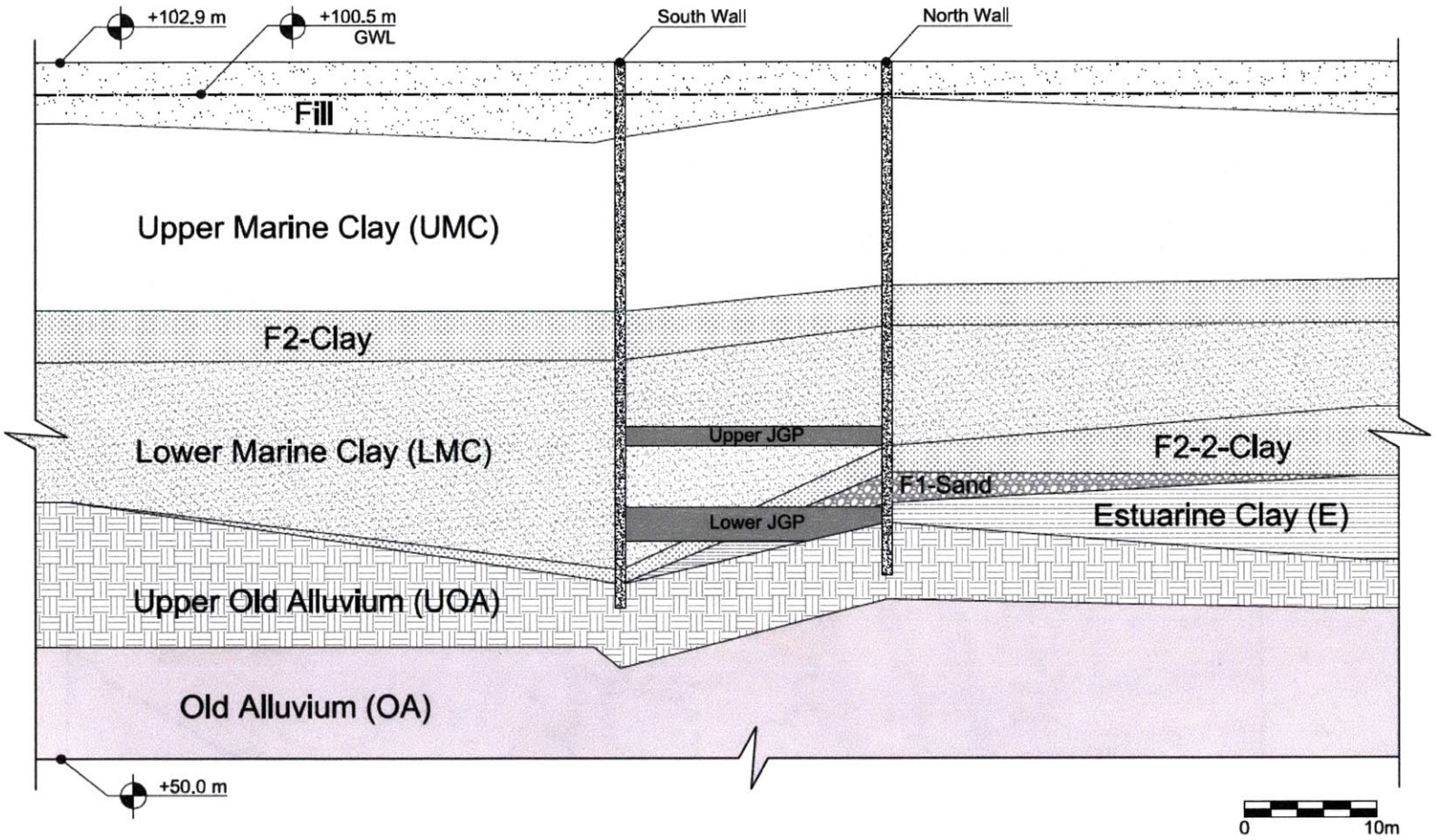

Figure 5-3: S335 Section geometry used in FE model (Corral and Whittle, 2010).

Table 5-1: MC Model parameters for soil layers at S335 model.

						Strength Parameters				Elastic Properties			
ID	**Layer**	Material Type	Reference Elevation RL, m	$k_x=k_y$ (m/day)	γ_t (kN/m3)	s_u [c'] (kPa)	† $\Delta s_u/\Delta z$ (kPa/m)	ϕ' (°)	ψ' (°)	E' (kPa)	† E'/Δz (kPa/m)	ν'	K_{ONC}
1	Fill	drained	-	8.64E-02	19.0	[0]	-	30	0	10000	-	0.25	0.5
2	Upper MC	undrained	98.2	8.64E-05	16.0	20	0.397	0	0	6913	137	0.25	0.52
3	F2 Clay	undrained	-	8.64E-05	19.0	88	-	0	0	29250	-	0.25	0.7
4	Lower MC	undrained	83.4	8.64E-05	16.8	31	0.79	0	0	10310	346	0.25	0.52
5	F2-2 Clay	undrained	-	8.64E-05	20.0	88	-	0	0	29250	-	0.25	0.7
6	F1-Sand	undrained	-	8.64E-05	19.0	[0]	-	30	0	10000	-	0.25	0.5
7	OA-weathered	undrained	61.6	8.64E-04	20.0	100	52	0	0	33250	13600	0.25	1
8	OA-competent	undrained	-	8.64E-05	20.0	500	-	0	0	167500	-	0.25	1
9	JGP	undrained	-	8.64E-05	16.0	300	-	0	0	250000	-	0.15	-

† Linear variations with depth in stiffness and shear strength within soil layers starting at reference elevation (constant values above)

Table 5-2: (a) JGP Raft Elevations, (b) Elevations of Type Walls, and (c) Wall Material Properties (COI, 2005 and Arup, 2005).

JGPs		
Elevations		Thickness
Top of Upper	75.3 m	1.5 m
Bottom of Upper	73.8 m	
Top of Lower	69.2 m	2.6 m
Bottom of Lower	66.6 m	

(a)

Type Wall Elevations	
Upper	102.9-85.0
Middle	85.0-71.0
Lower	71.0-61.5 (south) 71.0-64.0 (north)

(b)

ID	Name	Type	EA [kN/m]	EI [kNm^2/m]	w [kN/m^2]	ν	Mp [kNm/m]	Np [kN/m]
1	(Lower)	Plastic	16000000	597000	6.4	0.15	2300	1.00E+15
2	(Middle)	Plastic	16000000	597000	6.4	0.15	3500	1.00E+15
3	Upper	Plastic	16000000	597000	6.4	0.15	2500	1.00E+15

(c)

Table 5-3: Strut Properties & Pre-Load Struts Assumed, and Elevation (Reduced Level) for each Strut Level (Arup, 2005)

ID Strut	Name	EA [kN/m]	|F_max,comp| [kN/m]	|F_max,tens| [kN/m]	Pre-Load [kN/m]	Elevation, RL [m]
1	Level1	903000	825	0	200	101.9
2	Level2	1148000	825	0	363	99.2
3	Level 3	2295000	1950	0	630	95.6
4	Level 4	2295000	1950	0	500	92.1
5	Level 5	2295000	1950	0	525	88.6
6	Level 6	1551000	1200	0	265	85.6
7	Level 7	2295000	1750	0	605	82.6
8	Level 8	3104000	2300	0	400	79.3
9	Level 9	2295000	1750	0	250	76.3

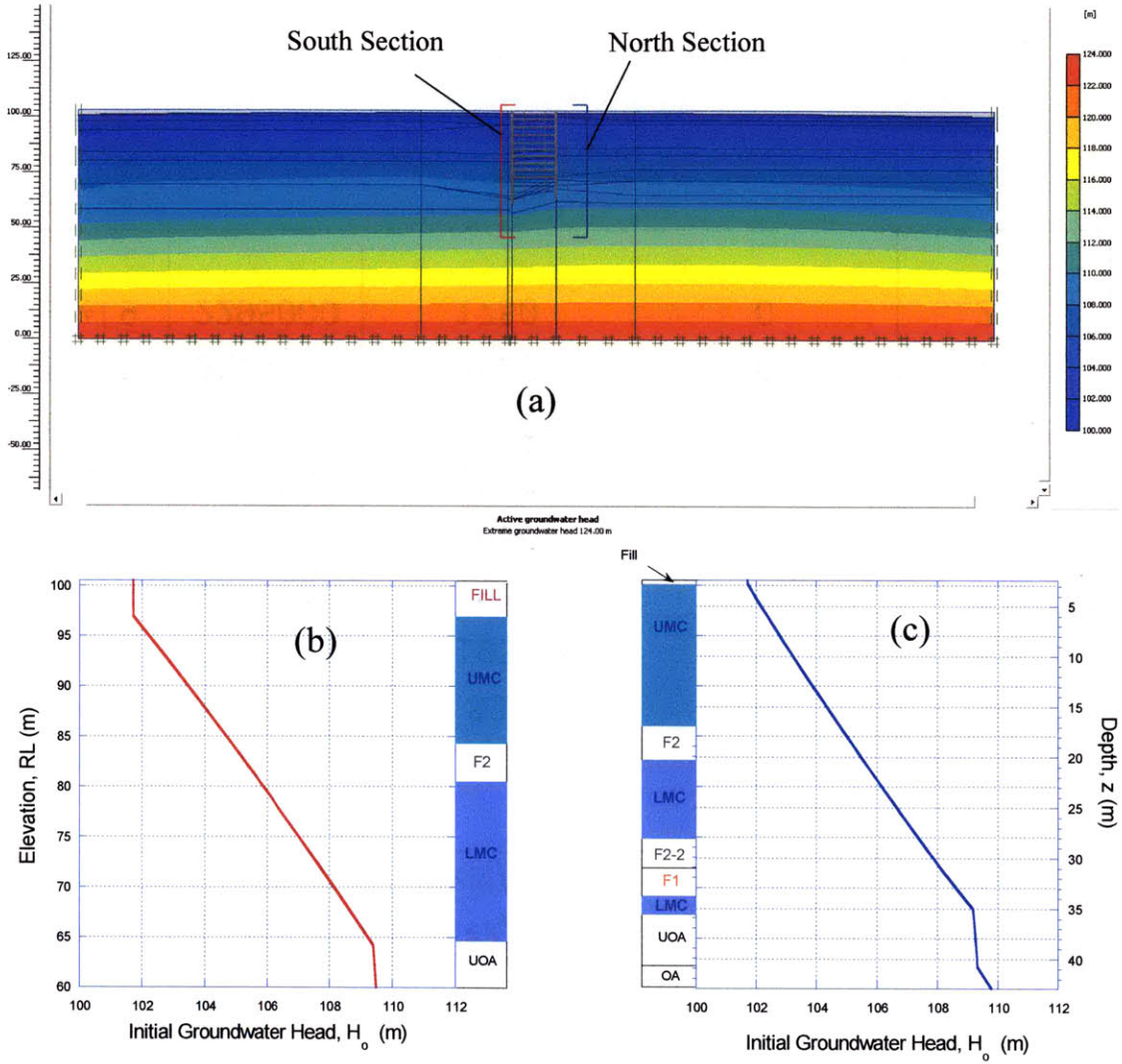

Figure 5-4: (a) Ground Water Heads for Initial Conditions, after Appling Initial Drained Equilibrium: (b) South Section and (c) North Section

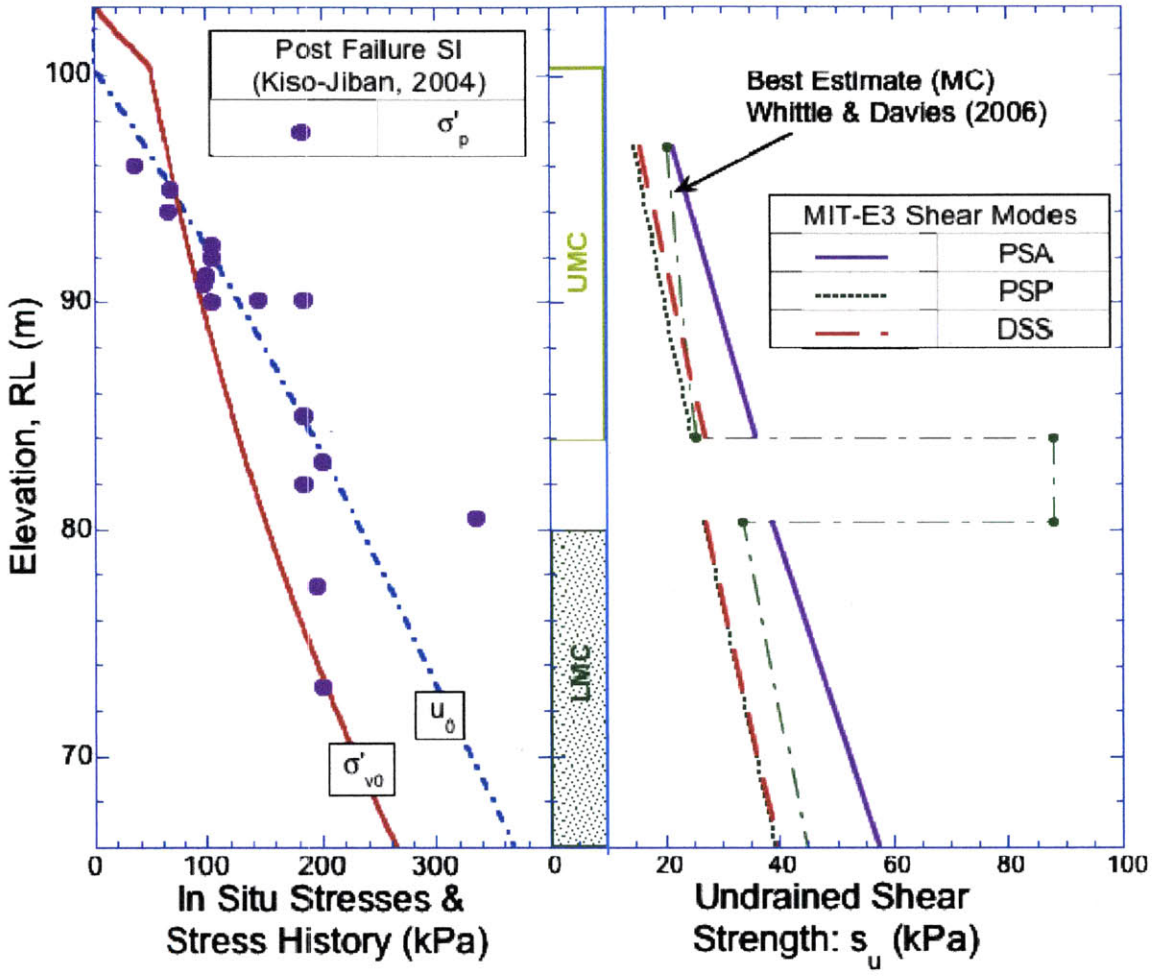

Figure 5-5: **Comparison of in situ stresses and undrained strengths of marine clay used in FE model (Corral & Whittle, 2010)**

Table 5-4: Calculation Phases used in FE simulations for S335 Section.

1. Initial Drained Equilibrium (since there are no horizontal soil layers)
2. Diaphragm Wall Installation
3. JGP raft Installations
4. Surcharge Application of 10 kPa (outside the excavation & applied at the top of the Fill)
5. Excavation Level 1 – Elevation, RL, 100.9 m
6. Strut Level 1 - Elevation, RL, 101.9 m
7. Excavation Level 2 – Elevation, RL, 98.2 m
8. Strut Level 2 - Elevation, RL, 99.2 m
9. Excavation Level 3 – Elevation, RL, 94.6 m
10. Strut Level 3 - Elevation, RL, 95.6 m
11. Excavation Level 4 – Elevation, RL, 91.1 m
12. Strut Level 4 - Elevation, RL, 92.1 m
13. Excavation Level 5 – Elevation, RL, 87.6 m
14. Strut Level 5 - Elevation, RL, 88.6 m
15. Excavation Level 6 – Elevation, RL, 84.6 m
16. Strut Level 6 - Elevation, RL, 85.6 m
17. Excavation Level 7 – Elevation, RL, 81.6 m
18. Strut Level 7 - Elevation, RL, 82.6 m
19. Excavation Level 8 – Elevation, RL, 78.3 m
20. Strut Level 8 - Elevation, RL, 79.3 m
21. Excavation Level 9 – Elevation, RL, 75.3 m
22. Strut Level 9 - Elevation, RL, 76.3 m
23. Excavation Level 10 – Elevation, RL, 72.3 m
24. Strut Level 10 - Elevation, RL, 73.3 m

6 RESULTS OF NUMERICAL SIMULATIONS FOR S335 SECTION

6.1. Computed Lateral Wall Deflections

This Chapter considers the role of the soil model on predictions of excavation performance and predictive accuracy.

Figures 6-1a and 6-1b summarize predictions of lateral wall deflections at different stages of the excavation for the South and North walls at S335. The results compare results for the MC profile with the 'MIT-E3' profile where UMC and LMC layers are represented using the MIT-E3 model. The main points are as follows:

1. Both sets of analyses show similar modes of wall deformation. For the South wall, there is a monotonic increase in maximum inward wall deflection as the excavation depth increases. The maximum wall deflection occurs slightly below the formation level at a given excavation stage. In contrast, the North wall deforms and reaches a maximum inward deformation when the excavation reaches El. 81.6 mRL (Level 7). For subsequent excavation there is a reversal and the wall moves back to slightly into the retained soil.
2. The MIT-E3 profile generally predicts higher inward wall movements for both South and North walls than the base case MC analyses. This result is influenced significantly by the large initial cantilever movements occurring in the first (unsupported) phase of excavation. This result reflects the very low strength at the top of the UMC unit (Figure 5-6). This condition occurs due to the assumption that OCR=1.0 throughout the marine

clay. Once struts are installed, movements of top of the wall are heavily constrained. The MIT-E3 profile shows inward movements of approximately 50 mm at the top of the North wall and 10 mm at the top of the South wall. In comparison the MC profile generates wall outward movements at the top of built North and South walls.

3. Inward movements predicted at the South wall reach a maximum movement exceeding 420 mm for MIT-E3 vs. 350 mm for the MC profile (for excavations to level 10, including the removal of the upper JGP layer). In contract, the maximum inward movement of the North wall is 195 mm and 150 mm for the MIT-E3 and MC profiles, respectively, at stage 7 (El. 81.6 mRL).

Figure 6-1 compares the computed maximum wall deflections of the two analyses. These results confirm the close qualitative agreement for the two profiles. Additionally, Table 6-1 and Figure 6-2 summarize the maximum computed lateral wall deflections with their corresponding elevations at each excavation stage.

6.2. Comparison of Computed and Measured Wall Deflection

Figure 6-3, 6-4 and 6-5 compare predictions of lateral wall deflections from the current analyses with measured data from the two inclinometers (I-104, I-65) and with results of prior analyses (marked as MC) performed by Whittle & Davies (2006). The results are shown at six times during the two months preceding the collapse (with excavation depths 15.3, 18.3, 21.3, 24.6, 27.6 and 30.6 m). Figure 6-3 shows predictions for level 5 and 6 excavations (El. 87.6 and El. 84.6m), while those related to level 7 and 8 excavations (El. 81.6 and El. 78.3 mRL), and level 9 and 10 excavations are shown in Figures 6-4 and 6-5, respectively. The current analyses predict

very well the maximum lateral wall deflection on the south side of the excavation including the large deflections associated with removal of the upper JGP layer (April 17-20). At this stage, a plastic hinge formed in the South wall (at a depth of 32m) and there is very large rotation of the toe. The current analyses also describe very well the maximum lateral wall deflection on the north side through March. The analyses tend to overestimate inward movements of both walls within the upper 10-15m of the bracing system. This may be attributed to the assumption that the UMC is normally consolidated, while the pre-consolidation data show a small OCR in this layer (Figure 5-6). The analysis predicts significant lateral displacements at the toe of the north wall in April 2004 (70mm at time of failure on April 17-20). In contrast, inclinometer I-65 suggests that the north diaphragm wall panel remains well anchored (see Figure 6-5). The net effect is that the analysis underestimates the deflections and flexure in the lower part of the north wall during April. This result is largely related to the complex stratigraphy and assumed truncation of the lower JGP at the north wall. Table 6-2 summarizes both the computed and measured maximum wall deflections for each level excavation previously mentioned and for each side (i.e. south wall and north wall). The same information is graphically represented in Figure 6-6.

The current analyses using MIT-E3 predict larger inward wall deflections than the prior MC analyses and are in rather better agreement with the measured data. This result is encouraging as the current analyses are based on calibration of a complex constitutive model using laboratory test data (rather than a best estimate of a design strength line). However, it is clear that certain features of the measured data such as the toe fixity on the north wall are difficult to interpret and

are not controlled by the properties of the marine clay. Similarly, the current analyses do require additional judgment in the selection of the OCR profile.

6.3. Computed Bending Moments in Diaphragm Wall

Figures 6-7a and 6-7b compare computed bending moments for the MC and MIT-E3 profiles in the South and North walls, respectively. The results show relatively small differences in computed moments for the two profiles. Results for the North wall show that the design reinforcement provides adequate capacity at all stages of the excavation. The analyses of the South wall show that the plastic moment capacity is exceeded at the El. 72.3 mRL, such that a plastic hinge is predicted after removal of the upper JGP (stage 10 excavation), as indicated Figure 6-7a. This marks the outset condition for the collapse mechanism. A summary of each stage of computed maximum bending moment magnitudes is presented in Table 6-3.

6.4. Computed and Measured Strut Loads

In this section, the MC and MIT-E3 strut load predictions are discussed. All strut level elevations correspond to 1 m above the excavation levels (e.g. for excavation at EL. 100.9 mRL, strut 1 is located at EL. 101.9 mRL).

Figures 6-8, 6-10, 6-12, and Figures 6-9, 6-11, 6-13 show the strut load distribution prediction for struts 1-9 for MC and MIT-E3 profiles, respectively. A summary of the computed maximum strut load at each level is shown in Table 6-4. Two models show similar details (small

differences in magnitude). The struts were assumed to behave as an elastic-perfectly plastic material.

Figure 6-14 compares the predicted maximum strut loads for each model profile with measured data. These predicted strut loads for MC and MIT-E3 profiles are consistent with ductile buckling observed in plate stiffeners at level 6 (COI, 2005). Strut loads at level 7 and 8 are in normal ranges for MC and MIT-E3.

Both sets of analyses predict that the capacity of the 9th level strut-waler connection is fully mobilized at this stage of excavation (30.6m deep) immediately following removal of the upper JGP raft. In contrast the measured strut loads are much smaller. This is an inconsistency noted by all the experts to the public inquiry (COI, 2005). Hence, it can be concluded that the current analyses with MIT-E3 are able to predict the onset of collapse consistent with prior MC analyses but do not shed any insight to explain the measured loads at level 9.

6.5. Vertical Settlements

Figure 6-15a and 6-15b compare both the computed surface settlement profiles to the south and north of S335 using the MC and MIT-E3. The profiles generate higher settlement for MIT-E3 than MC on both sides of the excavation. Results on the north side are highly influenced by the initial cantilever deflections produced in the first stage of excavation. Also, the reverse lateral wall deflection effect on the North wall is associated with the decrease of surface North vertical settlement after level 7 excavation (El. 81.6 mRL). Table 6-5 summarizes the predicted maximum magnitudes of vertical settlements for both profiles and both wall sides.

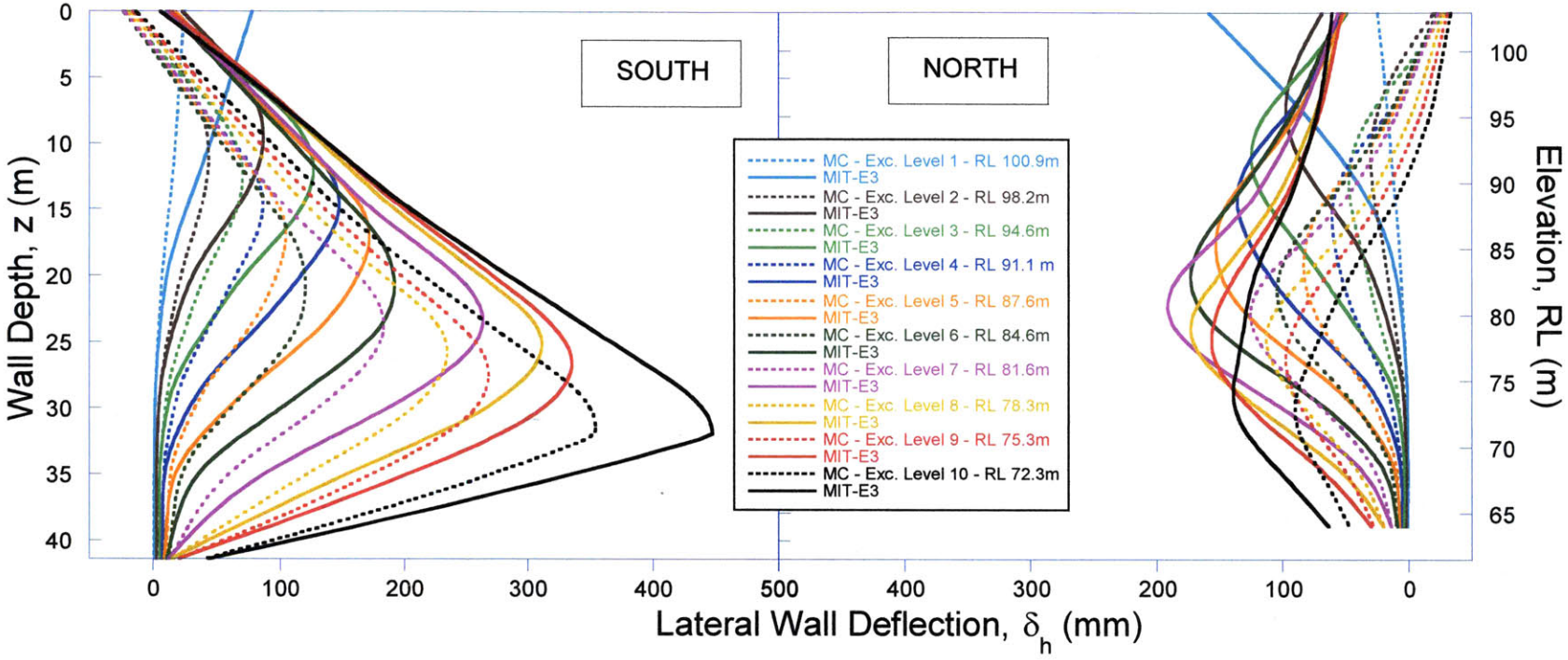

Figure 6-1: S335 Wall Deflection Comparison between MC and MIT-E3: (a) South Wall (b) North Wall

Table 6-1: Summary of Computed Maximum Lateral Wall Deflections & Corresponding Elevations

		Maximum Lateral Wall Deflections and corresponding Elevations							
After Excavation		South				North			
Level	EL. RL	MC	EL. (RL)	MIT-E3	EL.	MC	EL.	MIT-E3	EL.
#	(m)	(mm)	(m)	(mm)	(m)	(mm)	(m)	(mm)	(m)
1	100.9	25	102.9	78	102.9	25	102.9	159	102.9
2	98.2	44	91.9	87	93.4	30	91.9	98	95.6
3	94.6	71	90.5	127	91.1	47	89.9	125	92.1
4	91.1	86	88.4	148	88.4	61	87.2	136	88.6
5	87.6	105	86.1	172	85.6	83	83.8	153	85.4
6	84.6	120	81.9	192	82.1	105	81.9	173	82.7
7	81.6	183	79.3	263	79.6	126	79.9	191	80.5
8	78.3	235	77.3	311	77.8	113	78.3	173	79.1
9	75.3	268	75.6	335	76.3	98	76.8	157	78.3
10	72.3	354	71.3	447	71.0	90	72.8	139	74.2

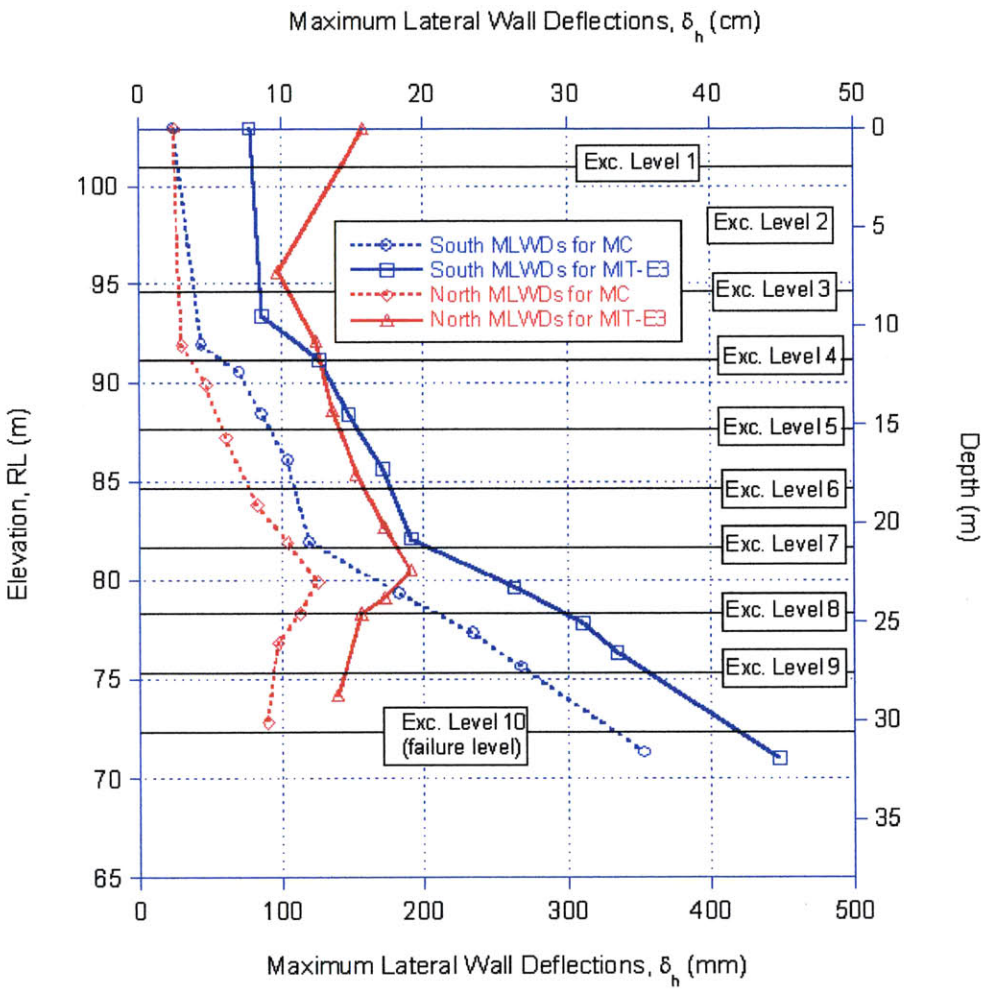

Figure 6-2: Maximum Lateral Wall Deflections vs. Elevations

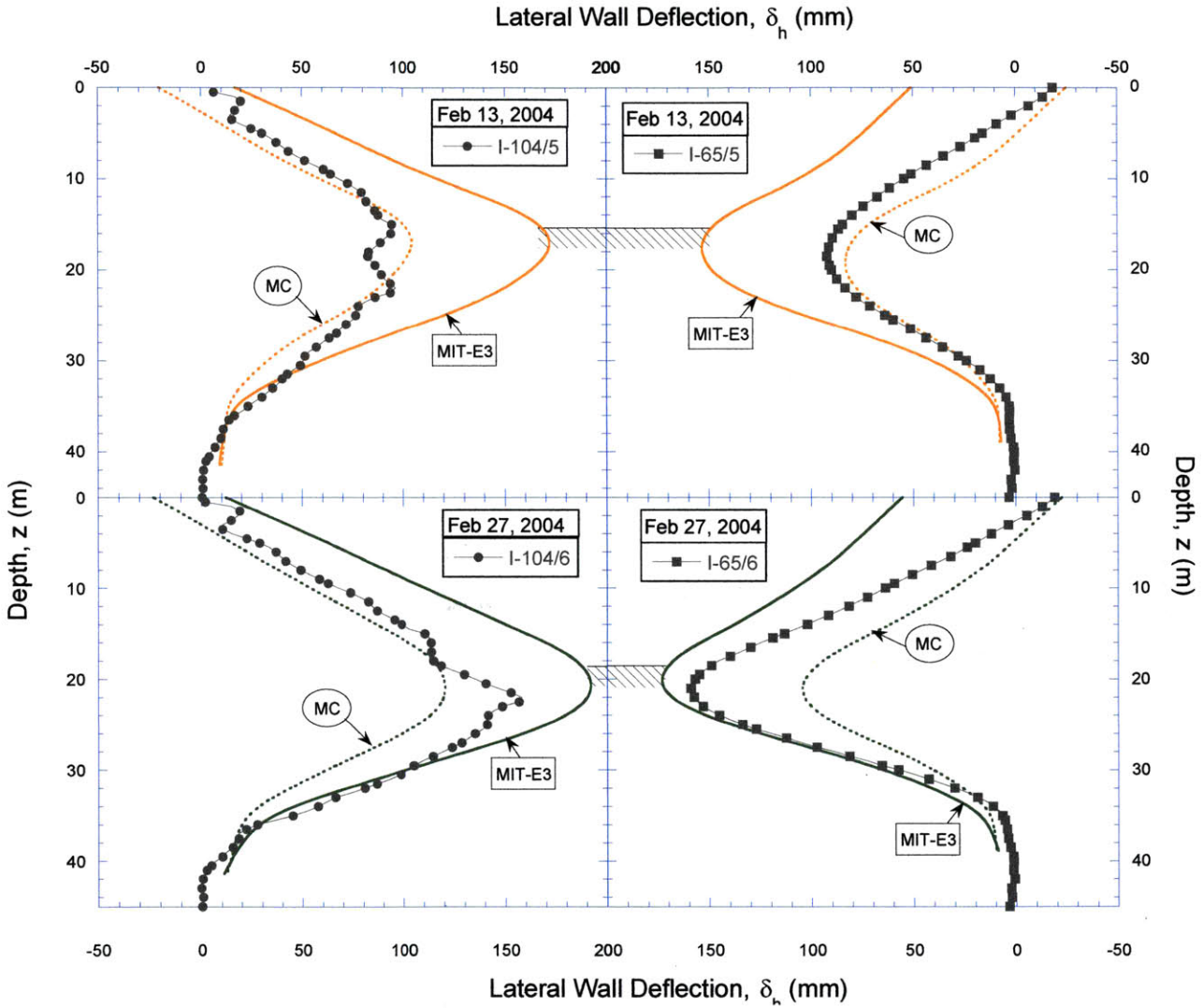

Figure 6-3: Measured and Predicted Wall Deflections for Excavation Levels 5 and 6

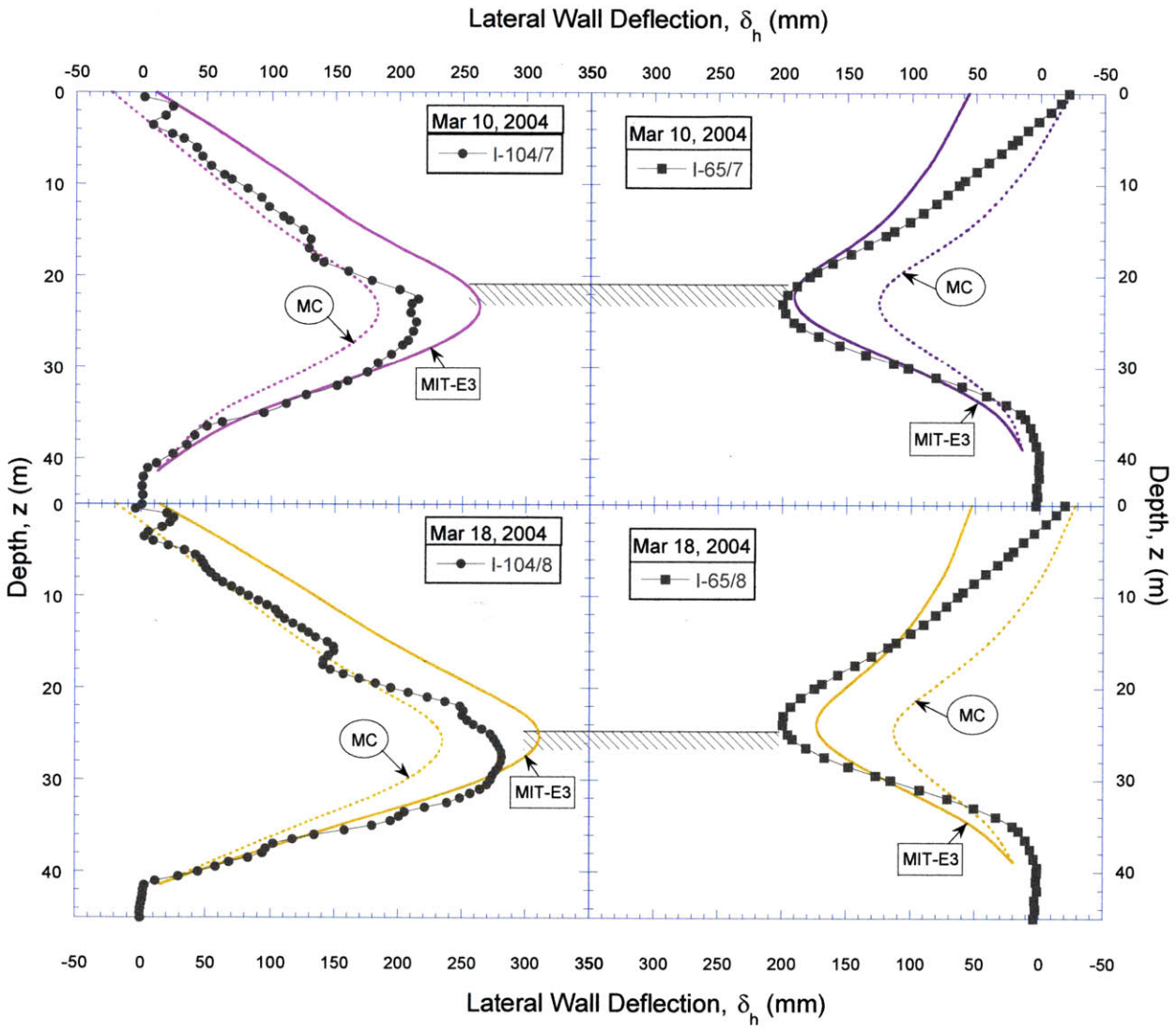

Figure 6-4: Measured and Predicted Wall Deflections for Excavation Levels 7 and 8

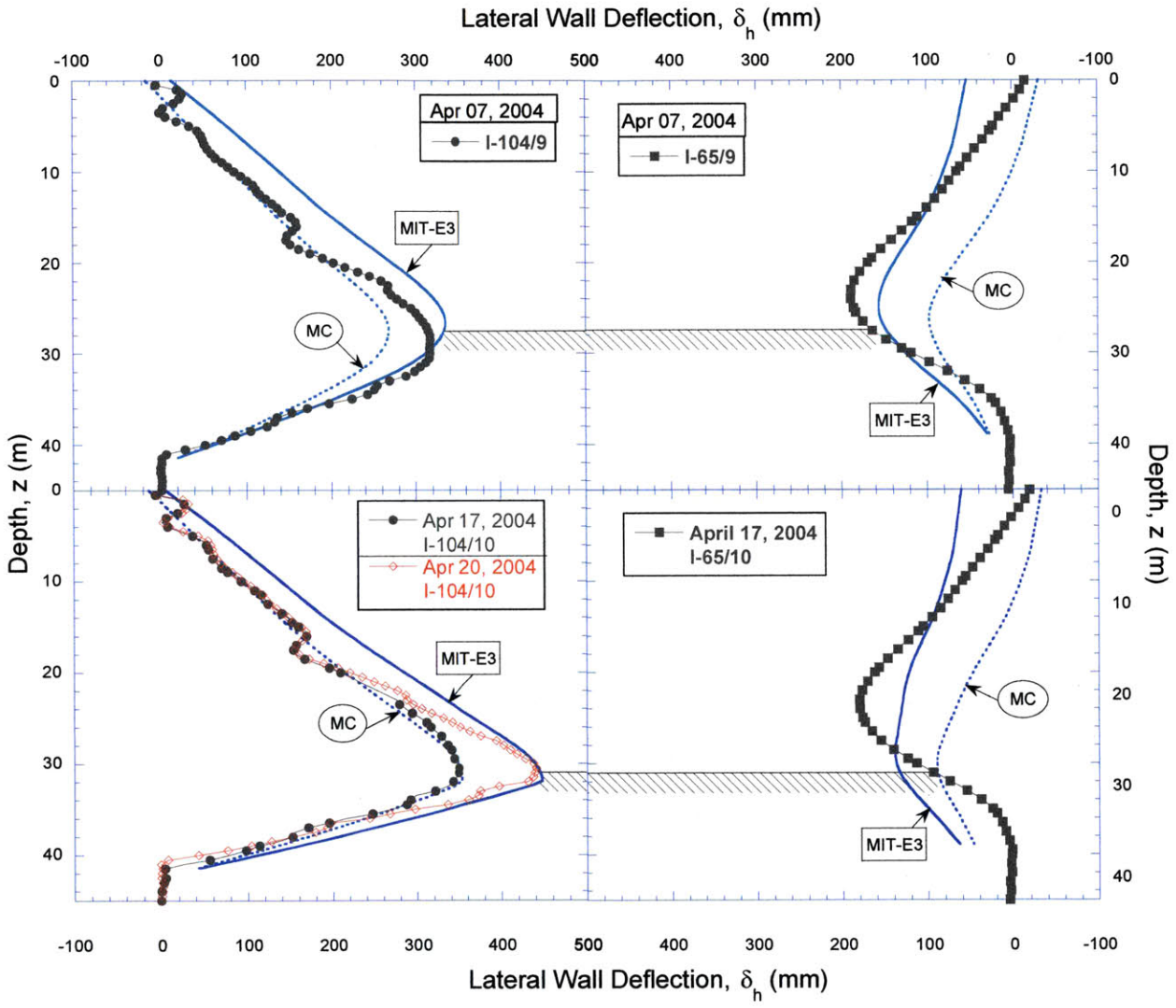

Figure 6-5: Measured and Predicted Wall Deflections for Excavation Levels 9 and 10

Table 6-2: Summary of Computed and Measured Maximum Lateral Wall

		Maximum Lateral Wall Deflections (mm)					
After Excavation		South			North		
Level	EL. RL (m)	MC	MIT-E3	I-104	MC	MIT-E3	I-65
5	87.6	105	172	96	83	153	93
6	84.6	120	192	158	105	173	159
7	81.6	183	263	215	126	191	200
8	78.3	235	311	282	113	173	200
9	75.3	268	335	317	98	157	190
10	72.3	354	447	350	90	139	190

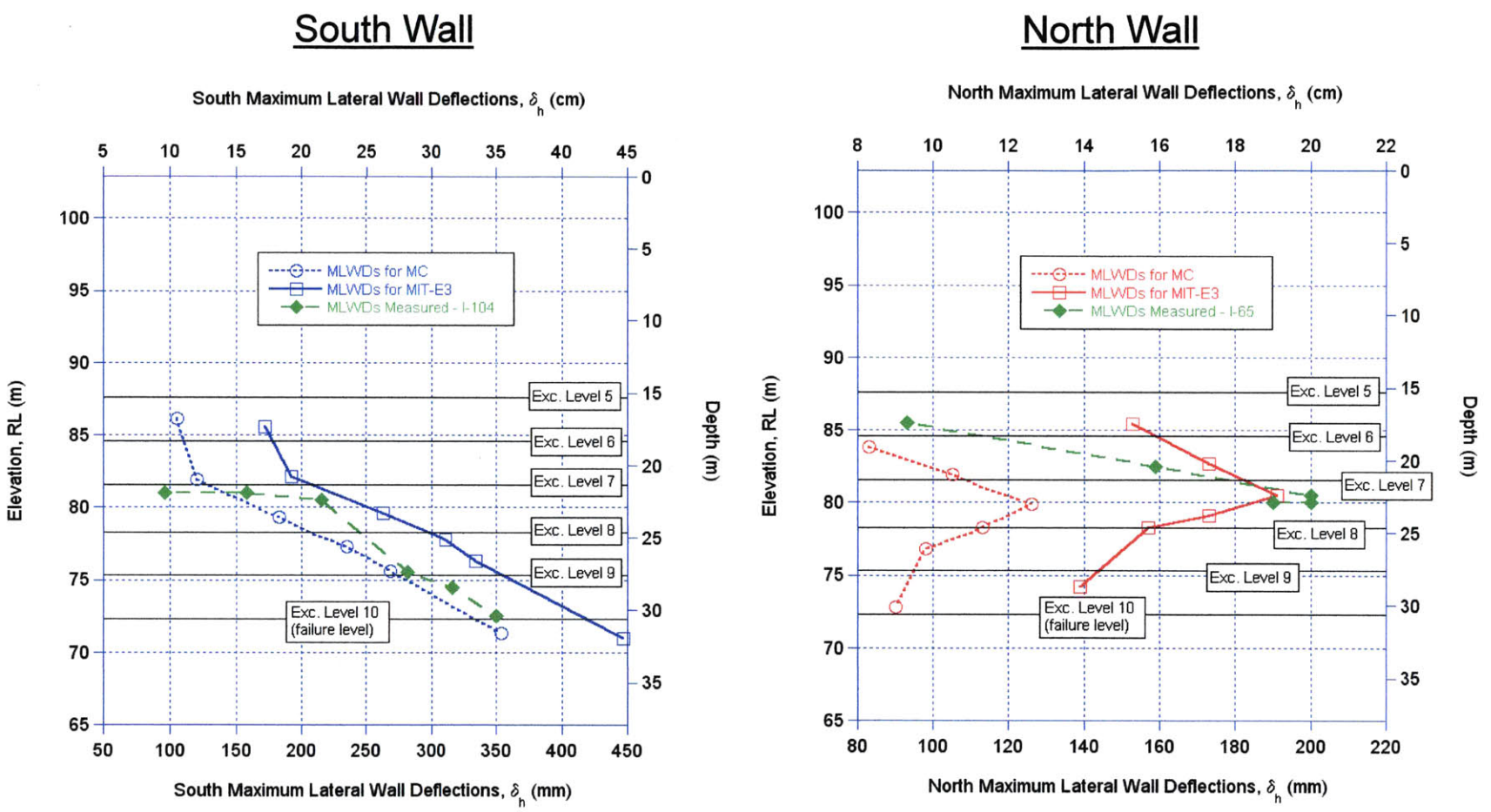

Figure 6-6: Computed and Measured Maximum Wall Deflections (a) South Wall (b) North Wall

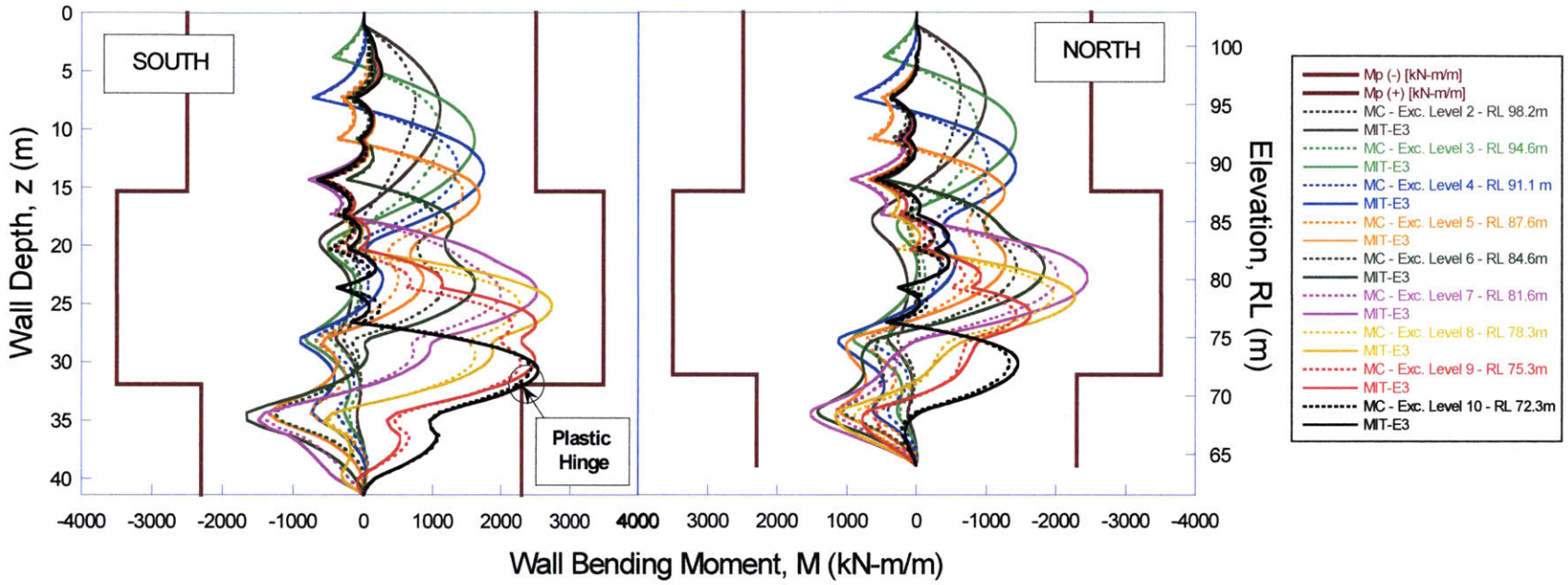

Figure 6-7: Bending Moments for (a) South Wall, and (b) North Wall

Table 6-3: Summary of Maximum Wall Bending Moments

		Maximum Wall Bending Moments (kN-m/m)			
After Excavation		South		North	
Level	EL. RL (m)	MC	MIT-E3	MC	MIT-E3
1	100.9	115	319	117	540
2	98.2	745	1108	624	984
3	94.6	1118	1612	870	1420
4	91.1	1367	1747	1024	1420
5	87.6	1443	1687	1030	1274
6	84.6	1267	1652	1436	1833
7	81.6	1996	2520	2026	2450
8	78.3	2273	2736	1971	2270
9	75.3	2286	2509	1431	1632
10	72.3	2432	2533	1328	1454

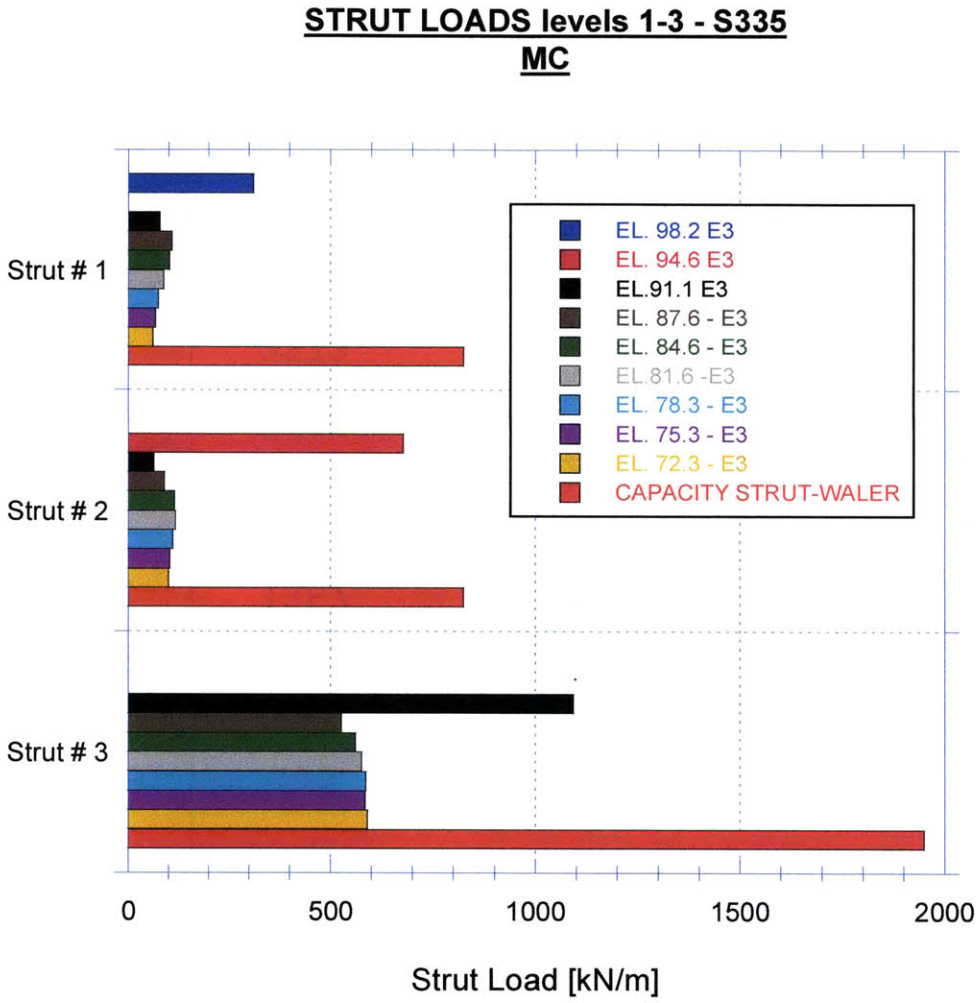

Figure 6-8: S335-Strut Loads for Strut Levels 1, 2 & 3, using MC

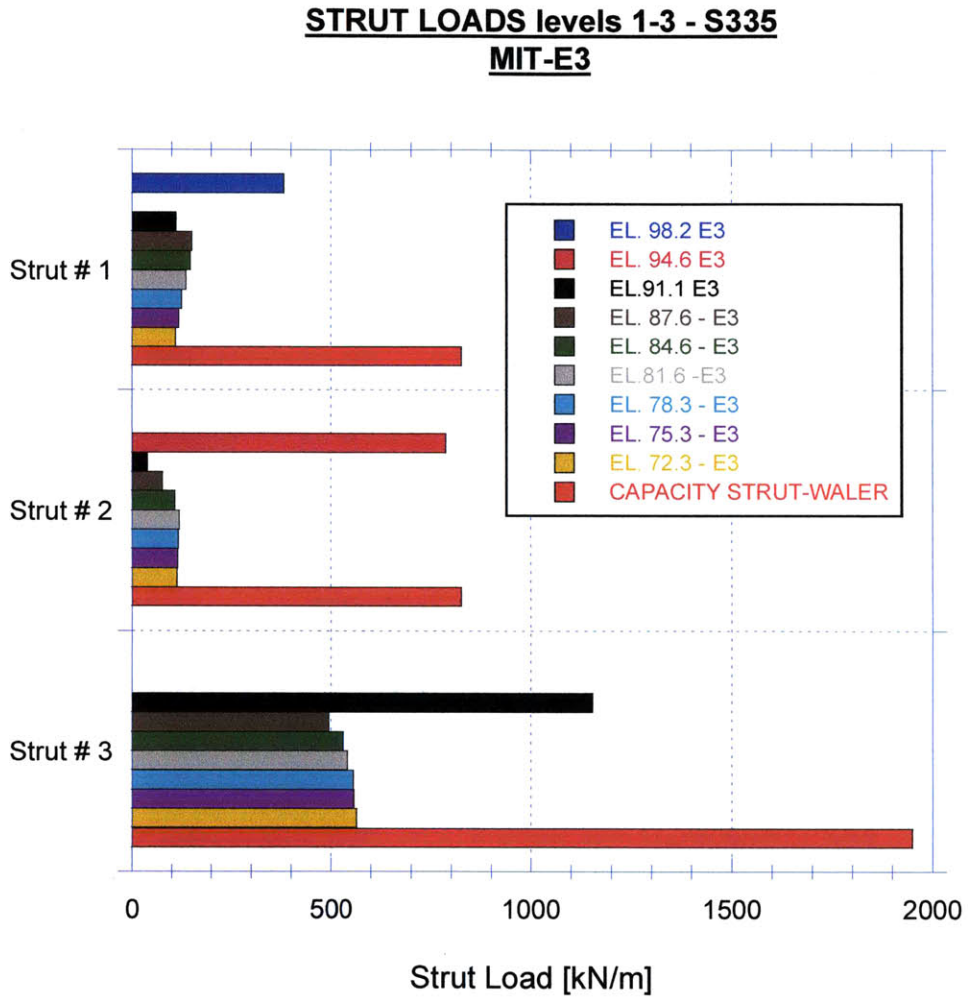

Figure 6-9: S335-Strut Loads for Strut Levels 1, 2 & 3, using MIT-E3

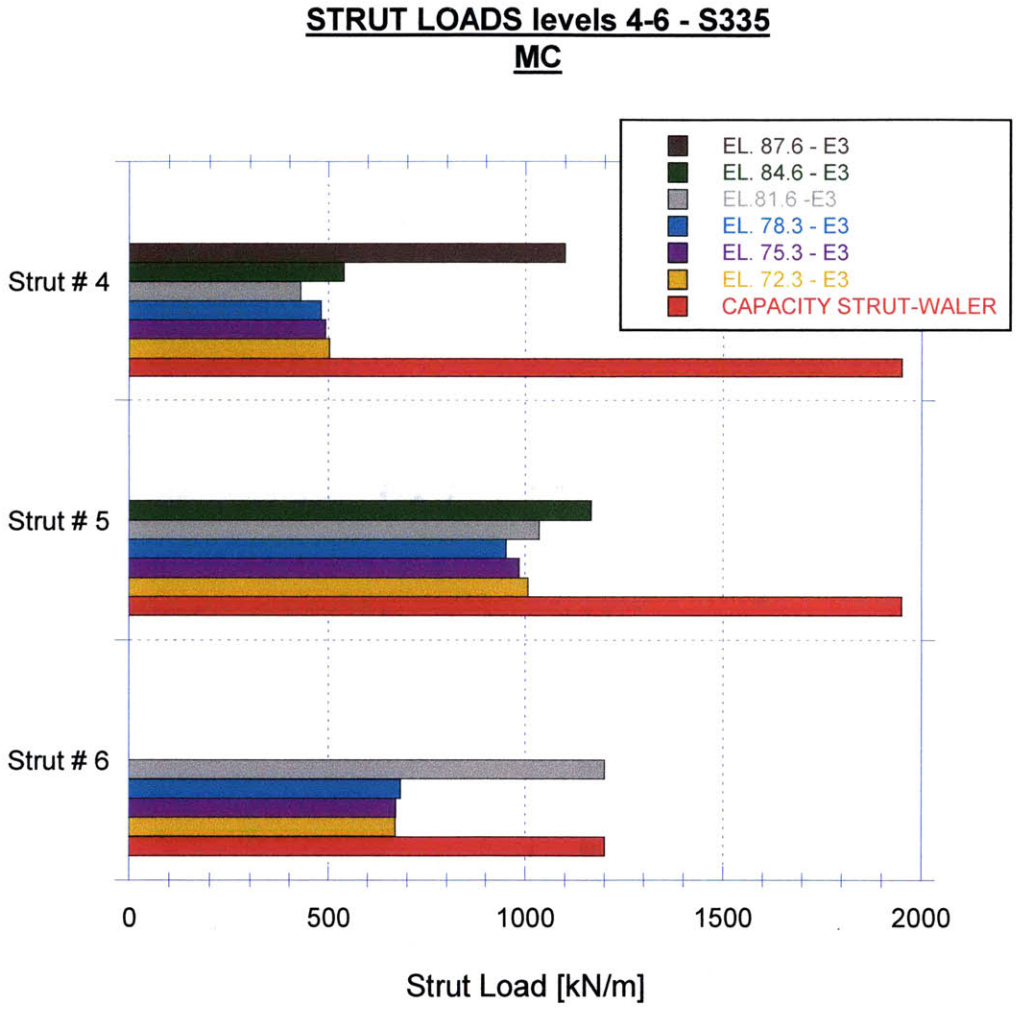

Figure 6-10: S335-Strut Loads for Strut Levels 4, 5 & 6, using MC

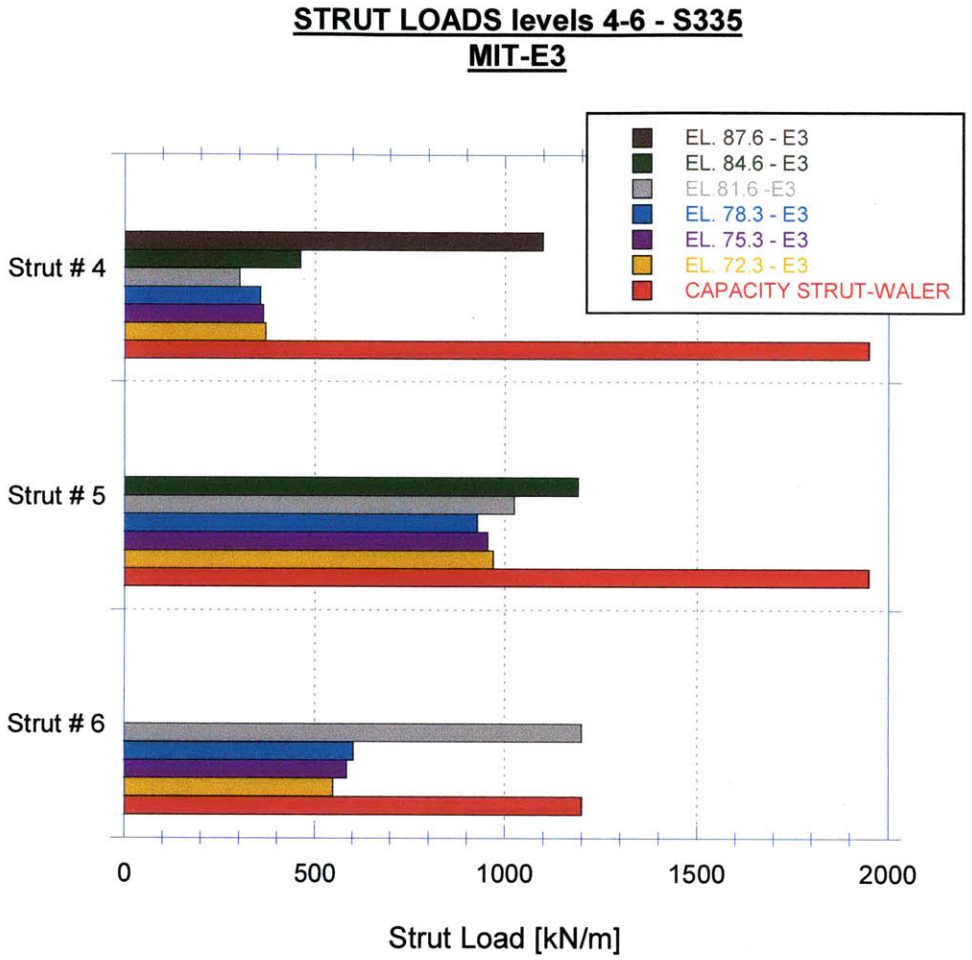

Figure 6-11: S335-Strut Loads for Strut Levels 4, 5 & 6, using MIT-E3

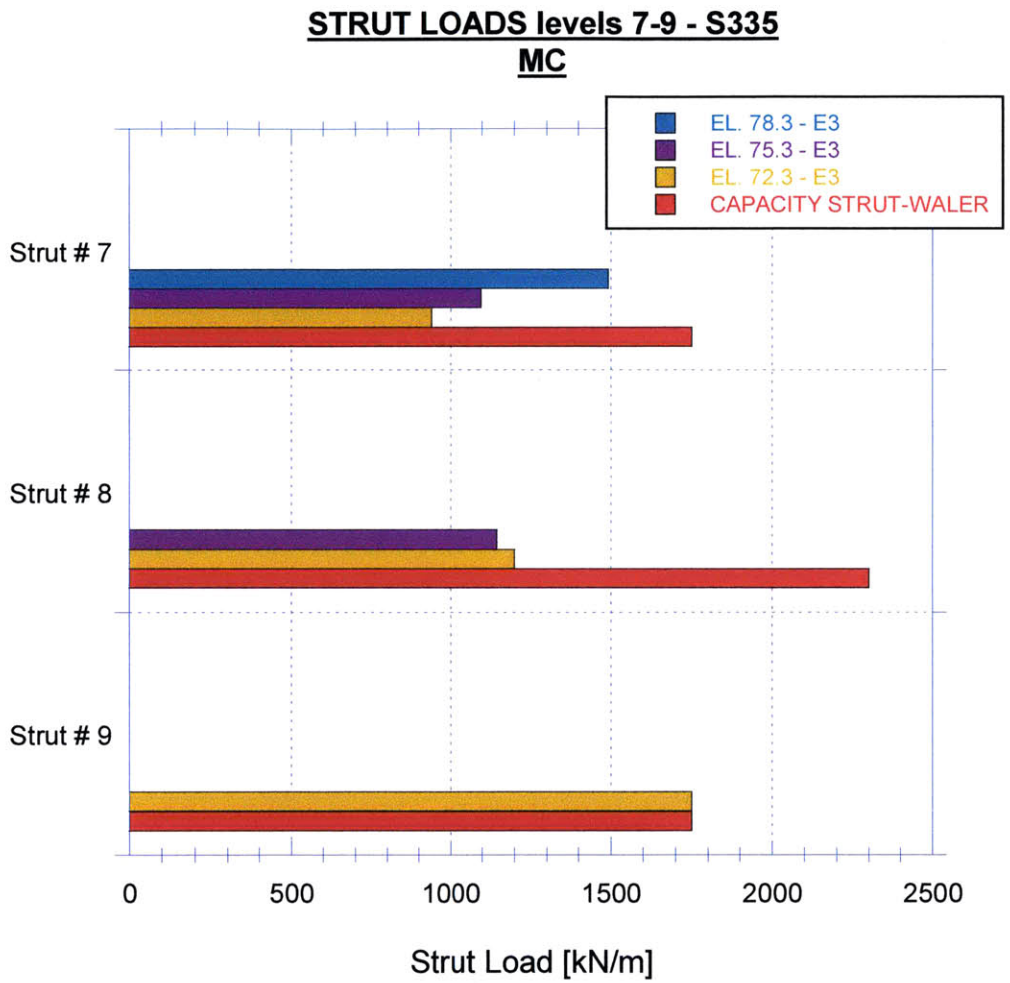

Figure 6-12: S335-Strut Loads for Strut Levels 7, 8 & 9, using MC

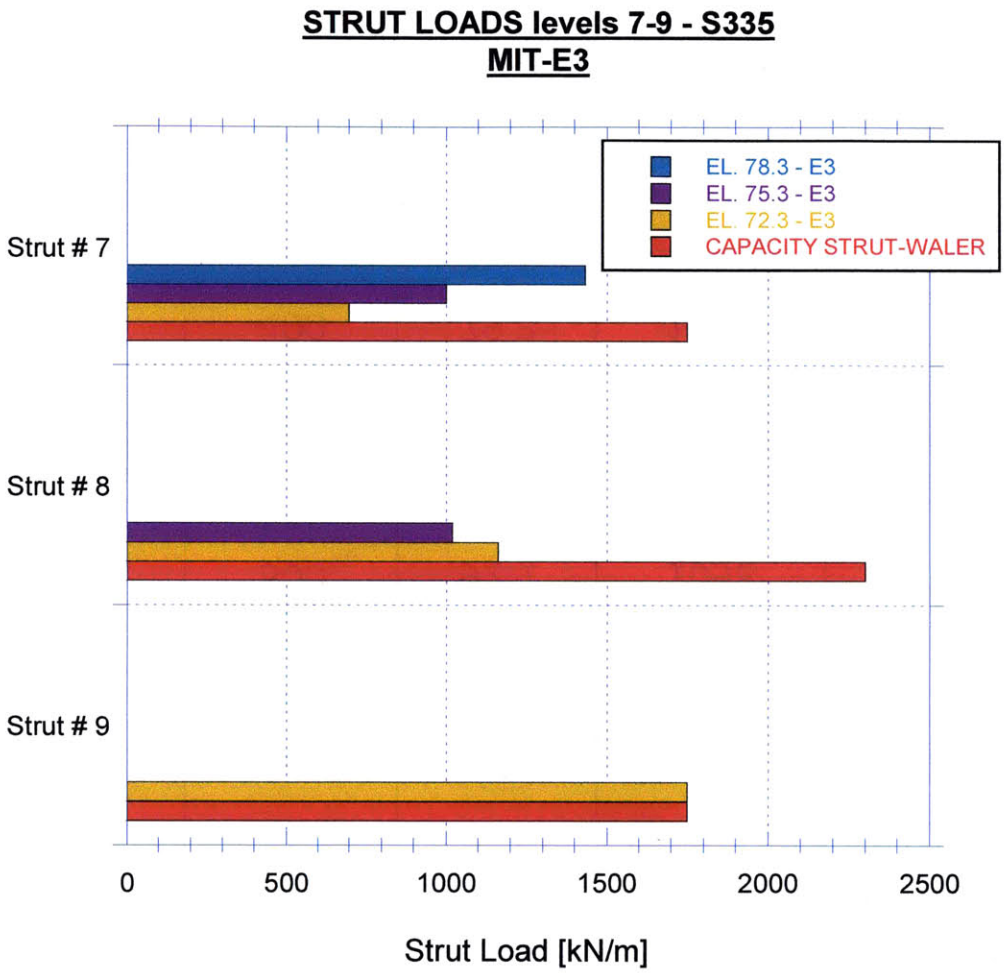

Figure 6-13: S335-Strut Loads for Strut Levels 7, 8 & 9, using MIT-E3

Table 6-4: S335 Predicted Maximum Strut Loads

Strut			Maximum Strut Loads (kN/m)		
#	Pre-Load	EL. RL (m)	MC	MIT-E3	Capacity
1	200	101.9	311	382	825
2	363	99.2	678	786	825
3	630	95.6	1093	1154	1950
4	500	92.1	1098	1099	1950
5	525	88.6	1165	1191	1950
6	**265**	**85.6**	**1200**	**1200**	**1200**
7	605	82.6	1492	1433	1750
8	400	79.3	1200	1162	2300
9	**250**	**76.3**	**1750**	**1750**	**1750**

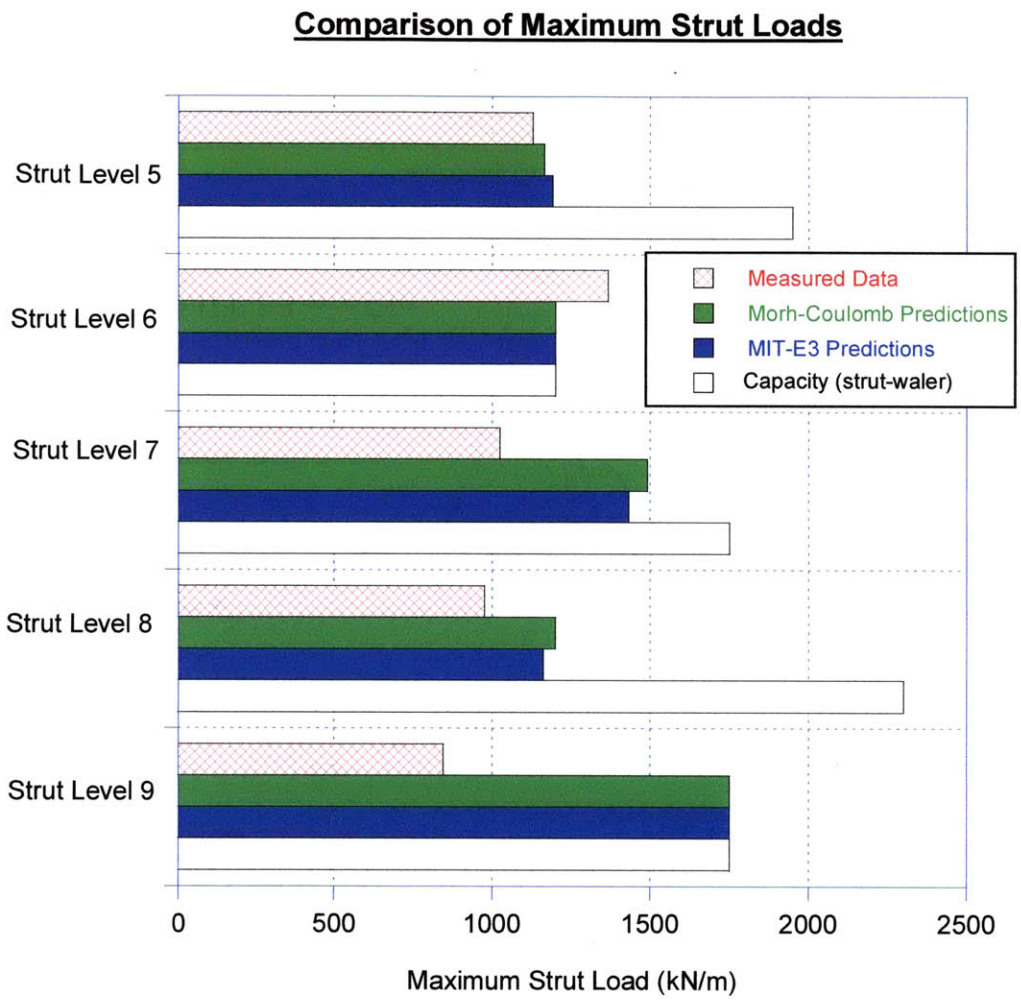

Figure 6-14: Comparison of Measured and Predicted Maximum Strut Loads

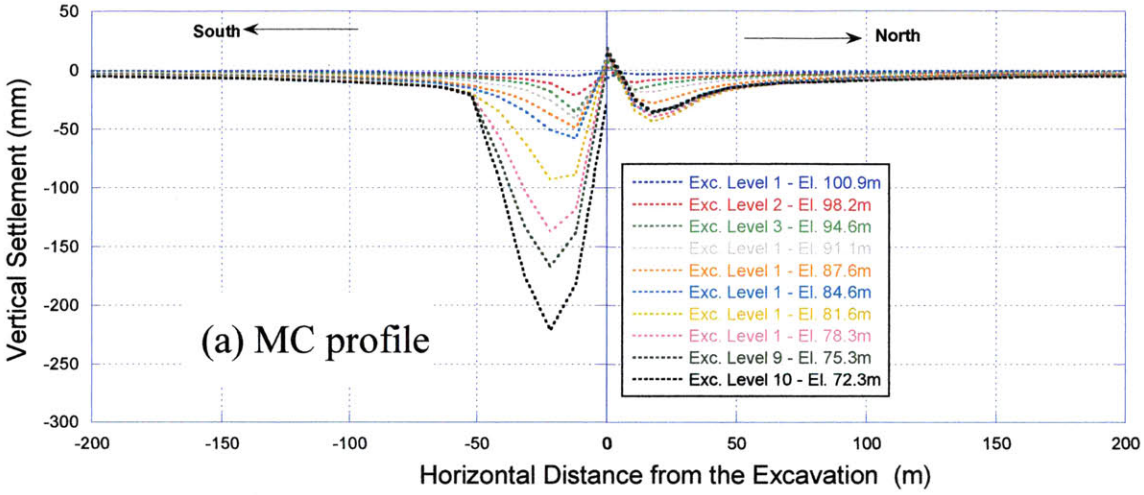

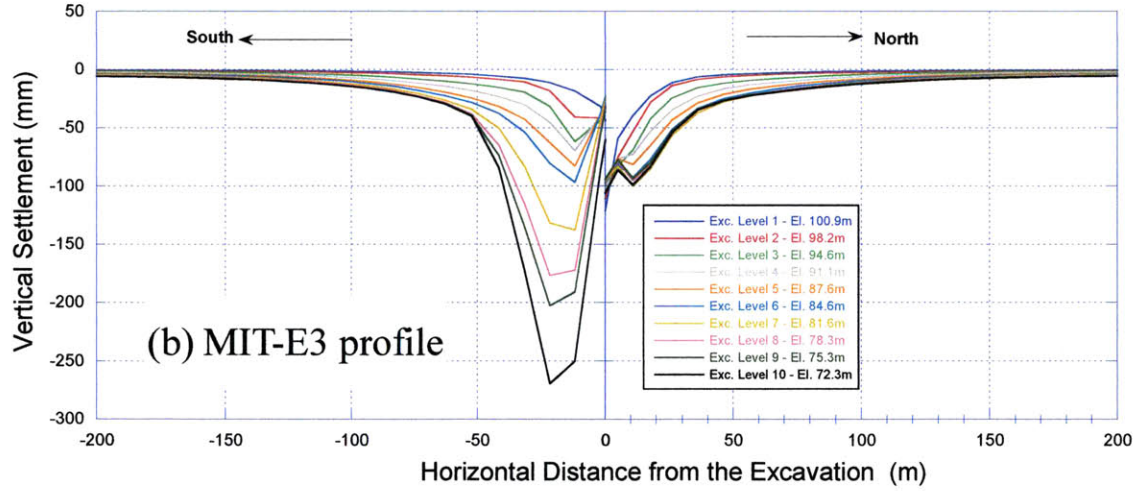

Figure 6-15: Predicted Surface Vertical Settlements

Table 6-5: Predicted Maximum Surface Vertical Settlements

		Maximum Vertical Settlements (mm)			
After Excavation		South		North	
Level	EL. RL (m)	MC	MIT-E3	MC	MIT-E3
1	100.9	6	44	6	122
2	98.2	21	42	11	111
3	94.6	36	62	16	106
4	91.1	41	70	18	102
5	87.6	49	83	28	98
6	84.6	58	97	37	97
7	81.6	93	138	44	100
8	78.3	137	177	40	96
9	75.3	167	203	36	94
10	72.3	221	269	35	106

7 CONCLUSIONS & RECOMMENDATIONS

7.1. Summary

A well-documented failure of a 30m deep braced excavation in underconsolidated marine clay using an advanced effective stress soil model (MIT-E3) is re-analyzed. The collapse of the Nicoll Highway during construction of cut-and cover tunnels for the new Circle Line in Singapore has been extensively investigated and documented. All prior analyses of the collapse have relied on simplified soil models with undrained strength parameters based on empirical correlations and piezocone penetration data. The present analyses use results from high quality consolidation and undrained triaxial shear tests that were only available after completion of the public inquiry. The current analyses achieve very reasonable estimates of measured wall deflections and strut loads using model parameters derived directly from the laboratory tests. The analyses confirm prior interpretations of the failure mechanism but provide a more rational basis for the modeling of soil-structure interaction.

7.2. Conclusions

The performance of the lateral earth support system for a critical instrumented section, S335, of the cut-and-cover excavations at the site where the Nicoll Highway collapsed in 2004, have been re-analyzed. Engineering properties of the key Upper and Lower marine clay units have been modeled using the generalized effective stress soil model, MIT-E3, with input parameters calibrated using laboratory test data obtained as part of the post-failure site investigation. The

model predictions are evaluated through comparisons with monitoring data and through comparisons with results of prior analyses using the Mohr-Coulomb (MC) model (Whittle & Davies, 2006). The MIT-E3 analyses provide a modest improvement in predictions of the measured wall deflections compared to prior MC calculations and give a consistent explanation of the bending failure in the south diaphragm wall and the overloading of the strut-waler connection at the 9th level of strutting. The current analyses do not resolve uncertainties associated with performance of the JGP rafts, movements at the toe of the north-side diaphragm wall or discrepancies with the measured strut loads at level 9. However, they represent a significant advance in predicting excavation performance based directly on results of laboratory tests compared to prior analyses that used generic (i.e., non site-specific) design isotropic strength profiles.

7.3. Recommendations

Advanced soil model calibrations of other main units are indeed recommended. Therefore, high quality of laboratory soil tests is always required.

Accurate measurements of pore pressures must be carefully considered when a project of this magnitude is planned. This has a huge impact on predictions by numerical analyses. In addition, precise measurements of vertical settlements surrounding the excavation play a very important role.

An adequate use of monitoring data can certainly be much more useful if inverse analyses for model parameter identifications are available.

LIST OF REFERENCES

Arup (2005). Report for the Ministry of Manpower Committee of Inquiry - Circle Line, Singapore Contract 824 - Supplemental Expert Report (Volume 1 & 2), Ove Arup & Partners, Unpublished.

Bell, B.C., and Chiew, S-P. (2006). "Nicoll Highway Collapse: Some Structural Observations: Part 2: Soil Retention System", *Proc. International Conference on Deep Excavations,* Singapore 2006, 1-15.

Bird, M. I., Chang, C. H., Shirlaw, J.N., Tan, T.S., Teh, T.S. (2003). "The Age and Origin of the Quaternary Sediments of Singapore with Emphasis on the Marine Clay." *Proc. Underground Singapore* 2003, 428-439.

Cao, L. F., Chang, M. F., Teh, C.I., Choa, V., Bo, M. W. (2001). "Evaluation of Shear Strength Parameters of Singapore Marine Clay." *Proc. Underground Singapore* 2001, 315-322.

Chiam, S. L., Wong, K. S., Tan, T.S., Ni, Q., Khoo, K.S., Chu, J. (2003). "The Old Alluvium." *Proc. Underground Singapore* 2003, 408-427.

Chu, J., Bo, M.W.,Chang, M.F., and Choa, V. (2002). "Consolidation and Permeability Properties of Singapore Marine Clay", ASCE *J. Geotech. Geoenviron. Eng.,* 128 (9), 724-732.

COI (2005). Report of the Committee of Inquiry into the Incident at the MRT Circle Line Worksite that Led to the Collapse of Nicoll Highway 20 April 2004. Report Submitted to the Minister of Manpower, Government of Singapore.

Corral, G. and Whittle A.J. (2010). "Re-analysis of Deep Excavation Collapse Using Generalized Effective Stress Soil Model." *ASCE Earth Retention Conference (ER2010),* Bellevue WA, August 2010.

Davies, R.V., Fok, P., Norrish, A., and Poh, S.T. (2006). " The Nicoll Highway Collapse: Field Measurements and Observations", *Proc. International Conference on Deep Excavations,* Singapore 2006, 1-15.

Ferrari, A. A. (2007). A remedial approach to stabilize a deep excavation in Singapore, M.Eng Thesis. Dept. of Civil and Environmental Engineering, MIT, Cambridge, MA., 103 pages.

Geotechnical Consulting Group (2005). "Investigation into Nicoll Highway Collapse - Supplementary Report - submitted to Nishimatsu, Construction Company Limited.", Unpublished.

GIM (2001) Geotechnical Interpretative Memorandum C824/DES/DM/002A, Project Document, Unpublished.

Hashash, Y. M. A. (1992). "Analysis of deep excavations in clay." PhD Thesis. Dept. of Civil and Environmental Engrg., MIT, Cambridge, MA, 337p.

Hashash, Y. M. A. and Whittle, A. J. (1992). "Analysis of braced diaphragm walls in deep deposits of clay." *Res. Rep. R92-19*, Dept. of Civ. Engrg., MIT, Cambridge, Mass.

Jen, L. C. (1997). "The design and performance of deep excavations in clay." PhD Thesis. Dept. of Civil and Environmental Engrg., MIT, Cambridge, MA, 698p.

Kiso-Jiban, C. C. L. (2004). 3rd Progress Factual Report on Soil Investigation at Nicoll Highway, Report submitted to Nishimatsu Construction Co Ltd., Unpublished.

Lee, F. H. (2008). "How Useful is Numerical Analysis in Geotechnical Engineering?" International Conference on Deep Excavations, *Proc. Int. Conf. on Deep Exc.* 2008, 1-19.

Lee, F. H., Qian, G., Pengjun, Z., Han, H.S., Ming, J.Y.Y., Sivasangari, M. (2005). "Three-Dimensional Analysis of the Nicoll Highway Collapse." Unpublished, Report to LTA.

Lewin, J. and Chau T. L. (2006). "Construction Works on Contract 828 following the Nicoll Highway Collapse in Singapore." *International Conference and Exhibition on Tunnelling and Trenchless Technology* 7-9 March 2006, Selangor, 1-11.

Mote, T. I., Bowden, A. J., McGowan, M. (2009). "Palaeochannel Mapping beneath Singapore." *Proc. Underground Singapore 2009*, 109-117.

Pitts, J. (1984). "A Review of Geology and Engineering Geology in Singapore." *Quarterly Journal of Engineering Geology and Hydrogeology*, 17, 93-101.

Plaxis (2009). Plaxis 2D v.8.5. http://www.plaxis.nl/.

Sharma, J. S., Chu, J., Zhao, J. (1999). "Geological and Geotechnical Features of Singapore: an Overview." *Tunnelling and Underground Space Technology*, 14(4), 419-431.

Tanaka, H., Locat, J., Shibuya, S., Soon, T.T., Shiwakoti, D.R. (2001). "Characterization of Singapore, Bangkok, and Ariake clays." *Canadian Geotechnical Journal*, 38(2), 378-400.

Whittle, A. J. (1993). "Evaluation of a Constitutive Model for Overconsolidated Clays." *Geotechnique* 43(2), 189-313.

Whittle, A. J. (2004). Report Submitted to COI, Unpublished.

Whittle, A. J. and R. V. Davies (2006). "Nicoll Highway Collapse: Evaluation of Geotechnical Factors Affecting Design of Excavation Support System." *International Conference on Deep Excavations*, Singapore, 2006, 1-16.

Whittle, A. J., Degroot, D. J., Ladd, C. C., and Seah, T. H.. (1994). "Model Prediction of the Anisotropic Behavior of Boston Blue Clay." ASCE Journal of Geotech. Engrg., 120(1), 199-224.

Whittle, A. J. and Hashash, Y. M. (1994). "Soil Modeling and Prediction of deep excavation behavior." *International Symposium on Pre-Failure Deformation Characteristics of Geo-Materials. IS-Hokkaido'94*, Japan, A. A. Balkema, Vol. 1, 589-595.

Whittle, A. J. and Hashash, Y. M. (1996). "Ground Movement Prediction for Deep Excavations in Soft Clay." ASCE Journal of Geotechnical Engineering, 122(6), 474-486.

Whittle, A. J. and Kavvadas, M. J. (1994). "Formulation of MIT-E3 Constitutive Model for Overconsolidated Clays." ASCE Journal of Geotechnical Engineering, 120(1), 173-198.

Whittle, A. J. (1987) "A constitutive model for overconsolidated clays with application to the cyclic loading of friction piles." PhD Thesis. Dept. of Civil and Environmental Engrg., MIT, Cambridge, MA, 641p.

Whittle, A. J. and Sutabutr, T. (2005). "Parameters for Average Gulf Clay and Prediction of Pile Set-up in the Gulf of Mexico." Constitutive Models. Part of Evaluation, Selection, and Calibration, ASCE, GSP No. 128, 440-458.